Imperial College London

Light diffraction in all-optical time-varying metasurfaces

Romain Tirole

Department of Physics
Imperial College London

Submitted in partial fulfilment of the requirements for the degree of

Doctor of Philosophy in Physics and the Diploma of Imperial College London, June 2023.

Abstract

This thesis focuses on frequency control of optical waves using time-varying effects in nanophotonic media. Particularly, diffraction by a slit in time is demonstrated using ultrafast all-optical mirrors. We first demonstrate a large reflectivity change from an Indium Tin Oxide/Gold bilayer under optical pumping, at speeds high enough to observe time-varying effects. Then, treating the mirror as an interface, we show time-diffraction from the sample, corresponding to broadening and shifting of the spectrum of light reflected by the mirror during its modulation. This is clearly confirmed by a double slit diffraction experiment, replicating Young's experiment in time, with a generated spectrum exhibiting oscillations in frequency. Insights on the electron dynamics within Indium Tin Oxide is gained, with in particular a striking shortening of the permittivity modulation rise time unlocking the access to an even lower timescale for time-varying effects. Finally, time-varying effects on harmonic generation from Indium Tin Oxide and Gallium Phosphide thin films are demonstrated, exhibiting strong temporal refraction and new mechanisms for temporal modulation.

Statement of originality

I am the author of this thesis, which is written in my own words. All else is appropriately referenced.

Thursday 8th June, 2023

Romain Tirole

Copyright statement

List of publications

1. E. Galiffi, R. Tirole, S. Yin, H. Li, S. Vezzoli, P. A. Huidobro, M. G. Silveirinha, R. Sapienza, A. Alù, and J. B. Pendry, "Photonics of time-varying media", Advanced Photonics **4**, 014002 (2022).

2. R. Tirole, E. Galiffi, J. Dranczewski, T. Attavar, B. Tilmann, Y.-T. Wang, P. A. Huidobro, A. Alù, J. B. Pendry, S. A. Maier, S. Vezzoli, and R. Sapienza, "Saturable Time-Varying Mirror Based on an Epsilon-Near-Zero Material", Physical Review Applied **18**, 054067 (2022).

3. R. Tirole, S. Vezzoli, E. Galiffi, I. Robertson, D. Maurice, B. Tilmann, S. A. Maier, J. B. Pendry, and R. Sapienza, "Double-slit time diffraction at optical frequencies", Nature Physics, 1–4 (2023).

4. R. Tirole, B. Tilmann, L. de S. Menezes, S. Vezzoli, S. A. Maier, R. Sapienza, "Dielectric epsilon near-zero hybrid nanogap antennas for nonlinear nanophotonics" (in preparation)

5. R. Tirole, S. Vezzoli, S. Yang. E. Galiffi, S. A. Maier, J. B. Pendry, R. Sapienza "All optical modulation of second harmonic generation in an Indium Tin Oxide thin film" (in preparation)

Acknowledgements

This thesis is the sum of contributions from a galaxy of friends and colleagues. For this I am indebted to many people for their support, guidance and friendship over the long course of my thesis, and would like to thank the not-so-few who have made this work possible.

First, I thank my supervisor, Prof. Riccardo Sapienza, for taking me under his wing and welcoming me in his research group. His patience, guidance, vision and vast experience of academic and non-academic matters truly is an aspiration. I also thank my second supervisor, Prof. Stefan Maier, for his precious advice and guidance, and for giving me the opportunity to visit and work in his research group in LMU Munich.

Second, I would like to thank Dr. Stefano Vezzoli, who has set the bar extremely high for that it means to be a Physicist. He has taught me everything I know in and out of the lab, with a continuous kindness, patience and a selflessness that only do credit to his modesty.

I would also like to thank Dr. Emanuele Galiffi, who introduced me both to time-varying media and the Imperial College Optical Society. His help and experience have been immensely precious, and I look forward to many more fascinating scientific discussions with him.

I also thank Prof. Sir John Pendry, Dr. Paloma Arroyo Huidobro and Prof. Andrea Alù for their precious advice and essential role in the development of my research projects and publications, it has been a real privilege to work and exchange with them.

A special thanks goes to all those in the group that made my time at Imperial special. Though the list is long, I would like to thank Dr. Tahiyat Huq for being my sister in arms during the length of this PhD, Dr. Harriet Walker, Dr. Mónica Mota, Dr. Paul Dichtl and Dr. Nicolas Güsken for their guidance and friendship as senior PhD students. I would like to thank Benjamin Tilmann for welcoming me in Munich with his friendship and kindness, and for his excellent collaborative work. I am also grateful to Dr. Leonardo de Souza Menezes and the whole group at the Nanoinstitut München for being so welcoming. I am indebted to Dr. Emma Pearce, Dr. Alex Chan and Julia Brug whose excellent banter saved me from drowning in my own work in the office. I thank everyone else in the office, the Optical Society and the group, and the talented MSc students I had the privilege to work with. I also thank everyone in the wider Experimental Solid State group, in research, administration, the nanofab lab and workshop.

I also would like to thank everyone who helped me grow as a physicist before my PhD, and to those I owe my passion for Nanophotonics and Metamaterials: Dr. Charles Roques-Carmes, Dr. Yi Yang and Prof. Marin Soljačić, Dr. Sylvain Gennaro and Prof. Rupert Oulton, Dr.

Omid Siddiqui, Dr. Tijmen Euser, and Prof. Jeremy Baumberg.

I am incredibly indebted to my friends outside of work, who made me love life in London. I would like to thank Dr. Jakub Szypicyn for his extreme patience and precious friendship, being locked in a flat with me for two years must have been a demanding demonstration of the relativity of time. I thank Dr. Dan Terracina Barcas for his friendship and leaving said flat, and in doing so preserving what was left of Jakub's sanity. I thank Dr. Javier Cañada Pérez-Sala for the sneaky slippers and the demonstration of tyre burning at too many revs per minute, as well as being an excellent flatmate. I thank Dr. Eleni Pahita and future Dr. Karen Wendt for being the best of friends. I thank Robert Olrog, whose friendship is very precious to me, for all the memories that we've made over the years and all those yet to come. I thank my friends from home Gauthier Le Bouëdec, Anna Aldanondo and Pierre-Louis Gautier, for their continuous friendship and support, and making home feel like home though it has been seven years since I left Toulouse.

I would like to thank in groups my old friends from Pembridge, the Imperial Eagles Handball Club, the University of Cambridge, my friends from Toulouse who also ended up in London and those who didn't, and all those I may have forgotten. What I lack in words here I will make up with in pints.

I would like to thank my girlfriend, Gabrielle, and give her my most sincere expression of love and gratitude. Her presence, love and kindness have shielded me from anxiety and continue to inspire me to be a better version of myself everyday.

Finally, I would like to thank my family, my parents Nathalie and Jean, my sisters Naïs and Margot as well as newcomers William and baby Marguerite. Occasions and words will always be too few to describe my love and gratitude to them, and how much they mean to me.

'Là était la certitude, dans le travail de tous les jours. Le reste tenait à des fils et à des mouvements insignifiants, on ne pouvait s'y arrêter. L'essentiel était de bien faire son métier.'

Albert Camus, La Peste

'There lay certainty, in the daily task. The rest hung on thin threads and meaningless gestures, which one couldn't stop to consider. The essential thing was to do one's job well.'

Albert Camus, The Plague

Table of contents

List of Figures

List of Acronyms

NIR near-infrared

TCO transparent conducting oxides

ENZ epsilon-near-zero

ITO Indium Tin Oxide

AZO Aluminium-doped Zinc Oxide

PMMA Poly(methyl methacrylate)

BBO Beta Barium Borate

SHG second harmonic generation

THG third harmonic generation

FWM four wave mixing

SFG sum frequency generation

DFG difference frequency generation

SPDC spontaneous parametric down conversion

TPA two-photon absorption

FWHM full width at half maximum

TMM transfer matrix method

Chapter 1

Introduction

1.1 Time-varying media

Physicists and electrical engineers have long sought to structure media in time to create dynamic, active and reconfigurable systems. This means changing the properties of a medium as a function of time, and thus affecting waves interacting with said medium during that change. By nature, as an input of energy is required to modulate a medium, time-varying media break reciprocity (energy is no longer conserved) and allow to overcome the physical limits of static systems, such as the absence of reconfigurability. An example application can be found in isolators, which transmit waves in only one direction and are an essential component of full-duplex systems (systems that can simultaneously transmit and receive information at a given frequency) [1, 2]. Time-varying systems aim at controlling wave properties and as a consequence can be designed in various fields of physics such as mechanics [3], acoustics [4, 5], acousto-optics [6], optomechanics [7, 8], electronics [9], optoelectronics [10, 11] or spintronics [12]. This thesis focuses on the design of nanoscale photonic time-varying media, that is nanometer-scaled systems allowing for time-varying effects observable at visible and near-infrared (NIR) frequencies ($\sim$ 160 to 750 THz).

Thanks to the rise of new fabrication techniques and new materials since the crossing of the millennium, the field of Nanophotonics, Plasmonics and Metamaterials is seeing a surge in interest and potential applications. By unlocking the strong interaction of nanostructures with light at visible and NIR frequencies, spatial architecture provides new degrees of freedom in the control of light. A next major step in Photonics now consists in transitioning from passive to active systems, spatial to spatiotemporal engineering, to allow for a higher level of light control and new applications [13]. One could then imagine the ultimate nanophotonic multiplexer, with direct control of both spatial and spectral distribution of light as illustrated in Fig. 1.1. For a broader review on photonic time-varying media, the author recommends the review by Galiffi et al. [14]. To stay within the scope of this work, we will focus our attention on frequency control in time-varying media, that is changes in the spectral density of light resulting from the interaction with a medium whose properties are evolving in time.

The apparition of frequency control of light in time-varying media is difficult to date: though

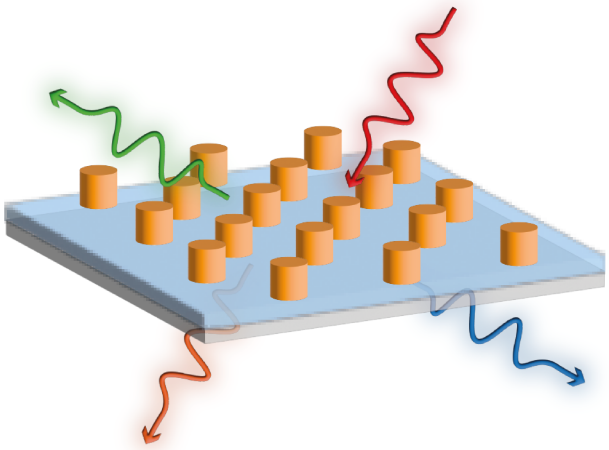

Figure 1.1: Illustration of a space-time metasurface. Light impinging on the surface (in red) could be scattered forward or backwards with different frequencies (orange, blue and green) leaving the metasurface at their respective desired direction of propagation, using time-varying physics. The metasurface could be reconfigurable, with a dynamic evolution the frequency modulation or beam steering.

the classical and quantum equations describing the behaviour of light have always been able to predict these effects, little record of such concepts is to be found in the first half of the XX$^{\text{th}}$ century.

J.T. Mendonça presents in his book *Theory of photon acceleration* [15] in 2000 an early development in the field of plasma physics. Frequency shifts were predicted for an electromagnetic wave interacting with a moving ionisation front, where the latter can be treated as a medium evolving sharply in time [16, 17]. This predicted broadening and shift in frequency was experimentally demonstrated in 1974 when a laser beam pulse was focused in an optical cavity, thus generating a flash ionisation [18]. This is an important point that may explain the lack of previous research on the topic: for any effect to be measurable in the spectrum, the medium modulation speed and amplitude must be comparable to the carrier frequency of the light wave, as will be shown in further detail in section 2.1.2. Subsequent experiments with microwaves reflected by relativistic electron beams [19] and simulations of photons in plasma wakefield perturbations, used to accelerate charged particles, also demonstrated the presence of a frequency shift [20]. The latter work coined the term *photon acceleration* for the first time, referring to the existence of an effective mass of photons in a medium (i.e. outside of vacuum) and in an analogy to Newtonian mechanics: a change in the medium is translated into a change in mass, which will 'accelerate' the photon.

In parallel, the field of Nonlinear Optics was flourishing thanks to the development of the laser allowing to reach higher field intensities. After Franken et al.'s first demonstration of second harmonic generation (SHG) [21], experiments on self-modulation [22–24], cross-modulation [25–27] and other nonlinear mechanisms followed in demonstrating the concept of photon acceleration and analogous modulations of the spectrum of light under a different label. The commonly used electromagnetic nonlinear optical formalism [28] can be reinterpreted as a medium evolving in time and acting on the frequency and amplitude of electric fields within it, as will be seen in section 2.3.

In yet another parallel stream of research, the transient behaviour of atoms, molecules and neutrons in the presence of a slit opening and closing in time (again, a time-varying medium) was investigated in the 90s, with predicted and measured oscillations in the particle's time of flight signal [29–33]. These were all in the continuation of a first prediction made by M. Moshinski in 1952 [34], that will be explored and discussed in chapter 5.

In the end, it was J.T. Mendonça's work that played an important role in recognizing the similarities across all these fields of research and unifying them in a single framework, that of time-varying media, as well as coining terms such as time refraction or time reflection in 2000. It is not before the late 2010s that time-varying physics flourished again when a new push in theory along with new fabrication techniques and materials unlocked new opportunities for experiments (see section 2.2 and for further reading section 5 of *Photonics of time-varying media* [14]).

1.2 Thesis plan

This thesis will focus on the experimental investigation of diffraction of light from a slit in time. It is divided in chapters as follows. First, fundamental concepts and properties of time-varying media will be introduced in chapter 2, along with the nonlinear optical properties Indium Tin Oxide (ITO) and epsilon-near-zero (ENZ) media and the modelling methods used throughout the thesis. Then, chapter 3 describes the design and implementation of a single slit in time using a time-varying mirror made of an ITO/Au bilayer. The experimental methods are presented, as well as a comprehensive study of the reflectivity changes within the bilayer under optical pumping. Chapter 4 then studies the time-varying effects resulting in this single temporal slit, namely broadening and shifting of frequencies within the reflected probe spectrum. These effects are described as diffraction in time, and the use of a semi-analytical adiabatic model as well as a Fourier transform model confirms the presence of diffraction and unveil new

dynamics within the medium. Chapter 5 shows the first experimental demonstration of double slit diffraction in time at optical frequencies from the bilayer, and constitutes a solid demonstration of the power and usefulness of the time-varying diffraction formalism. The surprisingly short dynamics of the reflectivity rise from the ITO layer, in the range of 1-10 fs for a 225 fs long pump pulse, is further confirmed and hints at the presence of yet to be uncovered electron dynamics. Finally, modulation of harmonic light generation is explored in chapter 6. In ITO, surface second harmonic generation exhibits strong spectral modulation, with large frequency shifts and broadening from a single slit and a highly visible double slit diffraction spectrum. The modulation of SHG in ITO being comparable to that of its fundamental probe, we also investigate an alternative material, Gallium Phosphide, and achieve a large spectral modulation of third harmonic generation (THG), whereas modulation in the NIR is perturbative, showing a path to engineer harmonic light generation while preserving resonances at the fundamental. The results are summarised and an outlook is then presented in chapter 7.

Chapter 2

Epsilon-near-zero and time-varying media

2.1 Photonics of time-varying media: concepts and formalism

2.1.1 From space to time: the example of refraction

Many time-varying effects have a strong similarity with their spatial counterpart, and can be understood as time-domain equivalents of well known spatial optics. A light cone depicting the frequencies of non-evanescent light ω for given momenta in the (x, y) plane (k_x, k_y) is shown in Fig. 2.1(a,b), any photon propagating in free space being within or on the surface of this cone. Light propagating in space will go through changes in permittivity at the interface between different media, which corresponds on the dispersion diagram to a transition to another state on the horizontal plane intersecting the cone at the light's frequency in Fig. 2.1(a), within the cone (e.g. scattering by a sphere) or outside (e.g. evanescent waves from total internal reflection). For example, from classic electromagnetic theory, we expect a reflected (k to $-k$) and a transmitted (k to $n_2 k/n_1$) wave at an interface between two media with refractive indices n_1 and n_2.

The exact same system of transitions holds true for temporal modulation of permittivity, except for the fact that they now occur along a vertical line on the light cone as in Fig. 2.1(b) as it is now momentum that is being conserved. In spatial modulation, from Noether's theorem we know that the system being invariant in time implies energy conservation. For temporal modulation, as the system is no longer translation-invariant in time, energy and thus the frequency of the photon is not conserved. This is the essential mechanism behind photon acceleration and other forms of frequency modulation.

The vertical transitions corresponding to reflection and refraction happening in the time domain are shown with the purple arrows in Fig. 2.1(c) and (d), highlighting the similarity between spatial and temporal modulation of permittivity when compared to the horizontal transitions from spatial modulation (blue arrows). This new class of transitions unlock applications

such as coupling to modes below the light-line or parametric amplification [35, 36].

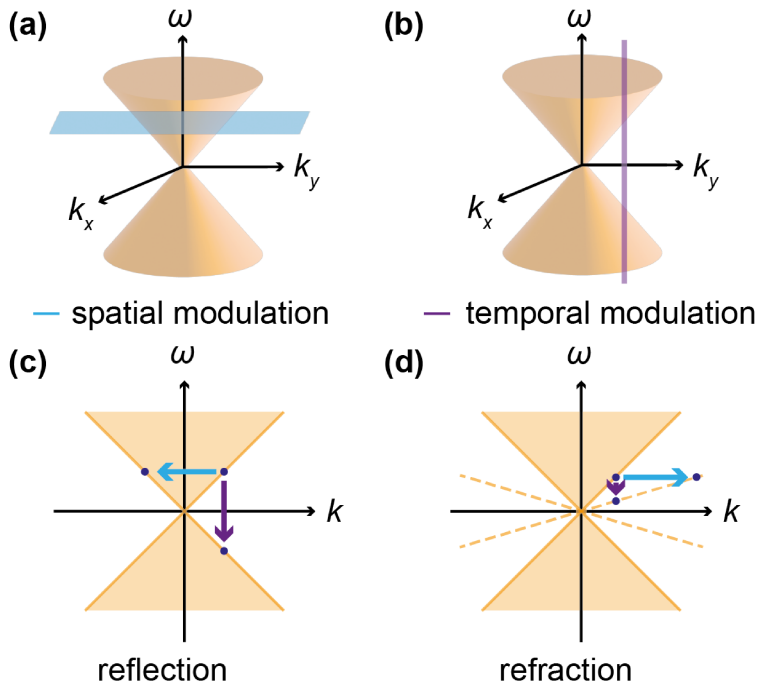

Figure 2.1: Spatial and temporal transitions in the light cone perspective. **(a)** Spatial transitions allowed by spatial modulations in the (x, y) plane (light blue plane) with regards to the light cone (in orange). All transitions are normal to the frequency axis. **(b)** Temporal transitions allowed by modulations in time (purple line) with regards to the light cone. Transitions are now normal to the (k_x, k_y) plane. **(c,d)** Transitions in the case of spatial (light blue arrows) and temporal (purple arrows) modulations in the dispersion diagram. (c) Reflection is characterised by a change in sign of the k component for a spatial transition (light blue arrow) and ω component for a temporal transition (purple arrow), while (d) refraction corresponds to a respective horizontal (spatial transition, blue arrow) or vertical (temporal transition, purple arrow) shift to the corresponding new light dispersion (dashed orange line) due to a change of permittivity.

Yet, similarity between spatial and temporal modulation does not mean equivalence and it is necessary to look further into basic cases to derive some first principles. Let us first consider the case of time refraction and reflection (see also *Theory of photon acceleration* [15] for the geometrical and full wave formalism), in the case of an infinite, homogeneous medium seeing an abrupt change of refractive index in time as depicted in Fig.2.2(a).

$$n(t) = \begin{cases} n_1 \text{ if } t < 0 \\ n_2 \text{ if } t > 0 \end{cases} \tag{2.1}$$

Due to spatial translation invariance, the momentum of the wave k is conserved. As the momentum is defined as $k = \omega(t)n(t)/c$, and defining $\omega_1 = \omega(t < 0)$ and $\omega_2 = \omega(t > 0)$, we have

$$n_1\omega_1 = n_2\omega_2 \tag{2.2}$$

We thus have simply obtained the frequency of the time refracted wave. Equation 2.2 is valid for any modulation in time in the asymptotic case $t \to +\infty$, as long as the modulation of permittivity and thus refractive index converges towards a final value n_f, i.e. $n \xrightarrow[t\to+\infty]{} n_f$. Note that a difficulty in practical experiments is the finite time of the interaction of the wave in the medium, which will put constraints on the modulation speed. These constraints will be further discussed below when moving on from a geometric to a full-wave approach.

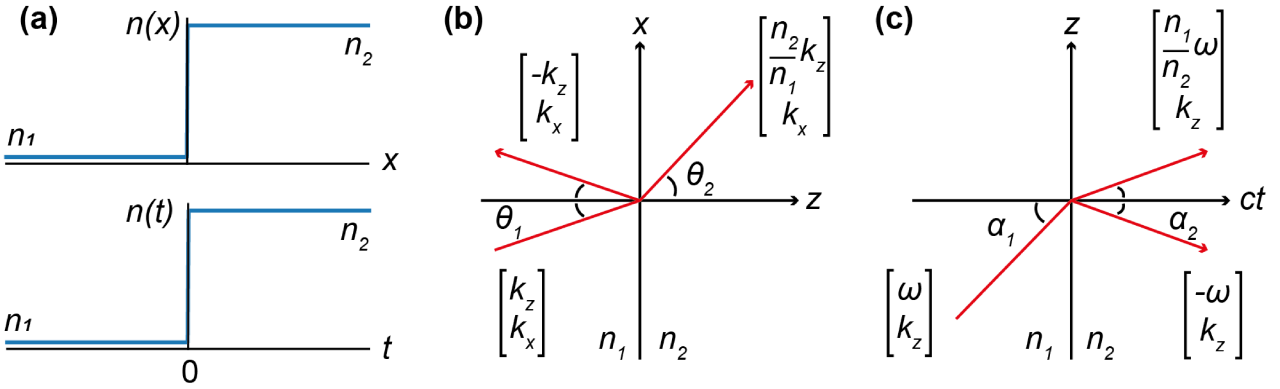

Figure 2.2: From space to time: the example of time refraction. **(a)** Step index change in space (top) and time (bottom). The change from index n_1 to n_2 is instantaneous. **(b)** Refraction diagram in the case of spatial refraction, the z component of momentum is modulated while the x component is conserved. **(c)** In temporal refraction, the frequency ω is modulated and a refracted and reflected wave appear just as in the spatial case.

Equation 2.2 is an inverse form of Snell's law, where $k_1/n_1 = k_2/n_2$, and confirms the strong similarity between the spatial and temporal domains. To push the analogy further, we can define an angle α in the (z, ct) plane just as we define the angle θ in the (x, z) plane for spatial refraction. With $\sin(\theta) = k_x/k_z$ as shown in Fig. 2.2(b), Snell's law gives $n_1 \sin(\theta_1) = n_2 \sin(\theta_2)$. In the same way we define $\tan(\alpha) = 1/n$ (see Fig.2.2(c)), which gives the temporal equivalent of Snell's law of refraction:

$$\omega_1 \tan(\alpha_2) = \omega_2 \tan(\alpha_1) \tag{2.3}$$

An important result from equation 2.3 is the absence of total internal reflection: while a critical angle θ_c can be defined for spatial refraction, equation 2.3 is always satisfied for positive refractive indices. This shows there is no such thing for a wave as being reflected by a temporal interface and going back in time. As we will now show with full wave optics, partial reflection in time does not contradict this.

Deriving the time domain Fresnel coefficients for a temporal interface with the Heaviside profile shown in Fig.2.2(a) is similar to the derivation for the spatial domain: starting from a wave propagating along z with moment k and frequency ω_i:

$$\mathbf{E}(z,t) = \begin{cases} \mathbf{E_i} e^{i(kz-\omega_i t)} \text{ if } t < 0 \\ \mathbf{E_r} e^{i(kz-\omega_r t)} + \mathbf{E_t} e^{i(kz-\omega_t t)} \text{ if } t > 0 \end{cases} \tag{2.4}$$

Satisfying the dispersion of the medium requires:

$$\begin{cases} \omega_i = \frac{kc}{n_1} \\ \omega_r = -\omega_t \\ \omega_t = \frac{n_1}{n_2}\omega_i \end{cases} \tag{2.5}$$

The negative sign of ω_r in partial time reflection is misleading: the wave is not going back in time and violating causality, but rather it appears to do so and time continues to flow in the usual direction. This is due to the equivalence between a wave and its complex conjugate in their complex representation: the combination $(k, -\omega_r)$ comes back to $(-k, \omega_r)$ i.e. a reflected wave travelling in the negative direction.

Pushing the derivation further, the continuity of the displacement and magnetic fields in time require $\mathbf{D}(t \to 0^-) = \mathbf{D}(t \to 0^+)$ and $\mathbf{B}(t \to 0^-) = \mathbf{B}(t \to 0^+)$. Rewriting $\mathbf{D}$ and $\mathbf{B}$ in terms of $\mathbf{E}$ we get a set of two equations relating the reflected and transmitted field to the incoming field, that can be rearranged to give us the time-varying Fresnel coefficients:

$$\begin{cases} r = \frac{E_r}{E_i} = \frac{\eta}{2}(\eta - 1) \\ t = \frac{E_t}{E_i} = \frac{\eta}{2}(\eta + 1) \end{cases} \tag{2.6}$$

where $\eta = n_1/n_2$. As a consequence, $|r|^2 + |t|^2 \neq 1$ unless $n_1 = n_2$ i.e. any change in refractive index, as expected, breaks conservation of energy. Notably, if $n_2 \ll n_1$ one can expect large enhancement of the time reflected and transmitted field amplitudes, corresponding to a transfer of energy from the medium (and the modulation) to the wave. This is another stark contrast from conventional spatial structuring of permittivity, and shows the potential of photonic time-varying media for frequency control.

2.1.2 Phase and frequency shifting

So far, important information on time refraction and an overall taste of time-varying optics have been obtained by considering the simple picture of an instantaneous change of permittivity. In real systems, the permittivity will change within a finite time, with a specific slope which will affect the propagating wave's frequency changes. To understand the role of the timescale of the modulation, let us now consider the case of a monochromatic plane wave interacting with a medium having a S-parameter matrix with coefficients S_{ij} (as shown in Fig. 2.3(a)). The scattering matrix S describes how light impinging on a system will interact and be scattered by the medium, with the various incoming and outgoing fields being related by the S-parameter coefficients S_{ij}.

If the medium is evolving in time we can add a temporal evolution to the S-parameter matrix and its individual coefficients $S_{ij}(t)$ and using complex representation for these coefficients, we write $S_{ij}(t) = a_{ij}(t)e^{i\psi_{ij}(t)}$. An output signal from the medium will then take the form of a linear combination of $E_{out}^{(j)} = S_{ij}(t)E_{in}^{(i)}$. Assuming all input fields are time harmonics $E_{in}^{(i)} = E_i e^{i\omega_0 t}$ where ω_0 is the original frequency of the wave the output S_{ij} is now $a_{ij}(t)E_i e^{i(\omega_0 t+\psi_{ij}(t))}$. As the instantaneous frequency is the derivative of the phase of a wave with respect to time, we express the instantaneous change of frequency as:

$$\delta\omega(t) = \frac{\mathrm{d}\psi_{ij}(t)}{\mathrm{d}t} \tag{2.7}$$

As equation 2.7 simply shows, changes in frequency are directly related to changes of the medium's optical properties, and this can be seen as the medium imparting phase and amplitude to the wave (see Galiffi et al. [37] for a more rigorous theoretical framework). For example for a Gaussian modulation of the S-parameter matrix phase as shown in Fig. 2.3(b), a trace in the form of its derivative will be found in the instantaneous frequency $\omega(t)$ (Fig. 2.3(c)). We find the conditions for a strong frequency content modulation: $\delta\omega(t) \sim \omega_0$ if $\delta\psi \sim \pi$ and $\delta t \sim 2\pi/\omega_0$, i.e. strong effects come from significant phase changes on timescales similar to the optical period of the pulse. This is a challenging aspect of time-varying physics at visible and NIR frequencies, as the timescales need to be of the order of 1-10 fs, which is unattainable by any other means of modulation than all-optical. Additionally, obtaining strong amplitude modulation in Nanophotonic systems is difficult due to the small volume and distances offered by such media limiting propagation effects and the perturbative scale of optical modulation in most materials. This will be tackled in this thesis using Nonlinear Optics, novel materials and

ultrafast pulses (see section 2.2).

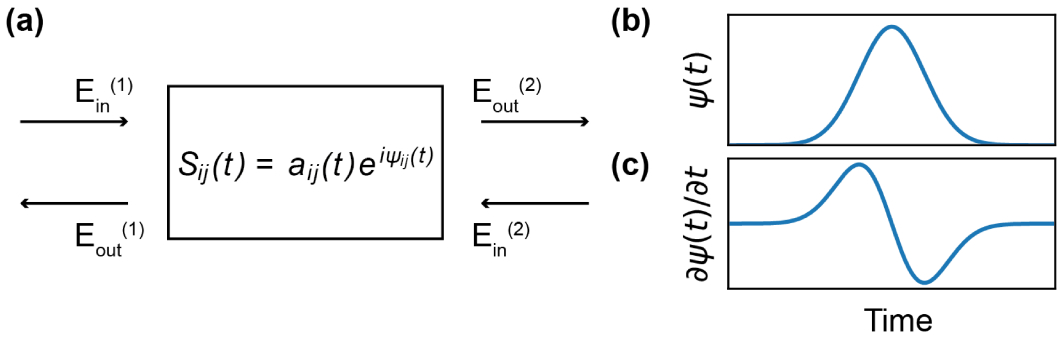

Figure 2.3: A S-parameter approach to the role of phase in frequency shifts. **(a)** Diagram of a S-parameter matrix, with its input and output fields related by $E^i_{out} = \sum S_{ij} E^{(j)}_{in}$. **(b)** S-parameter matrix phase as a function of time in the case of a Gaussian modulation. **(c)** Resulting phase derivative and frequency shift from a Gaussian modulation of the S-parameter matrix phase.

A final layer of complexity can be found in the symmetry of the modulation $\psi(t)$. We experimentally collect a field using a detector with a finite integration time, which in our case will be much longer than the modulation and optical pulse width timescales (at least 100 ms versus timescales below 1 ps). Equation 2.7 depicts an instantaneous frequency, and needs to be integrated over time to give the final frequency shift resulting from the modulation. As an example, for a temporal interface represented by a Heaviside function in space

If the input field amplitude stays constant throughout the modulation, we have an integral of the phase shift in time as a resulting measured frequency shift [37].

In the case of a symmetric modulation of phase in time such as the Gaussian presented in Fig. 2.3(b,c), no phase shift will be measured. Only a broadening will be measured, of which an example can be found in self phase modulation for the optical Kerr effect with a Gaussian pulse. A degree of asymmetry, be it due to a change in amplitude of the input field with time or an asymmetry of the temporal modulation, is necessary to measure a frequency shift in the experimental conditions presented in this work. We will see in chapter 4 that the strongest time-varying effects come about at the point of highest temporal asymmetry.

Of course the model presented here is too simple to capture the full physics of time-varying media. It neglects key factors such as causality (light modulated at a time t might not leave the system immediately and keep on being modulated at a time $t + \delta t$) or dispersion (in a pulse with a given spectral width, different frequencies might not be modulated the same way). This calls for a formalism embracing the finer features of time-varying effects, which will be discussed in section 2.3.

The space-to-time analogy, with the twists explained above, will be our intuitive guide when designing new time-varying systems. Here, the choice of working in all-optical nanostructures aims at leveraging specific advantages: the strong field confinements achievable in Nanophotonics, matched with the relaxation of certain spatial constraints such as phase-matching or group-velocity mismatch, lowering the effects of propagation and dispersion, make a favorable environment to study temporal-only effects by reducing the available degrees of freedom in space. Nonlinear Optics provides a unique platform to achieve ultrafast modulation, to reach the timescales so important for time-varying effects shown in equation 2.7. Let us now focus our attention on the materials and nanostructures we will use to perform new time-varying experiments.

2.2 Epsilon-near-zero media in Nonlinear Nanophotonics

2.2.1 Nonlinear Nanophotonic materials for time-varying media

The period of an optical cycle in the visible and NIR is of the order of 1 to 5 fs. It is thus necessary in order to observe sizeable time-varying effects to obtain medium modulation timescales of the order of the fs, and in this Nonlinear Optics makes a prime platform. Through nonlinear orders of the material susceptibility, an optical pulse can induce changes in the permittivity: let us consider the classic development of Nonlinear Optics following an expansion of the polarisation in the medium as a function of the vector electric field $\mathbf{E}$ and the susceptibility tensor $\tilde{\chi}^{(n)}$ [28, 38].

$$\mathbf{P} = \epsilon_0 \left(\tilde{\chi}^{(1)}\mathbf{E} + \tilde{\chi}^{(2)}\mathbf{E}^2 + \tilde{\chi}^{(3)}\mathbf{E}^3 + ... \right) \tag{2.8}$$

Considering third order effects only with a scalar field $E(t) = E_w(t)\cos(\omega t)$ and susceptibility $\chi^{(n)}$, the polarisation can be rewritten as

$$\begin{aligned} P &= \epsilon_0 \left(\chi^{(1)} + \frac{3}{4}\chi^{(3)} E_w(t)^2 \right) E(t) + ... \\ &= \epsilon_0 \epsilon_r(t) E(t) + ... \end{aligned} \tag{2.9}$$

This shows that Nonlinear Optics can provide changes in the permittivity of a medium over

the time scale of a pulse's envelope. Other terms in the polarisation have been ignored as they present fields at different frequencies than the original and thus do not contribute to the permittivity modulation. Using ultrafast lasers with pulse durations of the order of 10-100 fs full width at half maximum (FWHM), and with a choice of the right nonlinear material and architecture, one can thus induce strong changes in permittivity on the pulse timescale, satisfying the conditions for efficient temporal modulation.

Recent advances in Nanophotonics have provided us with many potent materials for Nonlinear Optics. Metals, at the center of the early push in Plasmonics, offer good nonlinear properties as well as useful plasmonics resonances, but their use is severely limited by their high losses and low damage threshold [39, 40]. 2D materials offer many exotic and useful properties, as single layers, bulk or multilayered structure, but haven't reached full maturity yet for Nonlinear Optics. Single layers are limited by their small volume and interaction time, but the control of nonlinear properties and switching in multilayered media and heterostructures has now been established and applications in time-varying physics are sure to follow [41–44].

This leaves us with the two main photonic time-varying platforms: high index dielectrics and ENZ materials, both offering strong nonlinear properties. High-index dielectrics offer rich resonance engineering [45–47] but have a lower comparative change in permittivity than ENZ materials. We will further discuss and investigate a high-index dielectric, Gallium Phosphide (GaP), in chapter 6. The majority of this work is rather focused on time-varying effects in an ENZ medium, which we will now introduce.

2.2.2 Linear properties of transparent conducting oxides

ENZ materials provide rich physics at the frequency where the real part of their permittivity crosses zero, allowing for plasmonic resonances, relaxed phase-matching in Nonlinear Optics and other applications such as slow light or levitation [48–50]. ENZ materials are of particular interest when their losses at the ENZ point are comparatively low, and the frequency at which the crossing happens (that we will refer to as the ENZ frequency) is in the range of interest (visible to NIR). Degenerately doped semiconductors known as transparent conducting oxides (TCO) draw our interest as they satisfy these conditions (green diamonds in Fig.2.4). As will be shown in the following section 2.2.4, TCOs and in particular ITO have proven to be an excellent platform for time-varying experiments.

The ITO layers measured in this work were either purchased from Präzisions Glas & Optik GmbH or deposited within the nanofabrication facilities of the Nanoinstitut München at

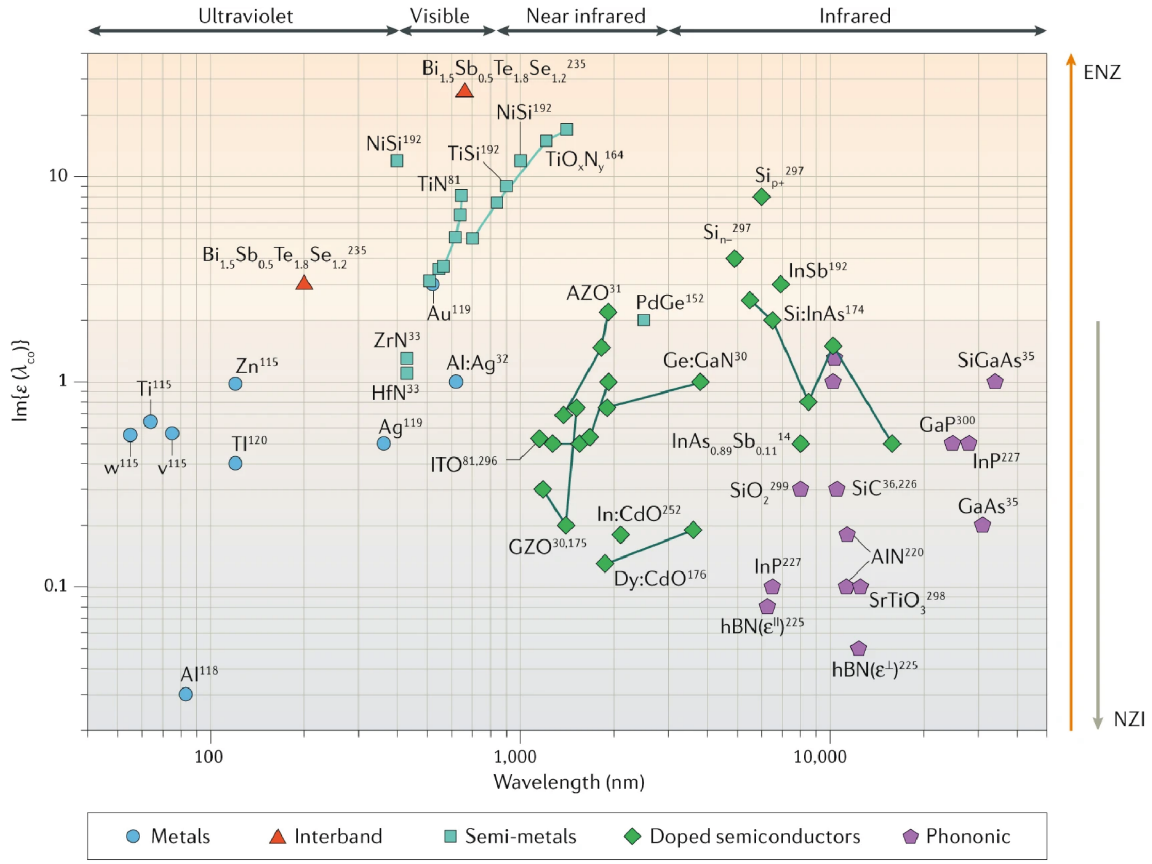

Figure 2.4: Overview of ENZ materials. The imaginary part of the permittivity is shown on the vertical axis, against the ENZ wavelength on the horizontal axis. As losses go towards zero, the material will be dubbed near zero index (NZI), a class of materials that will not be discussed in this work. Reused with permission from [48].

Ludwig-Maximilians-Universität München by Benjamin Tillman. ITO layers, as well as amorphous GaP layers are deposited using RF magnetron sputtering with an Angstrom Engineering Amod. Key elements in the control of the ENZ frequency and losses of the medium are the thickness of the deposited layer as well as the evaporation temperature and rate. When performing successive deposition of layers of different materials, a cool down of the instrument heating chamber is useful in order to preserve the properties of the ITO layer, and prevent the formation of some alloy between ITO and its neighboring materials.

As shown in 2.5, if nanostructuring is required a PMMA layer is spin-coated onto the film, and an electron-beam lithography will induce scission in exposed areas thus creating a positive mask. The exposed PMMA is removed during development using methyl isobutyl ketone and isopropanol. This first mask will enable the creation of a second positive mask using sputtered gold, with the remaining PMMA being removed using acetone. The sample will then undergo reactive ion etching to structure the layers using gold as a hard mask. Chemical etching is then used to remove the gold. Reactive ion etching being a dry-etching, 'aggressive' method of

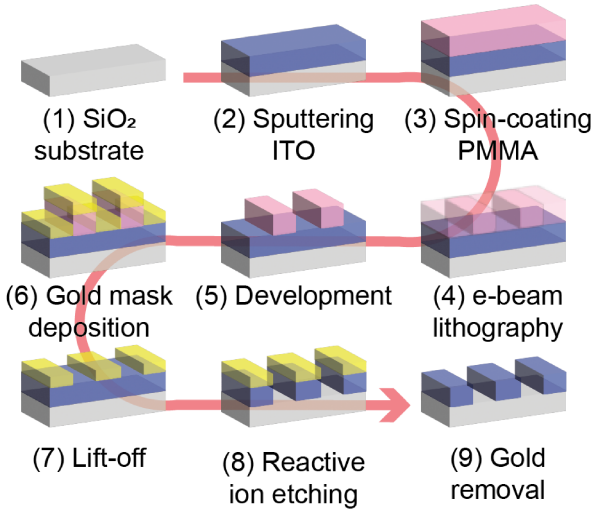

Figure 2.5: Fabrication process of ENZ materials. (1) A SiO_2 is used as a substrate, on which (2) an ITO layer is deposited using RF magnetron sputtering. (3) For further nanostructuring, Poly(methyl methacrylate) (PMMA) is then spin-coated onto the ITO and (4) put under an electron beam, creating a positive mask that will be removed under (5) development. (6) A gold layer is then deposited above the PMMA structure and (7) lift-off creates a second positive mask. (8) The ITO is then structured using reactive ion etching and (9) the gold mask is then removed with wet etching, leaving the patterned nanostructure on the substrate.

structuring, it provides a high wall aspect ratio and little under-etching.

As ITO will be the principal material used in this work, we will now introduce its optical and electronic properties further. The permittivity of ITO in the NIR range can be well described by a simple Drude-Lorentz model as for metals. Defining ω_p as the plasma frequency, γ as the dissipation rate and ϵ_∞ the permittivity at infinity, the complex relative permittivity of ITO, as shown in Fig.2.6 is then given by [51, 52]:

$$\epsilon_r(\omega) = \epsilon_\infty - \frac{\omega_p^2}{\omega^2 + i\omega\gamma} \tag{2.10}$$

Note that throughout this work frequencies noted with f will be referring to natural frequency units, while the use of the symbol ω will refer to radial frequencies i.e. $\omega = 2\pi f$. ω_p and γ are then also scaled appropriately depending on the convention in use.

Another fact to take note of is that ϵ_∞ is an approximation in the frequency range of interest, in truth it can be modelled by a Lorentzian resonance in the ultraviolet range [53, 54] corresponding to the background from the bound electrons. This will be important when considering harmonic generated light at higher frequencies in chapter 6.

The curves shown in Fig.2.6(a) correspond to the permittivity of one of the samples studied in this thesis (see chapter 3), a 40 nm ITO thin film deposited on glass. One can see the permittivity crossing zero in the NIR at 227 THz (1320 nm in terms of free space wavelength),

while losses remain comparatively low with a value of 0.42. The range of frequencies near the crossing point is referred to as the ENZ region. In terms of refractive index (Fig. 2.6(b)), the ENZ point is not a near-zero-index point though the real refractive index is indeed low with a value of 0.46 crossing that of its losses.

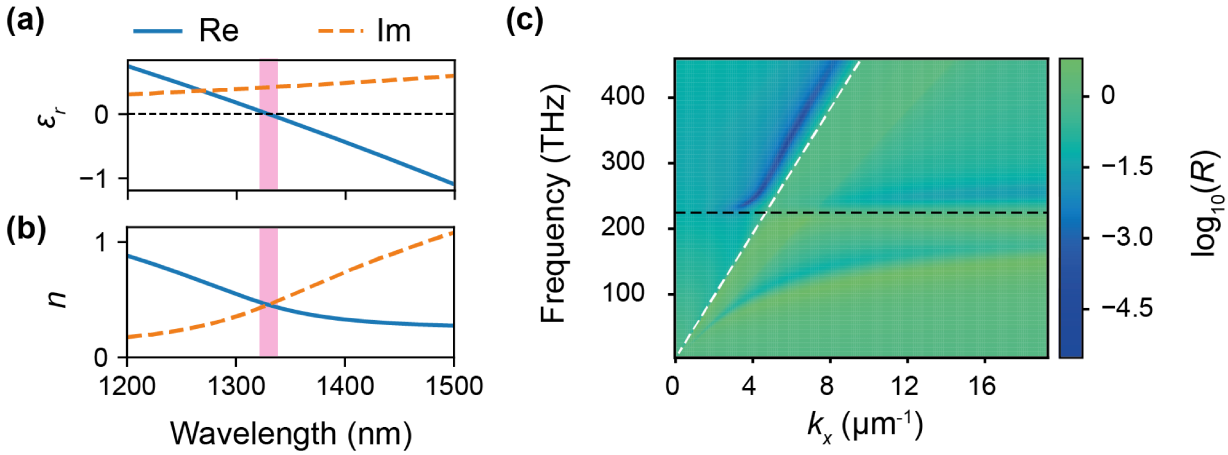

Figure 2.6: Linear properties of a 40 nm thick ITO slab on glass. **(a)** Relative permittivity of the 40 nm ITO thin film used in this work: the real part (blue line) crosses zero in the NIR while the imaginary part (dashed orange line) is non-zero due to the Kramers-Kronig relations. **(b)** This is translated into a crossing between the real (blue line) and imaginary (dashed orange line) parts of the ITO refractive index. **(c)** Computed dispersion diagram of the ITO on glass system: reflectivity R as a function of frequency and in-plane momentum k_x, the Berreman mode is visible in dark blue above the light line (dashed white line). The ENZ mode, along the ENZ frequency (dashed black line), and the short range surface plasmon are visible below the light line.

The ENZ region opens access to resonances above and below the light line in ITO thin films and multilayered structures. Below the light line (diagonal dashed white line in Fig2.6(b)), as for any material whose permittivity is crossing zero, ITO exhibits short and long range surface plasmon resonances (lower bright lines in Fig2.6(c)) [55, 56]. The long range plasmon is then usually referred to as the ENZ mode, due to its convergence towards the ENZ frequency as the layer gets thinner [55]. Above the light line, one can access a guided mode (upper bright line in Fig2.6(c)) using momentum matching by tuning the angle and polarisation of the impinging light. The resonance exists for angles close to the Brewster angle, and is usually referred to as the Berreman mode (though other designations exist). The Berreman mode will be used in this thesis to couple light to the ITO layer, enhance the electric field and drive a stronger modulation efficiency and amplitude as will be shown in chapter 3. Let us now look into the modulation mechanism and the importance of the pumping optical pulse.

From the Drude-Lorentz model we know

$$f_p = \frac{1}{2\pi}\sqrt{\frac{Ne^2}{\epsilon_0 m_e^*}} \tag{2.11}$$

where N is the free-carrier density of the electron gas, e the electron charge, ϵ_0 the permittivity of vacuum and m_e^* the electron effective mass. We can also derive the frequency f_{ENZ} at which the permittivity is zero i.e. $\mathrm{Re}\left(\epsilon_r(f_{ENZ})\right) = 0$ under the assumption of negligible scattering of electrons i.e. $f_p \gg \gamma$:

$$f_{ENZ} = \frac{f_p}{\sqrt{\epsilon_\infty}} \tag{2.12}$$

Now equipped with the knowledge of the linear properties of ITO, we can turn towards the mechanisms behind optical modulation of permittivity in the material.

2.2.3 Photocarrier excitation in Indium Tin Oxide

Under optical pumping, the modulation can happen through electronic transitions to real states (e.g. photocarrier excitation) or virtual states (e.g. SHG). The first case offers a higher modulation efficiency but exhibits timescales limited by the medium's material properties, while the latter offers much faster modulation speeds at the cost of interaction strength [57]. Hence, the choice of material and illumination architecture is key in making a time-varying medium, by determining which of these processes will be used and as a consequence the modulation strength and speed. In ITO the fast nonlinearities linked to virtual state transitions are estimated and measured to be 2 orders of magnitude below the slow nonlinearities from photocarrier excitation (see references [57] and [53] as well as chapter 6), so the latter will be the focus of study here.

Equations 2.11 and 2.12 give us insight on how photocarrier excitation can change the permittivity of ITO. Let's consider the band structure of ITO in the unperturbed regime (Fig.2.7(a)). The arrival of an intense pump pulse will disturb the electronic distribution depending on its carrier frequency: for energies above the band gap, interband transitions will dominate as shown in Fig.2.7(b). By depleting the valence band and filling the conduction band, the free-carrier density N of ITO increases which in turns blueshifts the plasma frequency and hence the ENZ frequency, i.e. the medium becomes more metallic. In comparison, for energies below the band gap intraband transitions will dominate, as shown in Fig.2.7(b). The electrons will be non thermalised for a few fs before relaxing into hot electrons via electron-electron scattering [58]. This will raise the Fermi level to higher energies and increase the electron mass due to the non-parabolicity of the conduction band. This will in turn redshift the ENZ

frequency and shift ITO towards the dielectric regime. Note that the electron scattering will also be affected by the optical pumping, though it cannot be modelled in an easy way, thus affecting the electron scattering rate γ. Finally, the electrons will relax through electron-phonon scattering, with additional pathways in the case of interband transitions as illustrated in Fig. 2.7(c) (band to band transitions, trap-assisted transitions with mid-gap defect states, Auger recombination) [59].

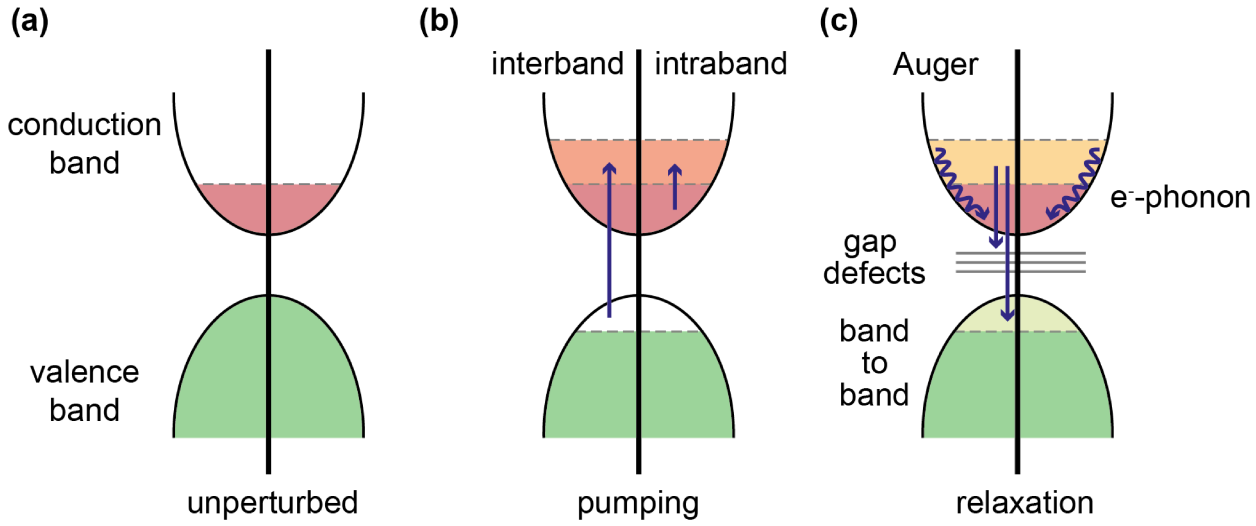

Figure 2.7: Photocarrier excitation and relaxation mechanisms in ITO. **(a)** Band diagram for an unperturbed ITO medium. **(b)** Under pumping, the electrons will undergo intraband or interband transitions depending on the pump frequency, leading to different electron cloud distributions in the conduction band. **(c)** The system will relax to its natural state through various means depending on the availability of states below the conduction band.

The two-temperature model is often used to describe the dynamics of the medium [53], allowing to show the dynamics of electrons within the medium with the dissipation of energy of the electrons through the lattice. This is illustrated in Fig. 2.8(a) with the slow decay over time of the electronic temperature, simultaneous to the rise of the lattice's. Wang et al. extracted the changes in ω_p and γ in an ITO thin film using pump-probe spectroscopy in transmission and reflection coupled with transfer matrix method (TMM) and the Levenberg-Marquardt optimisation algorithm [58], demonstrating the modulation of both coefficients (see Fig. 2.8(b)). This change in material properties and thus permittivity is then directly observable in the transmittivity or reflectivity of the thin films, which was recorded notably in Alam et al.'s seminal paper [53], with a non-perturbative change in transmission being recorded with short timescales under all-optical pumping as shown in Fig. 2.8(c).

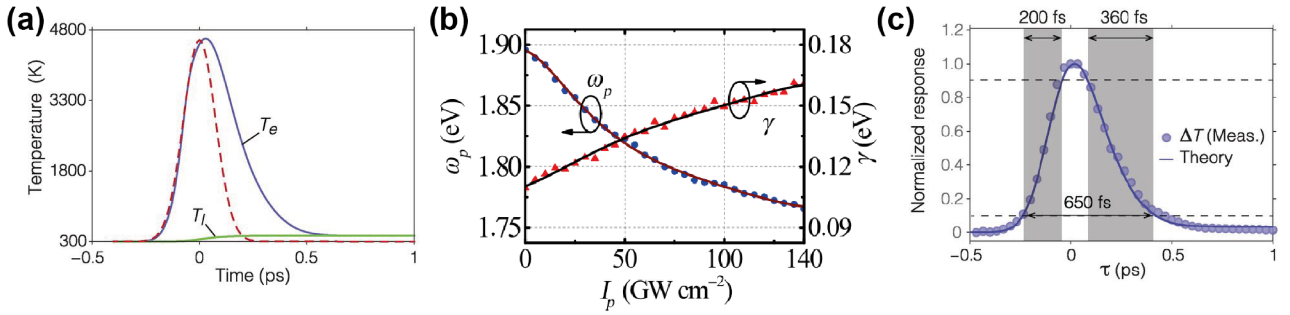

Figure 2.8: Changes in ITO electronic properties under intraband optical modulation. **(a)** Modelled free electron (T_e, in blue) and lattice (T_l, in green) temperature changes as a function of time under optical illumination of an optical pulse (dashed red curve) for a 310 nm ITO thin film using a two-temperature model. **(b)** Modelled changes in plasma frequency (blue curve) and electronic damping factor (red curve) as a function of peak modulation intensity in a different 220 nm ITO thin film. **(c)** Measured and modelled change in transmittivity as a function of time in the 310 nm ITO under optical illumination. Panels (a) and (c) reused with permission from [53], panel (b) reused with permission from [58].

2.2.4 Experimental demonstrations of time varying effects in transparent conducting oxides

Alam et al.'s work in 2016 [53] was seminal in the establishment of ITO as a time-varying platform. It demonstrated the high Kerr nonlinearities of the material, by measuring a shift in refractive index of the order of unity, beyond the perturbative regime where $\delta n \ll n$. Soon after came a similar result using another material, Aluminium-doped Zinc Oxide (AZO) (another TCO with very similar properties to ITO but with comparatively larger losses) [60, 61]. Time-varying experiments soon followed: time refraction [62–67] and reflection [68, 69] were demonstrated by pumping the medium under ultrafast pulses in the NIR. As a benchmark, Liu et al. reported a 1.8 THz shift at 140 GW/cm^2 in a 80 nm thin film [66].

Other works focused on better understanding the mechanisms and other materials/geometries that can be used for ultrafast modulation in ENZ materials [52, 70–75]. To achieve higher field intensities and phase changes via strong coupling between antennas and an ITO thin film, gold nanoantenna metasurfaces were made and investigated [69, 76–78]. This yielded a higher efficiency in field confinement and frequency shifting, but lowered the damage threshold of the system as gold antennas support much lower intensities than ITO. Pang et al. report a frequency shift of 6.8 THz for gold antennas with an electric dipole resonance on a 65 nm ITO layer, for an intensity of 2 GW/cm^2 [78] - thus presenting a much higher shifting efficiency than in bulk thin films.

Pump probe experiments are common in characterising time-varying effects: a pump pulse

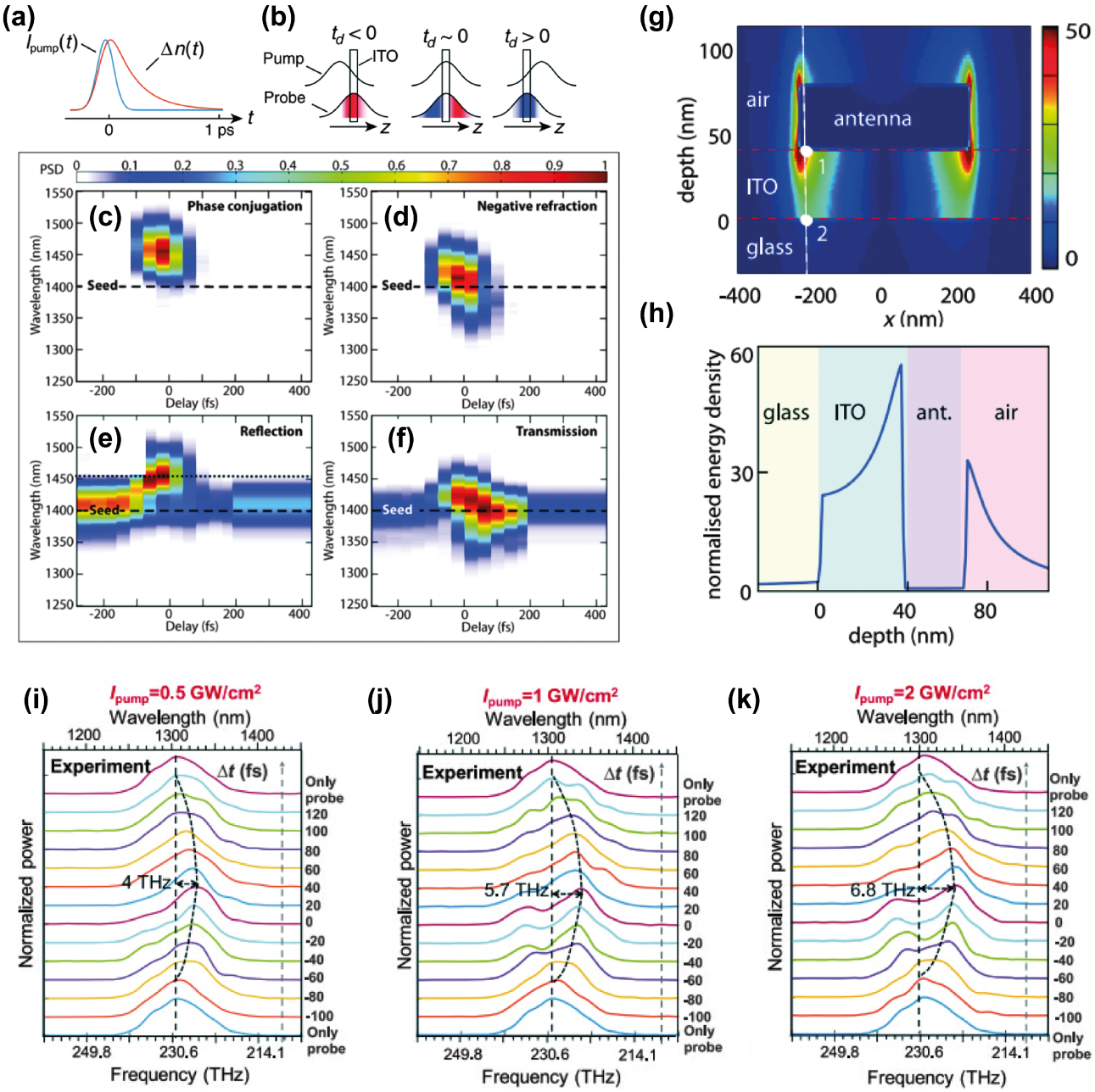

Figure 2.9: Review of demonstrated time-varying effects in ENZ nanostructures. **(a,b)** Mechanism for experimental realisation of time refraction in ITO in a pump probe measurement. (a) Diagram of the temporal modulation of refractive index in ITO (red line) by an ultrafast pump pulse (blue line). (b) A probe pulse will undergo a redshift if arriving on the rise of the modulation, and a blueshift when arriving on the decay of the modulation. **(c-f)** Time varying effects in a 500 nm thick AZO slab pumped by 105 fs pulses at high energy (770 GW/cm^2): phase shifts are visible in (c) phase conjugation, (d) negative refraction (e) reflection and (f) transmission. **(g,h)** Role of gold antennas in time-varying effects: (g) FDTD simulation of a gold antenna whose resonance crosses the ENZ frequency of the ITO thin film beneath. (h) Field distribution as a function of sample depth, showing the enhanced coupling of light to the ITO layer. **(i-k)** Frequency shift in a gold antenna on ITO metasurface at pump powers of (i) 0.5 GW/cm^2 (j) 1 GW/cm^2 (k) 2 GW/cm^2. Reused with permission from (a,b) [64], (d-f) [63], (g,h) [69] and (i-k) [78].

with high intensity induces a change in refractive index within a nonlinear system (a TCO layer in Fig. 2.9), and a weak probe pulse interacts with the medium and undergoes frequency modulation from the fast change in time, as shown in Fig. 2.9(a,b). For example, time refraction can be measured not only in transmission and reflection as Fig. 2.9(c-f) shows, but also in newly generated time-varying signals - here a phase conjugate and a negatively refracted beam in a time-varying AZO layer, with a maximum shift in reflection of 7.4 THz at 770 GW/cm^2. To achieve higher efficiency in frequency shifts, the use of a gold antenna's plasmonic resonance, if tailored to be spectrally close to the ENZ frequency of an ITO thin film below, will increase the coupling and average field intensity within the layer (as shown in Fig. 2.9(g,h)). This leads to large frequency shifts at much lower pump intensities as can be seen in Fig. 2.9(i-k), where a shift of 6.8 THz is achieved with only 2 GW/cm^2.

In view of the strong and promising modulations reported so far in literature, ITO is a logical choice of platform for the time-varying phenomena we hope to investigate. Now that we have gained an understanding of our time-varying media in general and of the experimental platform that are ENZ materials, we must now turn to the theoretical tools that can be used to gain a better understanding of the physics of our time-varying media.

2.3 Modelling of time-varying media

2.3.1 Phenomenological approach

The significant rise of time-varying materials over the recent years stirred much interest from theoreticians and computational physicists, while experimentalists developed models to further explain their results. While there is no such thing as a better theory, some theoretical models serve their purpose better than others, depending of course on said purpose (as depicted in Fig. 2.10). In this thesis, we aim at exploring new physics in photonic time-varying media made with ITO thin films. This would place us at the intersection of condensed-matter theory and more general time-varying theory, but we will prefer a qualitative and intuitive approach to modelling our systems. Though we will draw inspiration from the Drude model and intraband transitions described in section 2.2.3, and have tried the model presented in Bohn et al.'s work [52, 79] against our data, our main tool for modelling time-varying structures will be a Fourier transform of a pulse bearing the mark of the temporal modulation in its amplitude and phase.

The reason behind this choice of modelling time-varying effects with a Fourier transform lies within the choice of time-varying system that will be presented here. In this thesis, we

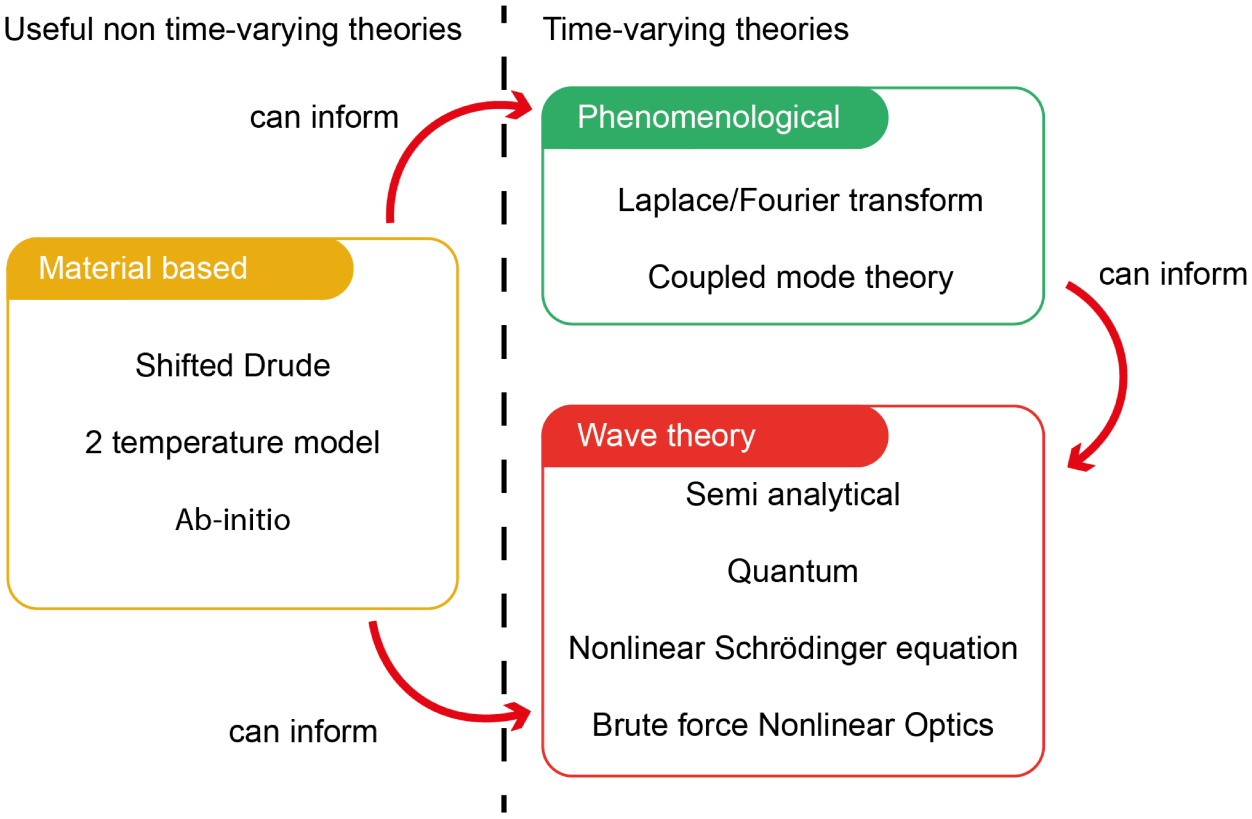

Figure 2.10: A summary of theories used for modelling all-optical time-varying media. Material based theories allow for a prediction of the changes within the material, which in themselves are not enough to model time-varying effects. A phenomenological or full wave theory are necessary to address the changes in frequency content. See the following references for the following models: shifted Drude [76, 79], 2 temperature model [76], ab-initio [80], Fourier [81], Laplace [82], semi-analytical [67, 79], quantum [83], nonlinear Schrödinger equation [53], nonlinear optical [54].

wish to study a time-varying mirror: an interface, presenting no spatial propagation, whose reflectivity can be instantaneously turned on ($R = 1$) and off ($R = 0$), over times shorter than the temporal width of the pulse which we desire to modulate. As shown in Fig. 2.11(a) and (b), though a regular mirror will only reflect the illuminating pulse, the fast change of reflectivity of the mirror from a fast change in the medium's permittivity will lead to new frequencies being generated within the pulse. Thanks to the absence of propagation within the medium when the mirror is on and the overall absence of causality in such a system, the Fourier transform allows to extract the generated spectrum from the temporal modulation.

The phenomenological model presented in this thesis is very similar to that used with the S-parameter matrix in section 2.1.2, and in the same manner does not account for the dispersion of the reflectivity i.e. the frequency dependence of $A(t)$. Consider a probe electric field with any particular shape in time $E(t)$, for example two consecutive pulses with different carrier frequency as shown in Fig. 2.12 (an approximation of a highly chirped pulse) or a single width-limited pulse as shown in Fig. 2.12(b). It interacts with an interface with a complex temporal

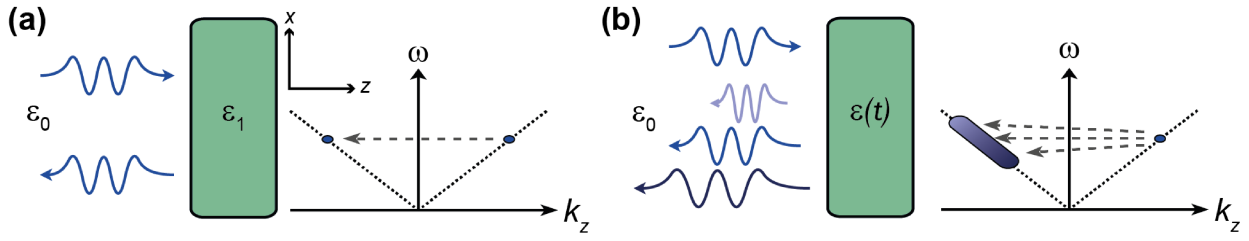

Figure 2.11: Diagram of the time-varying mirror. **(a)** A conventional mirror reflects light due to the permittivity mismatch at the interface, inducing a horizontal transition in the dispersion diagram. **(b)** A time-varying mirror will reflect light upon activation, thus creating new frequencies with regards to the incoming light's spectrum. Reproduced from [79].

aperture function $A(t)$ such that the wave, after interaction with the interface can be expressed as $A(t) \times E(t)$. In the absence of dispersion (all frequencies observe the same aperture $A(t)$), the time-modulated signal $S(f)$ can be expressed as:

$$S(f) = \mathrm{FT}\left[A(t) \times E(t)\right](f) \tag{2.13}$$

What would take the role of the aperture function in our ITO-based systems? In nanophotonic systems, structures are often measured on reflection or transmission from an impinging beam. The complex transmission and reflection coefficients of the structure inform us on the phase and amplitude imparted to the incoming light. In this work we will take a particular look on reflection, but all following equations are equally valid in transmission. The complex reflection coefficient $r(t)$ will here act as an aperture function, we will express it in its complex form as $r(t) = \rho(t)e^{i\phi(t)}$ where $\rho(t)$ and $\phi(t)$ are respectively its amplitude and phase.

Let us imagine the case of a mirror that can instantly be switched ON and OFF, as depicted in Fig. 2.12(c) - that is when $|r| = 1$ during a temporal interval and $|r| = 0$ the rest of the time. Then, a pulse arriving on an ON will be reflected and collected in $S(f)$, while a pulse arriving in OFF will not be sent back, as shown in Fig. 2.12(e). This is a first example of how the amplitude of the complex reflection coefficient can affect the frequency content of an electric field. In more general cases, the aperture amplitude function is generally connected to the width of the modulated pulse.

The role of the reflection coefficient's phase lies in the shifting of the frequencies. A first example was given with the S-parameter matrix in section 2.1.2, but a concrete example can be given via a classic Nonlinear Optics phenomenon. Many nonlinear optical effects can be reinterpreted in the framework of time-varying media, which provides a convenient platform to better understand their most complicated aspects. Consider a reflection coefficient being modulated in phase, with its amplitude kept constant, such that $r(t) = e^{i\omega t}$, shown in Fig.

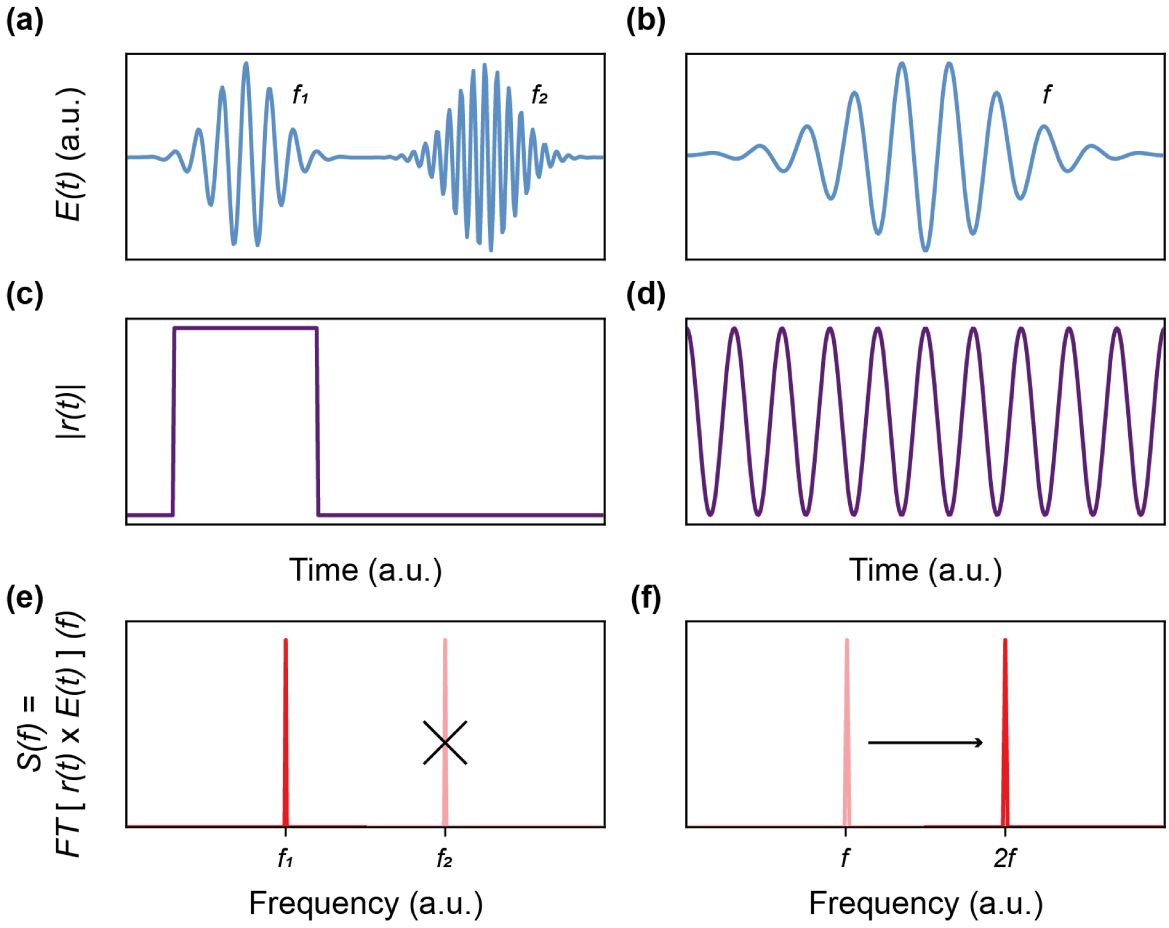

Figure 2.12: Time varying effects with a phenomenological Fourier theory. **(a,b)** Electric field as a function of time in the case of (a) two pulses with different frequencies f_1 and f_2, a simplified case of a highly chirped pulse, and (b) for a pulse with frequency f. **(c,d)** Complex reflection coefficient amplitude $|r(t)|$ as a function of time for (c) a top-hat modulation and (d) a sinusoidal modulation at frequency f. **(e,f)** Resulting modulated spectra: in (e) a frequency is suppressed by the modulation, while in (f) the pulse is upconverted to its second harmonic. Note that the fields shown in (a,b) as well as the spectra shown in (e,f) are illustrative and do not represent physical values.

2.12(d). A Gaussian pulse with carrier frequency f and width σ_f will see all its frequencies shifted by f, generating an outgoing pulse with carrier frequency $2f$ and the same width σ_f, shown in Fig. 2.12(f). This is analogous to SHG, where the reflection coefficient applied as a modulation can be modelled by taking the form of the probe pulse in time in the adiabatic limit where the approximation $E_{2\omega}(t) = E_{\omega}(t)$ can be made [38].

With this phenomenological model, there is no need for a deep modelling of the material and optical properties of a system. Indeed, one could use a combination of theories, for example an ab-initio condensed matter theory giving the change in plasma frequency in ITO, coupled with a transfer matrix method code, to get the complex reflection coefficient $r(t)$, but an informed guess reveals many physics and allows to free ourselves from the limitations imposed by further assumptions in other theories. A particular example of this will be given in chapters 4 and 5

with the rise time of $\rho(t)$.

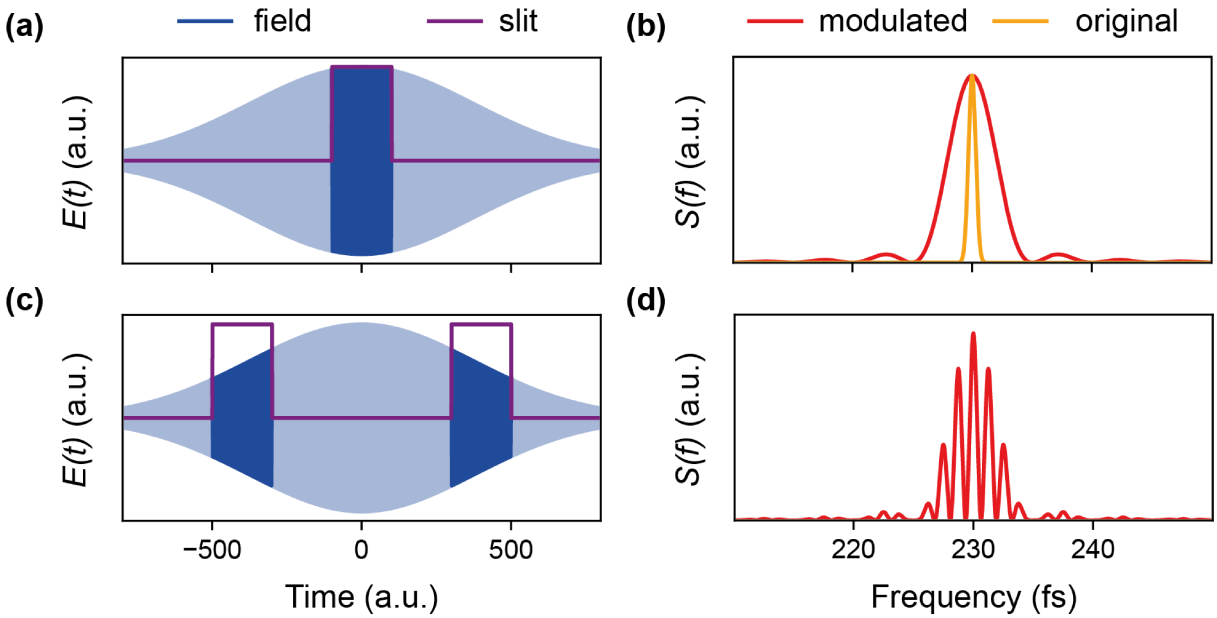

Figure 2.13: Single and double slit diffraction in time with Fourier modelling. **(a)** Effect of a single slit in time (purple line) on the electric field (blue oscillations): only a portion is selected in time (dark blue) while the rest of the pulse is cut out (light blue). **(b)** Resulting spectrum (red line) from Fourier theory, showing diffraction oscillations, compared to the original unmodulated spectrum (orange line). **(c)** Effect of a double slit modulation: the electric field is now separated in two pulses, leading to **(d)** an interference pattern in spectrum.

We can now turn our focus on the two main experiments that will constitute the basis of this thesis. As explained earlier in section 2.2.4, frequency shifting has been thoroughly studied in time-varying media made of TCOs, but little attention has been given to the role of amplitude $\rho(t)$ of the modulation in the generation of frequencies. We propose to demonstrate in this work the concept of time-diffraction, in an all-optical realisation of the single (chapter 4) and double slit experiments (chapter 5). The phenomenological model presented here is particularly well suited to describe the problem, as it is a direct temporal equivalent to the spatial Fourier modelling of Fraunhoffer diffraction. We can then expect the time-modulated signal to have a frequency distribution similar to spatial diffraction patterns observed in conventional optics.

Let us assume a probe field with a carrier frequency of 230 THz and a spectral width of 1 THz (440 fs for a transform-limited Gaussian pulse). If the ON state has a width of a 100 fs and arrives at the same time as the pulse, it will cut it short in time, as shown in Fig. 2.13(a) - thus making it broader in frequency by reciprocity. But the theory also predicts oscillations in the spectrum such as the ones seen in Fig. 2.13(b), which result from diffraction by the temporal slit.

Let us focus now on the double slit experiment. The action of two successive ON states in the aperture function, each with the same shape than shown in and separated by a time T,

will split the probe pulse in two separate pulses as shown in 2.13(c). The interference between the frequencies of these two pulses will generate a diffraction pattern with a sinc-like envelope, shown in 2.13(d), dictated by the shape of the individual slits, and oscillations originating from the separation in time of the slits - just as in Fourier theory.

2.3.2 Condensed matter and electromagnetic theory

The Fourier model presented in the preceding section is remarkable in its simplicity and its ability to give a physical intuition for the complex phenomena happening in time-varying media, though it suffers from not taking dispersion into account. For this purpose, we will use a semi-analytical model such as first presented by Bohn et al. [52]. The model relies on the adiabatic limit, that is when the timescale of the reflection coefficient modulation is significantly larger than the optical cycle of the probe pulse. This allows a series of approximations in solving Maxwell's equations for the magnetic field H.

We first define the complex reflection coefficient as a function of time and frequency $r(t, \omega)$. In frequency space, we have

$$r(\omega_1, \omega_2) = \int_{-\infty}^{+\infty} r(t, \omega_2) e^{i\omega_1 t} \mathrm{d}t \tag{2.14}$$

where ω_1 is a frequency component of the pump induced dynamics and ω_2 refers to the probe signal frequency. From the adiabatic approximation (see [52] for more details) the reflected spectrum then is

$$H_r(t) = \int_{-\infty}^{+\infty} r(t, \omega') a(\omega') e^{-i\omega' t} \frac{\mathrm{d}\omega'}{2\pi} \tag{2.15}$$

where $a(\omega')$ is the original, unmodulated probe spectrum. Then, the reflected frequency spectrum is simply the Fourier transform of the reflected field, that is

$$H_r(\omega) = \int_{-\infty}^{+\infty} H_r(t) e^{i\omega t} \mathrm{d}t \tag{2.16}$$

$$= \int_{-\infty}^{+\infty} \int_{-\infty}^{+\infty} a(\omega') r(t, \omega') e^{-\omega' t} e^{i\omega t} \frac{\mathrm{d}\omega'}{2\pi} \mathrm{d}t \tag{2.17}$$

Equation 2.17 shows we can compute the modulated spectrum in the adiabatic limit if we know the reflectivity of the medium as a function of time and frequency, and the original probe spectrum. While the original probe spectrum can easily be fitted and determined from an

experimental measurement, $r(t, \omega')$ has to be determined either via an informed guess or other means. The adiabatic limit puts a constraint on the input reflection coefficient, as opposed to the Fourier theory: the rise or decay time of the modulation has to be sufficiently slow compared to the probe optical cycle. In other words, if the Fourier theory works for modulations at the single optical oscillation timescale (∼4 fs), the semi-analytical model is better suited if the modulation timescale is comparable to that of the pump pulse (∼220 fs).

To build up on the semi-analytical model, we use two further theoretical tools: a well informed shifted Drude model, and the analytical TMM.

The shifted Drude model relies on our knowledge of ITO modulation gained in section 2.2. As we will experimentally rely on intraband pumping, we know the plasma frequency will redshift following absorption of light by the medium. This absorption will follow the intensity envelope of the pump pulse $I(t)$ (a Gaussian with FWHM 225 fs), but will also be determined by the medium's intrinsic response function $\xi(t)$. We then write

$$\delta\omega_p(t) = \alpha I(t) * \xi(t) \tag{2.18}$$

where α is a negative coefficient related to the nonlinear Kerr effect. We can then express the plasma frequency as

$$\omega_p(t) = (1 + \delta\omega_p(t))\, \omega_p^{(0)} \tag{2.19}$$

where $w_p^{(0)}$ is the original plasma frequency of the medium. α and $I(t)$ can be measured experimentally, which leaves $\xi(t)$ as a free variable. As the measured change in reflectivity follows the change in plasma frequency, we can try and use a measured $R(t) = |r|^2$ to find $\xi(t)$, but we hit here another barrier of our adiabatic model. Assuming the timescale of 225 fs for $I(t)$, we cannot resolve any dynamics in the material response function shorter than this due to the convolution in equation 2.18. In any case we infer a function $\omega_p(t)$ that we will then plug into the TMM to deduce a complex reflection coefficient $r(t, \omega)$. The following formalism is as presented in [84].

Let us consider a medium as shown in Fig. 2.14(a), with refractive index n and thickness d. Using Maxwell's equations, we can relate the electric and magnetic fields on either side of the layer using a transfer matrix M such as

$$\begin{bmatrix} E_1 \\ B_1 \end{bmatrix} = M \begin{bmatrix} E_2 \\ B_2 \end{bmatrix} \tag{2.20}$$

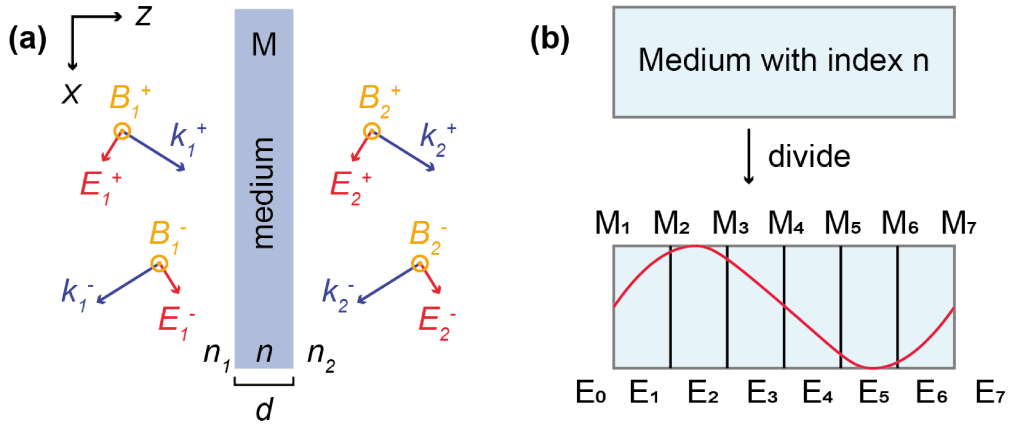

Figure 2.14: TMM theory diagram. **(a)** Inner working of the TMM code: the waves propagating in positive and negative z directions on either side of an interface can be related by a transfer matrix M. **(b)** Extracting a field intensity distribution with TMM: any layer or medium can be divided in sub layers, each with their own interfaces where the electric field can be computed.

where E_1 and B_1 respectively represent the total electric and magnetic fields on one side of the layer, and E_2 and B_2 the total fields on the other side. The total fields are expressed as the sum of the two counter-propagating waves, for example $E_1 = E_1^+ + E_1^-$. Assuming the field has a vacuum wavevector k_0, the transfer matrix can then be expressed as

$$M = \begin{bmatrix} \cos(\delta) & i\frac{\sin(\delta)}{\nu} \\ i\nu\sin(\delta) & \cos(\delta) \end{bmatrix} \tag{2.21}$$

where $\delta = k_0 n d \cos(\theta)$, θ the angle of the wavevector with the normal of the medium's interfaces and $\nu = n/(c\cos(\theta))$ if light is p-polarised/transverse magnetic or $\nu = n(\cos(\theta)$ if light is s-polarised/transverse electric. The factor of c on the off-diagonal elements of the matrix originatie from the conversion between electric and magnetic fields. The transfer matrix of a multilayered structure being the product of the transfer matrices of each individual layer i.e. $M = \prod M_i$, we can compute the transmission and reflection coefficients of our unstructured samples.

By setting the amplitudes $E_1^+ = 1$, $E_1^- = r$, $E_2^+ = t$ and $E_2^=0$, and using $E_i = E_i^+ + E_i^-$ we have

$$\begin{bmatrix} 1+r \\ \nu_1(1-r) \end{bmatrix} = \begin{bmatrix} M_{11} & M_{12} \\ M_{21} & M_{22} \end{bmatrix} \begin{bmatrix} t \\ \nu_2 t \end{bmatrix} \tag{2.22}$$

where ν_1 and ν_2 are the equivalents of ν in media 1 and 2, before and after the layer. Solving these equations gives the complex reflection r and transmission t coefficients of any layered structure. Plugging in $\omega_p(t)$ from our shifted Drude model, we can now obtain a reflection

coefficient $r(t)$ that we can insert into our adiabatic semi-analytical theory. For reference we will write down below the analytical solutions to the TMM:

$$\begin{cases} r = \frac{(M_{11}+M_{12}\nu_2)\nu_1-(M_{21}+M_{22}\nu_2)}{(M_{11}+M_{12}\nu_2)\nu_1+(M_{21}+M_{22}\nu_2)} \\ t = \frac{2\nu_1}{(M_{11}+M_{12}\nu_2)\nu_1+M_{21}+M_{22}\nu_2} \end{cases} \tag{2.23}$$

and the reflectivity can then be expressed as $R = |r|^2$ and transmittivity as $T = \nu_2|t|^2/\nu_1$. This allows us to predict the linear properties of the sample, mainly its reflectivity and complex reflection coefficient, but also the electric field amplitude in a layer j. Note that a layer can be divided in a series of sub-layers with the same index, as depicted in Fig. 2.14(b), so as to increase the spatial resolution of the electric field in the system (the transfer matrix then only corresponds to a propagation by the thickness d of the sub-layer). In a multilayered structure, the field in layer j is given by

$$E_j = (1+r)m^j_{22} - (1-r)m^j_{12}\nu_1 = tm^j_{11} + tm^j_{12}\nu_2 \tag{2.24}$$

where m^j_{ik} are the coefficients of the transfer matrix of the j$^{\text{th}}$ layer. This allows us to accurately predict the field distribution inside a multilayered material, and thus have information on the coupling of light to a nonlinear medium such as ITO giving us precious information on the efficiency of the nonlinear modulation. Another useful application of TMM will be presented in chapter 6, when it will be used in conjunction with nonlinear scattering theory to extract a value for the third order nonlinear susceptibility of ITO and GaP.

Chapter 3

Making a slit in time

3.1 Introduction

When studying spatial diffraction, the making of a slit is a trivial concern in the context of modern science. In contrast, the making of a temporal slit is a complex task that requires careful design and characterisation as well as advanced laboratory equipment. In this chapter, we will study an ITO/Au bilayer, consisting of 40 nm of ITO followed by a gold reflective layer, under optical pumping in the NIR, and look into how it can create an aperture function suitable for time diffraction at optical frequencies. We wish to exploit the optical excitation of intraband electronic transition mechanism presented in section 2.2, to induce a redshift of the plasma frequency in the ITO thin film which will in turn result in a change in permittivity and thus reflectivity.

In order for the change in reflectivity/aperture function to be fast enough to exhibit strong diffraction, an ultrafast pump pulse is used to induce all-optical modulation. Consider a 200 fs FWHM pulse as shown in Fig. 3.1(a). As it is coupled into the medium, the field intensity in the medium also take the form of a Gaussian as a function of time - a first approximation, as we will see later in section 3.3 the pump pulse can undergo self-modulation. As described previously in section 2.2.3, intraband absorption within the medium will lead to a redshift of the plasma frequency following the pump intensity profile in time. An extra component that must be integrated in our understanding of all-optical pumping is the medium's response function $\Gamma(t)$, which describes how and when the material responds to the optical excitation. $\Gamma(t)$ can be modelled as an impulse with finite, exponential rise and decay times τ_{rise} and τ_{decay}, shown here in Fig. 3.1(b). The plasma frequency will then be a convolution of the driving pump pulse intensity and the response function (Fig. 3.1(c)), which can lead to an asymmetry in the temporal evolution of the plasma frequency. In the limit of an instantaneous response, $\tau_{rise} \to 0$ / $\tau_{decay} \to 0$ and the response function becomes a Dirac delta function, meaning the plasma frequency has the same Gaussian temporal profile than the driving pump pulse.

As the material response time and the pulse dynamics have already been taken into account, no further dynamics are introduced in the translation from plasma frequency shift to change in reflectivity: the curve in Fig. 3.1(d) has the same dynamics than in Fig. 3.1(c) - and a fast

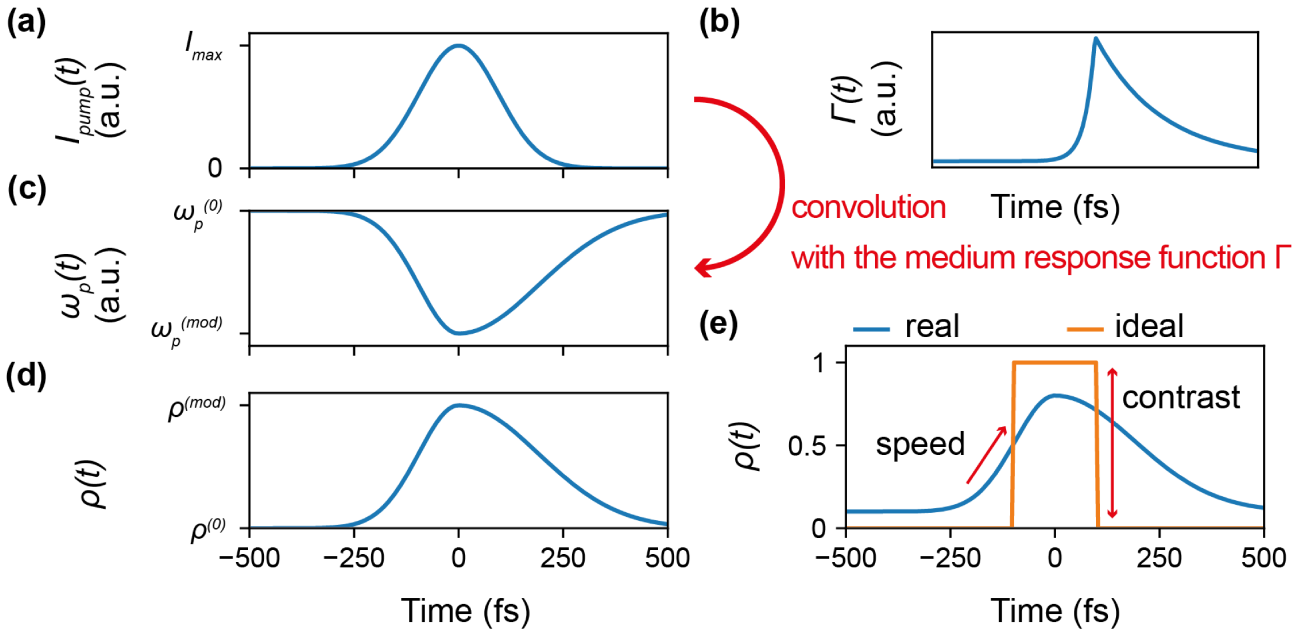

Figure 3.1: Diagram of the experimental realisation of a single slit in time. **(a)** An illuminating pump pulse creates an intensity profile in the medium in time, here a Gaussian. **(b)** The medium has an intrinsic response function Γ that allocates a response time to the electrons receiving energy from the driving pump pulse, which can create a temporal asymmetry in **(c)** the plasma frequency of the medium as a function of time. This change in plasma frequency corresponds to a change in **(d)** the Fresnel coefficient in time, here shown as real i.e. $r = |r| = \rho$. **(e)** The material linear properties, response time and driving pump pulse must be chosen to bring the resulting temporal change in reflectivity as close as possible to an ideal slit, that is with short rise and decay time as well as high contrast.

variation of the system's complex Fresnel coefficient is obtained. The figures of merit for an efficient slit for time diffraction can be inferred from comparing an ideal slit with a practical one in Fig. 3.1(e): (1) a high contrast is desirable for straightforward reasons (as the contrast gets lower the slit diffracts less) and (2) high switching speeds are essential for the wave to be able to experience modulation from the slit. This means the changes must be non-negligible within the timescale of an optical cycle.

These two criteria guide our design of the bilayer and our choice of material for time-diffraction. In particular, the role of the medium response function and the pump dynamics become essential in the light of criterion (2). Criterion (1) will be more easily satisfied by taking advantage of the dispersion of the sample and using the right experimental conditions. In this chapter, we will look into the linear and nonlinear properties of the bilayer and follow by a characterisation of a single slit in section 3.3 to gain a better understanding of our system. The physics shown at play here will be the basic building block for the experiments described in chapters 4, 5 and 6, and can be applied to other ITO thin film based systems, notably the 310 nm layer which will equally be presented in said chapters.

3.2 From linear to nonlinear properties of Indium Tin Oxide

3.2.1 The Berreman resonance in an Indium Tin Oxide/Au bilayer

To achieve a high contrast in reflectivity, we exploit the resonant behavior of the ITO thin films mentioned in section 2.2. Berreman resonances can be accessed via free-space illumination under the right illumination conditions. From Vassant et al.'s work [55], we know that Berreman resonances get stronger - that is exhibit a larger dip in reflection - when the thin film becomes narrower. By modulating the plasma frequency, a probe signal can be shifted out of the Berreman resonance and observe a high contrast in reflected intensity. To further enhance the Berreman resonance strength, a gold back mirror is added in a similar geometry as [72]. This can be understood in the light of classical optics (though not applicable for subwavelength systems): by cancelling transmission, and the Berreman achieving a perfect suppression of reflection for p-polarised light, the bilayer is on paper a perfect absorber in the Berreman condition.

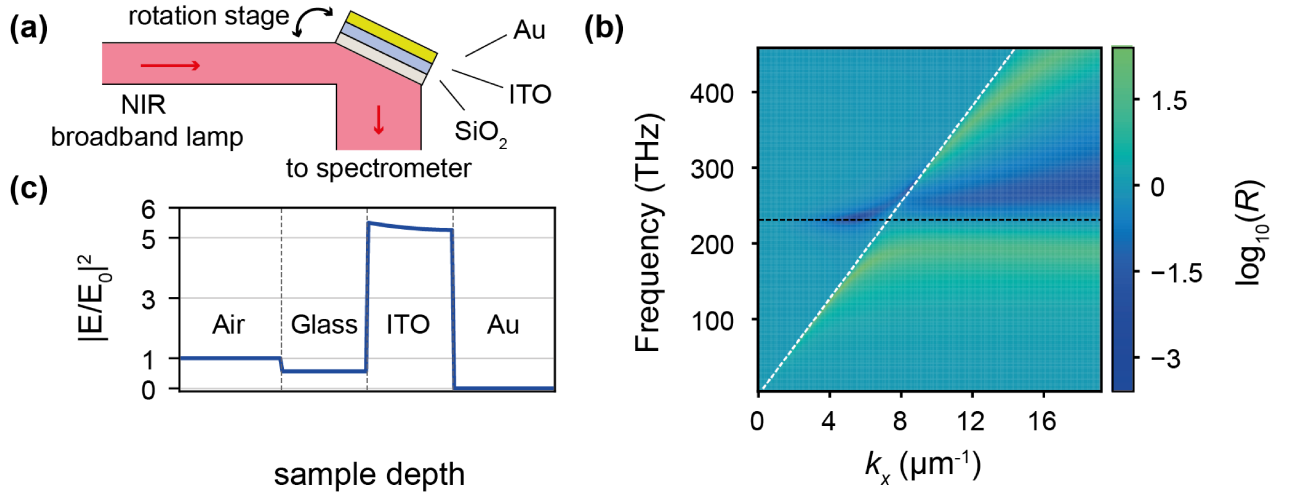

Figure 3.2: Linear properties of the ITO/Au bilayer. **(a)** The sample consists of three successive layers of 1 mm SiO_2, 40 nm ITO and 200 nm Au. For linear characterisation, a broadband NIR lamp is directed at the sample and collected in reflection, and the signal is compared to that reflected by an Ag mirror. **(b)** Simulated dispersion diagram of the bilayer: the Berreman resonance is visible in dark blue above the light line (white dashed line), close to the ENZ frequency (black dashed line). **(c)** Simulated field distribution within the sample using TMM for an angle of 65°. A strong field enhancement is visible within the ITO layer when compared to the other layers, showing a good coupling to the medium. Panels (b) and (c) reproduced from [79].

Due to fabrication constraints, the gold has to be deposited on top of the ITO, and the sample illuminated through the SiO_2 substrate. The sample used in this chapter, as well as

chapters 4 and 5 is composed of a 1 mm thick SiO_2 substrate, on which lies 40 nm of ITO with 200 nm Au on top, as shown in Fig. 3.2(a). The Au only acts as a back reflector for performance enhancement and does not play a role in the time-varying physics.

By solving for the boundary conditions in the wave equation, one can solve for the dispersion of the sample. As shown in Fig. 3.2(b), a strong decrease in reflection, and hence a strong increase in absorption as transmission is null, is expected at the Berreman condition. The Berreman resonance is slightly above the ENZ frequency (230 THz against 227 THz) and spectrally broad, allowing for a range of efficient illumination angles. As can be seen from TMM simulations in Fig. 3.2(c), the electric field within the ITO layer is strongly enhanced when illuminating at a 65° incidence angle. This means the coupling from free space to the medium is efficient, which will be useful both for pumping and modulation. For pumping, a higher field intensity and absorption means more energy will be transferred to the electrons in the conduction band, leading to a larger modulation of the material properties. For the probe, starting at the bottom of the Berreman resonance (low reflectivity) and being driven out by the modulation (high reflectivity) will lead to high contrast in the slit. We thus aim to bring both pump and probe as close as possible to the optimal conditions of the Berreman resonance.

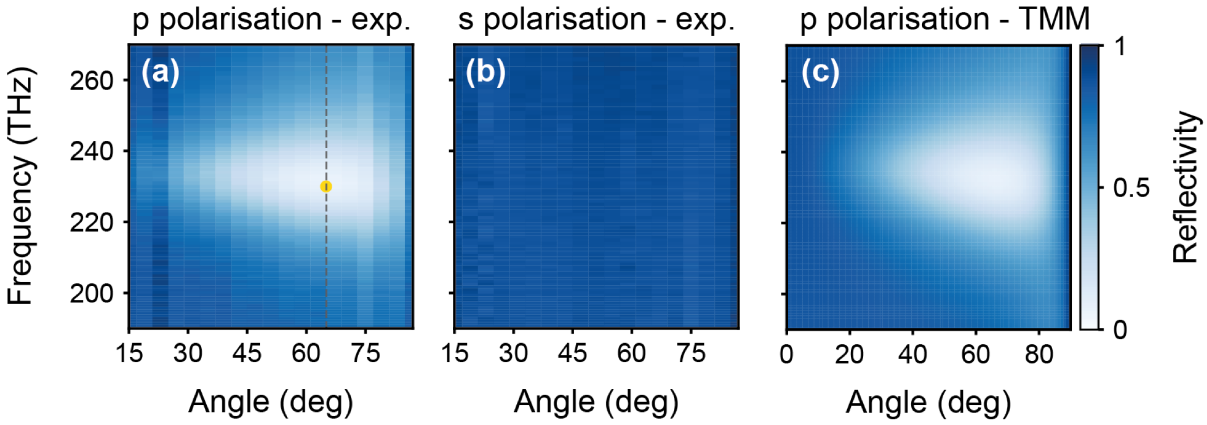

Figure 3.3: Linear properties of the Berreman resonance. **(a,b)** Measured reflectivity spectra as a function of incidence angle for (a) p-polarised and (b) s-polarised light. **(c)** Predicted reflectivity of the bilayer from TMM simulations for p-polarised light. Panels (a) and (c) reproduced from [79].

We measure the reflectivity of the sample using a broadband Tungsten-Halogen lamp illuminating the sample, the reflected signal being collected in reflection. This signal is compared to that collected when using a silver mirror that has a flat reflectivity of 98-99% in the spectral range of interest to give the reflectivity of the sample. For p-polarised light, the reflectivity spectrum of the bilayer is given for various angles in Fig. 3.3(a). One can observe the typical, teardrop-shaped reflectivity dip of the Berreman resonance, getting deeper (lower reflectivity)

and broader as the incidence angle gets closer to the Brewster angle. In the context of making a slit, we wish to place ourselves in the optimal experimental conditions, met at the light orange point on the panel. Here, the reflectivity is at its minimum, leading to a higher contrast, and the resonance is spectrally broad, creating an interesting trade-off between the Berreman resonance and the probe pulse width that will be discussed in chapter 4.

In comparison, the bilayer exhibits no resonance for s-polarised light, the reflectivity shown in Fig. 3.3(b) being angle independent as expected. The data shown in Fig. 3.3(a) and (b) is used to fine-tune the already known ellipsometric values of permittivity ϵ_∞, ω_p and γ in our Drude model, and the TMM prediction of reflectivity shown in Fig. 3.3(c) is in excellent agreement with the experimental result.

Having designed and modelled a bilayer with reliable linear properties, and verified the consistency between experiment and theory, we can now turn our attention to the nonlinear properties of the sample and the experimental methods we will put in place to measure them.

3.2.2 Modulation of the Berreman resonance

A first impression of the Berreman resonance's time-varying physics can be given using the Drude model presented in section 2.3. In a first step, we will ignore temporal dynamics and look into the modulation of ITO for a given intensity impinging on the medium. Taking $\alpha = -1.52 \times 10^{-4}$ cm^2/GJ in equation 2.18, we predict the reflectivity spectrum for increasing pump intensity in the bilayer in Fig. 3.4(a) using TMM. One can observe the Berreman mode being redshifted to lower frequencies, while reflection at the unmodulated minimum of the Berreman mode (230 THz) jumps from near-zero to near-unity. Looking at the reflectivity values at 230 THz in Fig. 3.4(b) as a function of intensity, we can see that though the plasma frequency is linearly dependent on intensity, the change in reflectivity is not, due to the shape of the Berreman resonance around its minimum. Note that the base reflectivity is low at 7% - of which 4% can be attributed to the reflection at the air/glass interface. The full modulation of the reflectivity is thus extremely large, above 1000% for pump intensities above 100 GW/cm^2.

Two important details must be noted from Fig. 3.4(c) and (d), where the complex reflection coefficient $r = \rho e^{i\phi}$ is plotted against frequency for increasing intensities (blue to red, low to high) in amplitude (c) and phase (d). First, from Fig. 3.4(c), our model assumes a shift only in ω_p and neglects the modulation of γ. This approximation was done to simplify the model and reduce the number of fitting parameters, and as non degenerate measurements would be needed to characterise the change in γ. Though the Berreman resonance gets shallower at a low pace

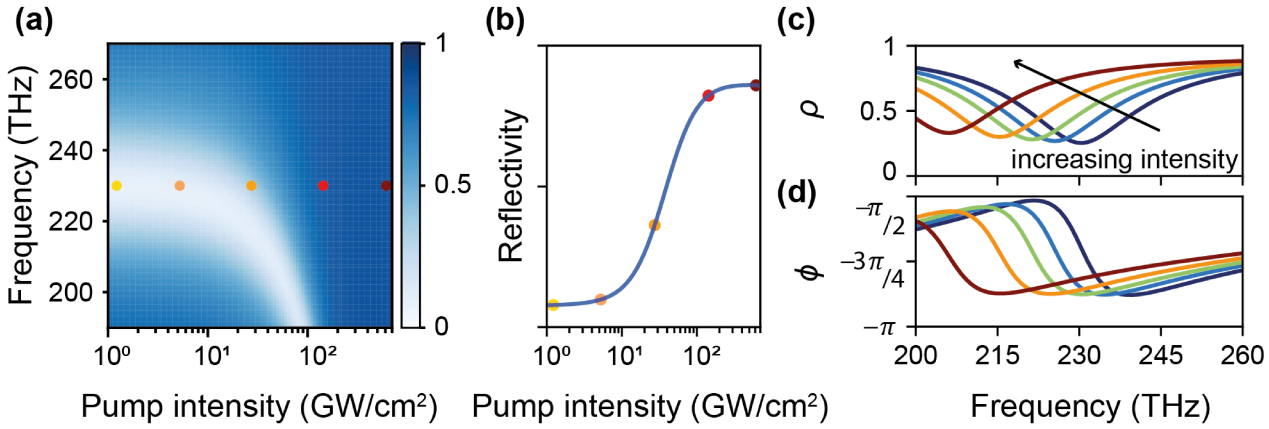

Figure 3.4: Modelling of the modulated Berreman resonance. **(a)** Simulated reflectivity of the bilayer against frequency and illuminating pump intensity. The dots indicate the corresponding locations on **(b)** reflectivity against intensity at 230 THz. **(c,d)** Complex reflection coefficient (c) amplitude and (d) phase against frequency for low to high intensities (dark blue to dark red). Panels (a) and (b) reproduced from [79].

when shifting the plasma frequency only, a change in losses is expected to affect the measured modulation. As will be seen in chapter 4, the change in γ is not essential to the modelling of the bilayer, but gains importance in thicker ITO samples with no gold back reflector.

Secondly, one can observe in Fig. 3.4(d) how the probe can cross the resonance in phase if its carrier frequency is equal or above to 230 THz. Resonances are typically distinguished by an important phase change between frequencies, which will translate for a time-varying medium as a frequency shift in the reflected probe spectrum. Hence, the single slit in the complex reflection coefficient of the bilayer exhibits both changes in phase and amplitude. Experimental measurements will determine which mechanisms are dominant in the spectral modulation.

Note the importance of the role of the asymmetry of the temporal modulation: the rise time of the reflection coefficient change is expected to be faster than its decay [53], meaning the increase in reflectivity and decrease in phase will have a sharper slope than their respective decrease and increase on the recovery. This asymmetry, as explained in section 2.1.2, will favour certain spectral shifts and broadening over others during the modulation.

3.2.3 Experimental setup and methods

All measurements presented in this work are performed in a pump-probe setup such as the one depicted in Fig. 3.5(a). A Pharos Light Conversion laser generates pulses at 291 THz (1030 nm wavelength) that are sent to an Orpheus Optical Parametric Amplifier. Outgoing pulses can be tuned between 150 (2 µm) and 1500 THz (200 nm). In the frequency range of interest

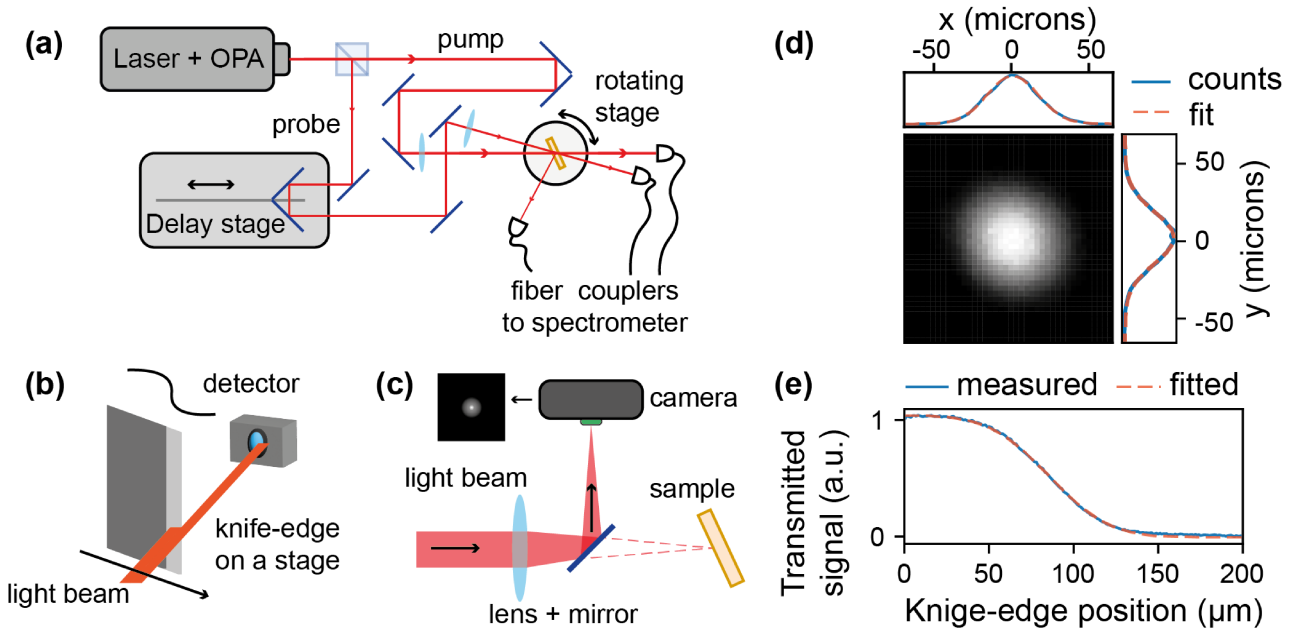

Figure 3.5: Pump probe setup and beam size measurement. **(a)** Simplified diagram of the pump probe measurement setup. Optical elements such as optical filters or neutral density filters are not represented for clarity. **(b)** Diagram of a knife-edge measurement: an object with a straight, sharp edge (here a razor blade) is moved in the plane normal to the beam's propagation direction. The change in transmitted signal is recorded and used to extract the beam size at the position of the knife-edge. The knife-edge's position can be changed along the beam propagation direction to find the point of focus. **(c)** Diagram of the alternative beam size measurement setup using a camera: a mirror is used to redirect the beam while a camera is placed at the focus. **(d)** Example of a measured beam at the camera: the beam is a 2D Gaussian and the counts in the x and y direction (continuous blue line) are fitted (dashed orange line) to extract a beam waist. **(e)** Example of a knife-edge measurement: the measured error function (continuous blue line) is fitted (dashed orange line) to extract a beam size. The two measurement techniques give matching results.

(around 230 THz), the manufacturer specifies a pulse FWHM of 220 fs. We later measure this pulse width to be of 225 ± 5 fs (see section 3.3.4). The laser pulse is then separated using a beam splitter into a pump and probe pulse. The relative arrival time between the two pulses is controlled via a delay stage. The power of the beams can be tuned using neutral density filters. The two beams are then focused and intersected at the sample, and the transmitted and reflected signals are sent to spectrometers through a collection system integrating fiber couplers. Depending on availability, a variety of spectrometers were used for measurement: lower sensitivity and resolution Oceanview spectrometers (flame and flameNIR for visible and NIR light respectively), or a more advanced Teledyne HRS spectrometer with a PIXIS (visible) or NIRvana (NIR) camera. The sample and reflection detection sit on rotating stages, allowing for changes in the illumination angle. The illumination angle will here be defined as the probe's incidence angle from the normal. The sample's position can additionally be controlled using stages in all three dimensions, allowing to change its position relative to the focus of the two

beams, as well as the illumination regions.

The repetition rate of the laser can be varied between 100 Hz and 100 kHz. For our samples, optical damage originates mainly from the build-up of heat within their volume due to absorption. By decreasing the repetition rate, one can reduce this build-up and lower the damage threshold at the expense of signal. As high intensities in the NIR are easily achieved, most measurements presented in this thesis were done for repetition rates of 100 Hz or 1 kHz. Note that higher volumes also provide higher damage thresholds as there is more space for heat to dissipate in, while higher surface areas (thinner samples or nanostructures) bring down the damage threshold as air is a poor thermal conductor.

Particularly, the linear stages allow us to perform knife-edge measurements, a well known technique to measure a beam's size and focal position. By moving a razor blade across the beam and measuring the transmitted light as shown in Fig. 3.5(b), one can fit the following function to the measured signal [85, 86]:

$$P(x) = \frac{1}{2}P_0\left(1 + \mathrm{erf}\left(\frac{x_0 - x}{w}\right)\right) \tag{3.1}$$

where P is the measured power, P_0 the illuminating power, x the coordinate along the knife-edge's movement, x_0 the corresponding point where the knife edge cuts the beam and w the beam waist. This allows us to determine the beam waist at the focus. This is crucial information as measured modulation of the sample is dependent on driving pump intensity, which depends quadratically on the beam waist size. It is therefore important that the later is measured with satisfying accuracy. Yet, knife-edge measurements are time-consuming, which pushes us to use an alternative technique to evaluate the beam size.

One can do direct imaging of the beam at the focus by placing a mirror and a camera as a alternative path to the sample, after the focusing lens, as shown in Fig. 3.5(c). The beam can then be fitted in the 2D plane of the camera and a beam waist extracted (shown in Fig. 3.5(d)). An important factor to take into account is the role of 2-photon absorption against linear absorption: the cameras used were Zelux CMOS cameras meant for visible detection. Detection is linear with intensity up to 1200 nm, but signal becomes quadratic beyond this wavelength due to 2-photon absorption and a factor of $\sqrt{2}$ must be applied to the beam size. Beam sizes extracted using the camera have been compared to those fitted using the knife-edge technique (example shown in Fig. 3.5(e)) and have yielded good agreement, justifying the use of the direct focal imaging technique as a beam size measurement technique.

As the experimental apparatus measures an average power $P_{mathrmavg}$, it is then necessary

to compute the pulse peak power:

$$P_{\text{peak}} = \frac{P_{\text{avg}}}{\tau \times f_{\text{rep}}} \tag{3.2}$$

where τ is the pulse width and f_{rep} the repetition rate of the laser. Once the beam waist and the illuminating peak power are known, the pulse peak intensity can be expressed as

$$I = \frac{2P_{\text{peak}}}{\pi w^2} \tag{3.3}$$

Note that the factor of 2 is important but often neglected in literature. It arises from the spatial integration of the Gaussian beam profile $I(x, y, z)$ over the (x, y) plane at $z = 0$ where the beam waist is minimal. Throughout this work, discussions and values in intensity will be implied as that of illuminating intensity and not field intensity within the medium, as the later depends on the conditions of illumination (frequency, angle) and the sample geometry. To control the illuminating intensity, the first approach is to use variable neutral density filters, with the maximum achievable power being limited by the laser power and losses of the optical path. Control over the beam size, thanks to intensity's quadratic dependence on the beam waist, can allow us to easily multiply or divide intensity by factors of 2 to 10. The size of the beam can be tuned by changing the focal length of the focusing lens, or changing the size or divergence of the beam before said lens. In the present and following chapter, smaller beam sizes have been used to explore a more dynamic range of intensities up to 700 GW/cm^2. As we will show, the use of the full range is not necessary and intensities of 'only' 100 to 200 GW/cm^2 are needed, allowing us to use larger pump and probe beams in chapters 5 and 6. Using a larger beam gives the benefit of a more stable setup, as the beams are less susceptible to the instabilities in the optical path.

Having laid out the design foundations of the time-varying system and established the experimental method, we can now move on to the measurement and characterisation of the modulation in the ITO bilayer.

3.3 Ultrafast modulation of Indium Tin Oxide

To begin with, we will look at the information that can be found in the spectrally integrated probe as a function of pump-probe delay. The ITO/Au bilayer is modulated by a single pump pulse, a Gaussian in time centered at $t = 0$ on the sample. A probe arrives with a delay τ with regards to the pump and observes the change in permittivity in the medium. We thus define

negative delay as the probe arriving at the sample before the pump, and positive delay as the pump arriving before the probe. Pump and probe are degenerate in frequency. This section first fully characterises the bilayer's reflectivity changes, and then moves on to determining the dependence of the modulation on the probe pulse properties.

3.3.1 Temporal reflectivity change

First, modulation is measured for various pump-probe carrier frequencies, intensities and illumination angles, with the pump having a lower incidence angle 10 degrees below that of the probe. The probe intensity is kept low to avoid any self modulation (see section 3.3.3). Shown in Fig. 3.6(a) are scans of the modulation, showing reflectivity as a function of delay for a probe pulse at 230 THz (2.8 THz bandwidth, far below the bandwidth of the Berreman resonance) and 65 degrees angle for multiple pump intensities. Very notably, the reflectivity can go from 0.07 to 0.66 at the highest intensity of 708 GW/cm^2, within a short timescale that cannot be resolved but whose upper limit is the pulse's intensity rise time $\sim$ 110 fs. This modulation, of order $\Delta R/R \sim 1000\%$, and its associated timescale make the ideal condition for the realisation of a time-slit.

One can notice the asymmetric shape of the modulation, with a decay longer than the pulses' duration of 225 fs. This is due to the relaxation mechanisms in intraband pumping described in section 2.2. At low intensities, the decay time is of 360 fs, in agreement with literature [53], and as the pump intensity reach higher levels the decay time increases to about 600 to 800 fs. It is clear from Fig. 3.6(a) that the modulation behaviour at high intensities become highly nonlinear, with lesser gains in reflectivity being done between 156 GW/cm^2 and 708 GW/cm^2 and the increase in relaxation time.

To demonstrate the increase in modulated reflectivity contrast at the Berreman resonant frequency, a map showing the reflectivity as a function of delay for multiple carrier frequencies for an intensity of 40 GW/cm^2 is shown in Fig. 3.6(b). An increase in reflectivity is visible for frequencies above 230 THz, but decreases can also be achieved by using frequencies below the Berreman resonance, notably in the 215 to 220 THz range. We find here a sign that the rise time dynamics are significantly below the probe's width of 225 fs. We should see a decrease in reflectivity at slightly negative delays for frequencies below 230 THz from crossing the Berreman resonance (down then up) in Fig. 3.6(c), but this is not the case for frequencies closer to 230 THz. Furthermore, for these frequencies above the Berreman resonant frequency, after increasing the reflectivity doesn't go back as far down than the minimum of 7% before

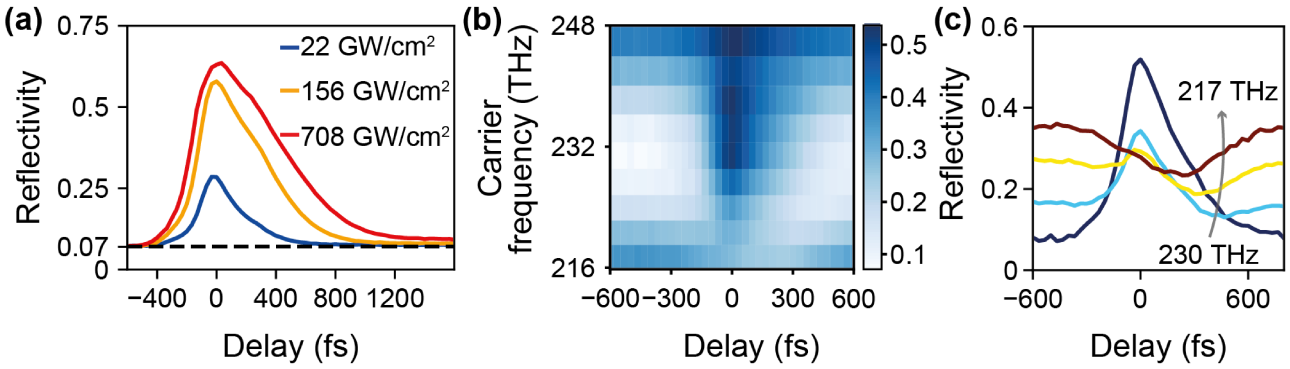

Figure 3.6: Reflectivity as a function of delay in the bilayer. **(a)** Reflectivity as a function of delay for three pump intensities for a carrier frequency of 230 THz and a 65 degree incidence angle . The black dotted line shows the base, unmodulated reflectivity. **(b)** Reflectivity as a function of delay and probe carrier frequency for an angle of 65 degrees and a pump intensity of 40 GW/cm^2. **(c)** Corresponding signal as a function of delay for four carrier frequencies above the Berreman resonant frequencies, at 217, 221, 224 and 230 THz (from dark blue to dark red). Panel (a) reproduced from [79].

recovering, which shows that the Berreman mode gets shallower. This means that not only the material dynamics are below the temporal resolution of the scan, which is here limited by the probe pulse width, but also that there is an extra variable to be accounted for in modelling. Unfortunately, an additional physical value needs to be measured in order to accurately determine the change in γ, such as transmission, not available with this sample, or phase, not measurable within this pump-probe setup.

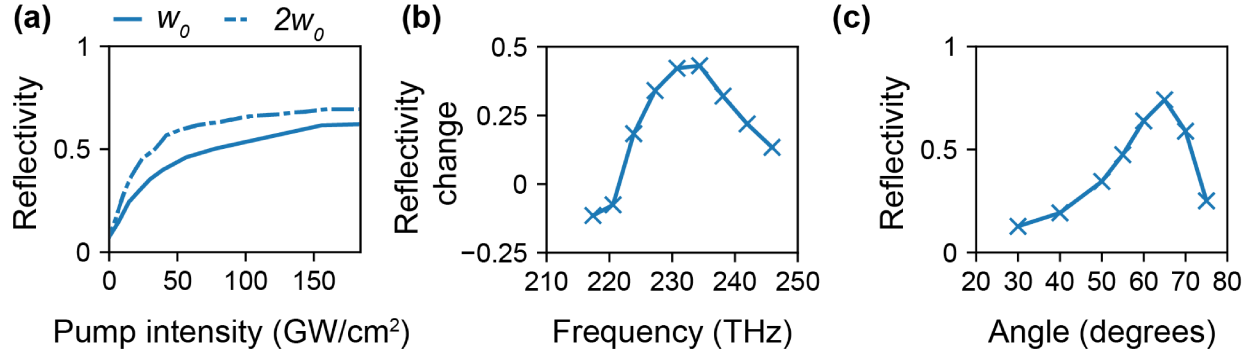

Figure 3.7: Intensity, frequency and angular response of the bilayer under optical pumping. **(a)** Reflectivity as a function of pump intensity for different beam sizes, for an incidence angle of 65 degrees and a carrier frequency of 230 THz. **(b)** Reflectivity change $\Delta R = R - R_0$ (where R_0 is the unmodulated reflectivity) as a function of frequency, at an angle of 65 degrees and intensity at 40 GW/cm^2. **(c)** Reflectivity as a function of incidence angle, for a frequency of 230 THz and an intensity of 132 GW/cm^2. Reproduced from [79].

To further confirm our intuitions from the previous section 3.2, we fully characterise the modulation within the bilayer. The pump intensity dependence of the reflectivity modulation (i.e. at the max reflectivity change at a given delay) is shown in Fig. 3.7(a), for two pump/probe beam sizes (30/15 against 50/30 microns). The overall and relative beam sizes play a role in

the intensity-dependent behaviour of the modulation in a pump probe experiment. Though the role of the pump pulse width in time with regards to the probe has been discussed by Liu et al. [66], the role of beam sizes remains unexplored. The different saturation level between the two beam sizes could be attributed to a stronger carrier diffusion effect for smaller beam sizes, reducing the efficiency of the modulation and pushing saturation towards higher intensities. The modulation appears to saturate at a constant level for pump intensities above 100 GW/cm^2. We attribute the origin of the saturation to the flat dispersion of reflectivity outside of the Berreman resonance. A saturation of the electron dynamics and permittivity within the medium under high intensities was considered but set aside as recent work indicates this is not the case [80]. Regardless of the physical origin of the modulation, it is useful to differentiate the unsaturated and saturated regimes as they show different dynamics (as shown in Fig. 3.6(a)) which will become important when considering spectral modulation in chapter 4.

Panels (b) and (c) in Fig. 3.7 confirm that the minimum of the Berreman resonance is the best configuration to achieve high contrasts in reflectivity under modulation. Results show that the frequency of 230 THz and angle of 65 degrees are indeed the best configuration to observe a large change in reflectivity of the sample.

3.3.2 Comparison with the semi-analytical model

So far, results have met our expectations, but we yet need to test our capacity to model and predict the time-varying effects in the bilayer. We will first look into the capacities of the semi-analytical, adiabatic model presented in section 2.3, the comparison between simulated results and experiment being shown in Fig. 3.8(a). The experimental results are the same as shown in Fig. 3.6(a). The agreement between experiment and theory is remarkable at low pump intensity, but behaviours diverge when intensity is increased. One difference lies in the decay time, this is not surprising as it is kept constant in the model (τ_{decay} = 210 fs 1/e time of the response function as described in section 2.3 and the introduction of chapter 3) while it visibly increases experimentally. This is due to the dependence of the electron heat capacity on temperature, and was predicted and measured by Del Fatti et al. in Silver [87] and Alam et al. in ITO [53].

The second divergence between the adiabatic model and experiment comes in the rise and plateau of the modulation. The difference appears in the saturation regime, with the curve at 708 GW/cm^2 being ostensibly different in slope and amplitude. Our model assumes no

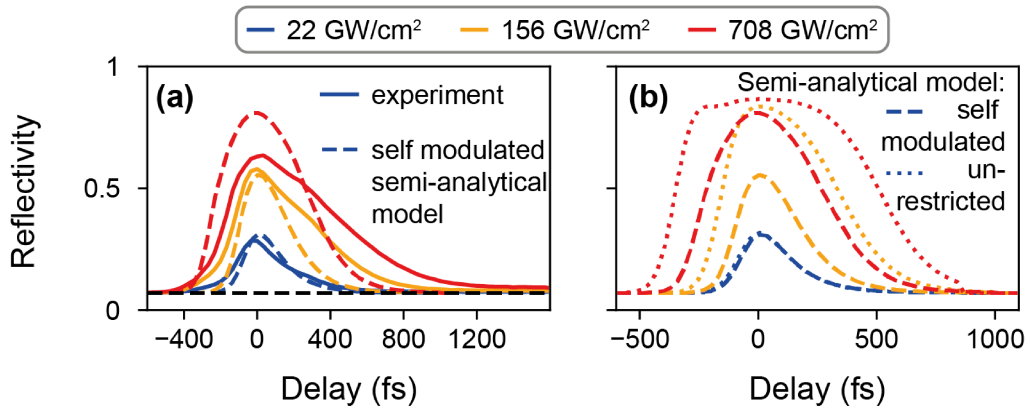

Figure 3.8: Semi-analytical modelling of the modulation in the bilayer. **(a)** Reflectivity against delay for various pump intensities, for a frequency of 230 THz and incidence angle of 65 degrees. Theory is shown with dotted lines while experiment is represented with a continuous line. **(b)** Comparison between a model including pump self-modulation (dashed line) and one with unconstrained pump intensity (dotted line). Panel (a) reproduced from [79].

saturation behaviour in the electron dynamics (in equation 2.18 behaviour is linear with intensity, here with $\alpha = -1.52 \times 10^{-4}$ cm^2/GJ fitting best the initial slope in Fig. 3.7(a)), and a convergence on the reflectivity of the sample at high intensity can only come from a flatness in the bilayer's dispersion. This is by choice, as we have no informed knowledge of an electronic saturation behaviour. A model assuming a saturation of the permittivity modulation in the form $\Delta\omega_p \propto \tanh(aI/I_{\text{sat}})$ did not yield further improvements to the rise and plateau of the modulation, and was rejected as it did not provide new insights on the medium while introducing extra fitting parameters. Differences could also arise from the change in the damping term γ in the Drude model, but this was again tested and rejected as it introduces a fine tuning problem without improving the matching between experiment and theory. To summarise, the saturation of the reflectivity change with intensity $R(I)$ due to the dispersion of the sample prevents any observation of a modulation of the permittivity $\epsilon_r(I)$ that could originate from the electron dynamics in the medium. Using an ab-initio solid state model, Wai Un et al. [80] suggest there is no such electronic saturation behaviour of permittivity, in agreement with our choice of modelling the ITO plasma frequency as $\Delta\omega_p = \alpha I$.

In the semi-analytical model as well as in experiment, the spectrally integrated measurements cannot show dynamics faster than the probe pulse width 225 fs. Very little can then be inferred about τ_{rise}, which is here assumed to be 30 fs as this corresponds to a reasonable value below the shortest pulse width of 50 fs used in literature to investigate the temporal response of ITO [78]. The following chapters will provide an alternative method to measure the dynamics within the medium by looking into the spectral features of the probe. The plateau at high intensity, on the other hand, informs us that additional dynamics are at play. Particularly, the

pump is driving itself outside of the medium: for a pump field driving the electrons at a time t, the reflectivity will increase and pump light arriving at $t + \delta t$ will couple less efficiently to the ITO layer. This creates a feedback loop, where the pump intensity in the medium evolves step by step depending on its previous state. Our semi-analytical theory accounts for this by iterating the pump field intensity in the medium a second time once the reflectivity evolution has been computed, and updating the reflectivity for the probe accordingly. If the pump modulation is left unrestrained, for the same parameters, the pump overshoots and the reflectivity saturates due to the Berreman resonance dispersion as can be seen in Fig. 3.8(b), drastically changing the dynamics of the simulated pump-probe. In the end, a semi-analytical model with a minimal number of parameters (α, τ_{rise} and τ_{decay}) and self-modulation reproduces the change in reflectivity under optical pumping with a good accuracy, without overreaching into the less know aspects of said optical pumping.

3.3.3 Self modulation of the probe pulse

The effects of pump self-modulation draw our attention to the importance of the pump and probe pulse properties. As we have so far focused on characterising optical modulation of permittivity in the ITO layer in terms of the bilayer and its dispersion, we will now look into the effects of pulse properties - mainly intensity and duration - on the modulation performances.

Though we have gained understanding on pump self-modulation in the previous section, the probe's self modulation still needs characterisation. The probe can change the permittivity of the medium just as well as the pump, which is why its intensity must be kept low and its power even lower due to its smaller beam waist. When increasing the probe power, the collected signal should be increasing proportionally as well and the reflectivity will stay constant, but as Fig. 3.9(a) shows this is not the case: the reflectivity of the sample increases for intensities comparable to that used for the pump modulation. For this reason, we keep the probe power below 1 GW/cm^2 to ensure a maximum contrast. Furthermore, at high intensities, the probe also modulates its own spectrum: the spectral broadening usually observed in nonlinear optical self modulation is visible in Fig. 3.9(b), as well as a slight blueshift due to the phase change within the medium and the asymmetry in time of the probe self-modulation. Recall from section 2.1.2 that though the parametric optical Kerr effect linked to photon-photon scattering through virtual states, as it is instantaneous, can only induce broadening, the non-parametric Kerr modulation in ITO on the other hand is due to carrier dynamics and thus can induce frequency shifts thanks to its asymmetric and finite nature in time.

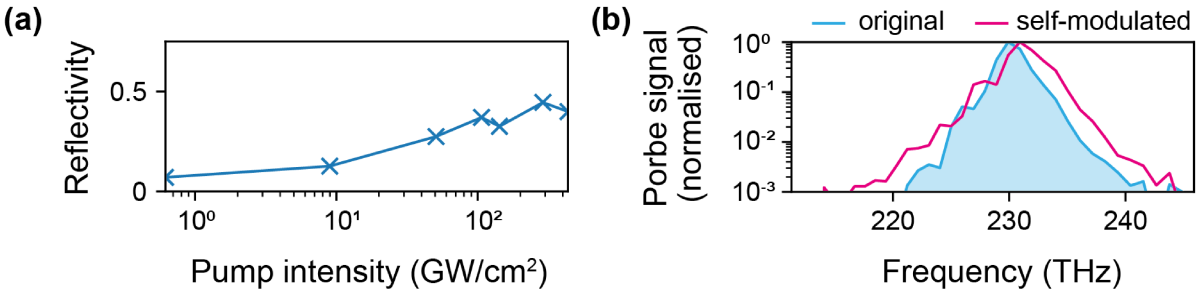

Figure 3.9: Probe pulse self modulation. **(a)** Sample reflectivity as a function of probe pulse intensity for a frequency of 230 THz and an angle of 65 degrees. **(b)** Original unmodulated probe pulse spectrum (light blue curve) against a probe spectrum with intensity of 436 GW/cm^2 reflected from the bilayer (pink curve).

3.3.4 Control and effects of the probe pulse duration

The conclusions from the probe intensity dependent properties of the modulation being simple - that is the importance of a low probe power and intensity - the role of the probe pulse width in time is the next and last item to be investigated in this chapter. This will be particularly important in the context of chapter 5 where a long probe in time is required to observe a double slit in time: the probe pulse needs to be long enough in time to experience the rise and decay of both slits. This can be explained by an analogy to the quantum mechanical picture of the famous double slit experiment in space: for a photon to have an interference pattern probability, there needs to be an uncertainty with regards to which slit in space it went through. If the slit through which the photon passes through is known, the interference pattern disappears. The same holds for the experiment in time: the photon needs to be delocalised in time - i.e. for a classical wave to have a large enough temporal width - in order not to know which slit in time it went through and observe the interference pattern.

We can study the role of the pulse duration only by extending it via a classic 4-f system. This is a well-know optical system made of two gratings, two lenses and a slit, all at a focal distance of each other, giving it its name. The 4-f system is represented in Fig. 3.10(a). The incident pulse, with a carrier frequency of 230 THz and a width of 2.8 THz, is reflected by a blazed NIR grating, which spatially separates its frequencies. The first lens then performs a Fourier transform of this spectral separation, thus allocating each frequency f to a position x in its Fourier plane. The slit operates a spatial selection on the beam, and thus selects any frequency comprised in its aperture $A(x)$, as shown in Fig. 3.10(b). The spectrally filtered beam is then recollimated and recollected in frequency with the outgoing lens and grating. Hence, due to the time-bandwidth product and the fundamental principles behind the Fourier transform of a Gaussian, the spectral filtering results in a longer pulse in time. Controlling the

width of the slit aperture $A(x)$ allows us to control the spectral filtering and thus the duration of the probe pulse.

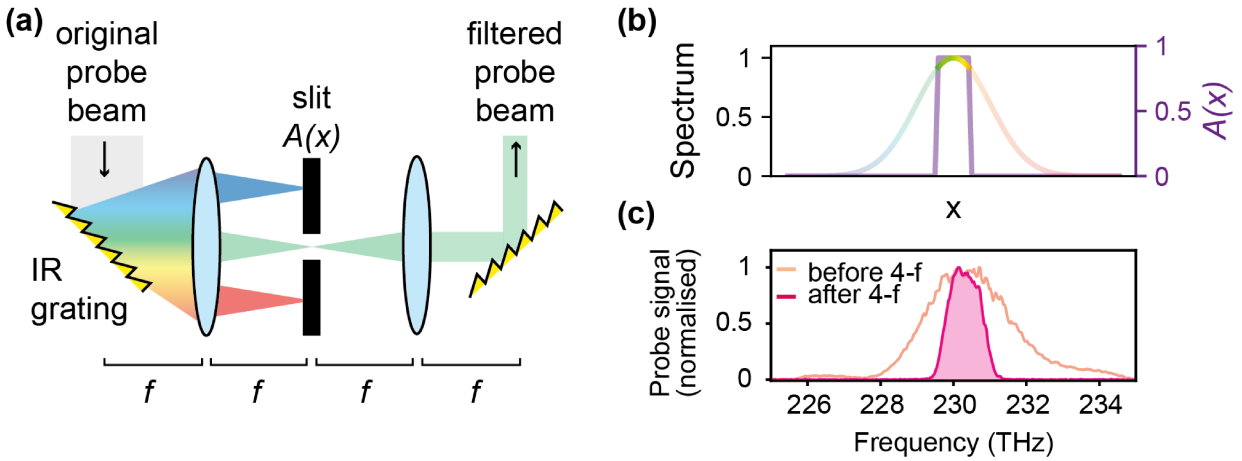

Figure 3.10: Spectral filtering in a 4-f system. **(a)** Diagram of the 4-f system. **(b)** Diagram of the distribution of frequencies along the slit's plane: each frequency, represented by a color on the rainbow curve, corresponds to a precise location x, creating a spectrum in space (multicolored curve). The slit aperture (purple curve) selects the spectral content on the axis. **(c)** Measured spectrum before (beige curve) and after (pink curve) a 300 µm aperture in the 4-f system. Reproduced from [81].

The spectrally filtered spectrum is shown in pink in Fig. 3.10(c). With a bandwidth of 1 THz, it is spectrally narrower than the original probe pulse of 2.8 THz bandwidth, shown in beige. One could use the time-bandwidth product to estimate the duration of the pulse, as $\tau \times \delta f = 0.44$ for a Gaussian pulse, τ being the pulse FWHM in time and δf the FWHM in frequency. Yet, it can be seen from the measured spectra that both the original and the filtered pulses are not perfectly Gaussian. This is because the original pulse from the laser is not bandwidth-limited (i.e. $\tau \times \delta f > 0.44$), and the filtered pulse is the product of the Gaussian part of the original spectrum with a top-hat function, leaving roughly a top-hat shape with a curved top.

To rigorously characterise the temporal profile of the filtered probe pulse, we use auto and cross-correlation measurements. These are measurements techniques that can be implemented in the pump-probe setup, consisting in measuring a nonlinear signal coming from the interaction between two pulses as a function of delay, as shown in Fig. 3.11(a). In our case, we look at sum frequency generation (SFG) in a 400 µm thick GaP layer with second order nonlinearities. As the delay reduces and the two pulses overlap in time, the SFG signal will increase, which leads us to observe the convolution of the two pulses as a function of delay. Knowing the pulse shape, a FWHM can be calculated.

For the measurement to be accurate it is important for the group velocity mismatch, also

referenced to as walk-off, to be negligible, so that the measured pulse shape does not appear distorted. If the two pulses walk off, the resulting bandwidth will be affected and the pulse will appear longer. In GaP, the phase matching bandwidth is given for a Gaussian pulse by

$$\Delta f = \frac{0.44}{L \times \mathrm{GVM}} \tag{3.4}$$

where L is the propagation length and GVM is the group velocity mismatch expressed as

$$\mathrm{GVM} = \left(\frac{1}{v_g(2f)} - \frac{1}{v_g(f)} \right) \tag{3.5}$$

Using ellipsometry data informing us on the refractive index of GaP, we compute the phase-matching bandwidth for a 400 µm GaP layer to be of 0.25 THz for a carrier frequency of 230 THz. This is below the bandwidth of the pulses used in the experiment and would be problematic if not for the phase-match in GaP. As opposed to the walk-off bandwidth, originating from the group velocity, phase-mismatch is due to the phase velocity of the respective pump and SFG pulses. As such, the resulting nonlinear coherence length dictates the distance over which the SFG signal can be generated, which is computed to be of 468 nm in GaP at 230 THz (using $L_{coh} = \pi \Delta k$ where $\Delta k = k(2f) - k(f)$ is the wavevector mismatch. Over this distance, the two pulses don't have time to walk off due to group velocity and the bandwidth needs to be recalculated with $L = L_{coh}$ and yields a value of 209.8 THz, much above the bandwidth of the pulses. We can thus expect the outgoing SFG pulse to give precise information on the two pulses at its origin.

Auto-correlation refers to the pump pulse interacting with itself to generate SFG, with momentum being used as a tool to differentiate it from SHG. Once the pump pulse width is known, the probe pulse width is determined using cross-correlation with a pump pulse. An analytical expression can be obtained for the FWHM of the convolution of two Gaussian curves:

$$\tau_{cor} = \sqrt{\frac{\tau_1^2}{2} + \frac{\tau_2^2}{2}} \tag{3.6}$$

where τ_{cor} is the FWHM of the measured SFG signal, in intensity, and τ_1 and τ_2 are the field amplitude FWHM of the two pulses used in the correlation measurement. For auto-correlation, this reduces to $\tau_{autocor} = \tau_{pump}$, and for cross-correlation $\tau_{probe} = \sqrt{2\tau_{Xcorr}^2 - \tau_{pump}^2}$.

The SFG signal as a function of delay for the pump-probe auto and cross-correlation measurements are shown n Fig. 3.11(b). One can see the curves are clearly Gaussian and can be easily fitted. The pump auto-correlation is shorter than the probe cross-correlation as the

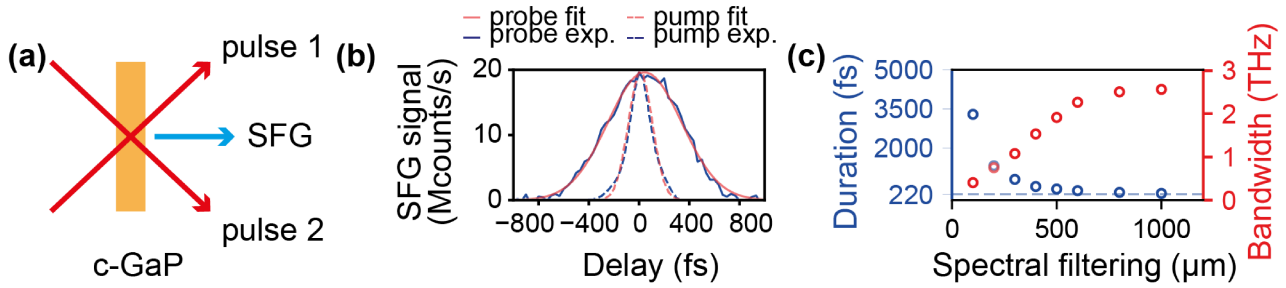

Figure 3.11: Auto and cross correlation measurements. **(a)** Diagram of SFG in a correlation measurement: the two non-colinear beams intersect in the GaP layer, generating the SFG signal at an intermediate angle. **(b)** SFG signal as a function of delay between the two pulses in a correlation experiment. The measured Gaussian signals (blue curves) are fitted (pink curves) to extract a FWHM used to estimate the pulse duration. The pump and unfiltered probe pulses are first measured through auto-correlation (dashed curves), and this information is used when measuring the filtered probe pulse, here with a 300 µm slit (continuous curves), which shows a larger FWHM. The auto-correlation signal is normalised to that of the cross-correlation for clarity. **(c)** Measured temporal duration (blue dots) and spectral bandwidth (red dots) of the spectrally filtered probe pulse, as a function of slit width. The grey dashed line indicates the base level of the unfiltered pump and probe pulse. (b) and (c) reproduced from [81].

probe is spectrally filtered with a 300 µm slit, making it longer in time. One artefact from the spectral selection is that the probe spectrum is close to a top-hat, and as a consequence its Fourier transform (the probe field in time) is sinc-shaped. We choose to ignore the side lobes with low intensity and approximate the main peak as a Gaussian, which as our cross correlation experiments show is a valid approximation. Fitting the Gaussian curves allows to extract a temporal FWHM as a function of 4-f slit aperture, shown in Fig. 3.11(c), which is compared to the FWHM in frequency. As expected, as the spectral filtering increases by decreasing the slit aperture, the spectrum gets narrower in frequency. As a result, the probe pulse becomes longer, with an inverse proportionality to the spectral width. For the pump pulse (and unfiltered probe), the width is determined to be of 225 ± 5 fs, close to the laser's specified width of 220 fs. Note that though spectral filtering gives control over the probe pulse length in time, it comes at the expense of power as a significant share of the probe pulse is cut out for smaller slit apertures.

Finally, broadening the probe pulse in time will have an impact on the perceived modulation of the medium. For a modulation of the reflectivity showing the same timescale as the probe pulse, as shown in Fig. 3.12(a), the majority of the probe pulse in time undergoes the modulation. For a probe pulse whose duration is 5 times longer, only 1/5 of it observes the modulation (Fig. 3.12(b)). As a result, one can expect the reflectivity modulation to be reduced by a factor of 5, as a vast portion of the probe remains untouched. This is experimentally verified by observing a lower reflectivity change as a function of delay, over a longer rise and decay

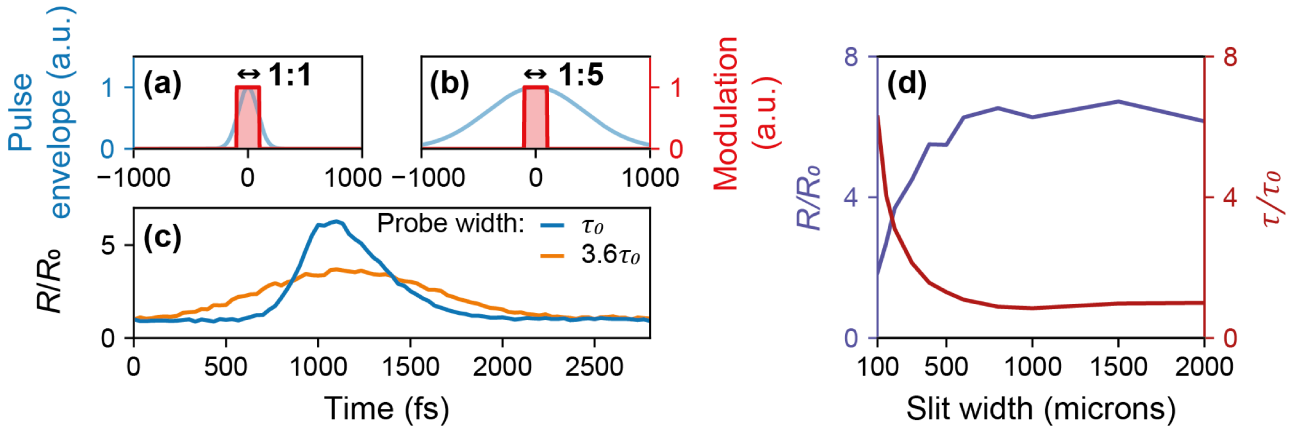

Figure 3.12: Effect of probe pulse duration on the observed modulation. **(a,b)** Diagram of a square modulation (red curve) and a probe pulse (blue curve) with (a) the same FWHM of 200 fs and (b) a probe duration 5 times superior (1000 fs). **(c)** Relative reflectivity change R/R_0 against delay for two probe pulses with different widths at a fixed pump intensity. **(d)** Measured ratio of reflectivity change R/R_0 (dark blue curve) and matching pulse duration ratio τ/τ_0 (dark red curve) against the spectrally filtering 4-f slit width.

time, in Fig. 3.12(c) for a longer probe pulse. One can also notice the asymmetry disappear as the decay of the modulation is now shorter than the probe pulse's width in time.

This effect of probe duration on the modulation amplitude is further studied by comparing the relative reflectivity change against the relative probe width change for different 4-f slit widths, as shown in Fig. 3.12(d). The reflectivity change R/R_0, where R is the modulated reflectivity and R_0 the unmodulated base value, follows the exact inverse of the probe pulse duration τ/τ_0 where τ is the FWHM of the stretched probe in time and τ_0 its original FWHM. As the slit gets narrower and the probe pulse longer in time, the reflectivity change decreases. This will reduce the time-varying effects induced by the slit, and a compromise will be used in chapter 5 to balance a longer pulse in time and a visible slit effect.

3.4 Conclusion

In conclusion, a single slit in time was demonstrated under all-optical pumping in a 40 nm ITO bilayer, thanks to the material's high nonlinear properties and the use of the Berreman resonance. The high contrast (1000%, or 0.59 in absolute reflectivity) and short rise time (pulse-limited or below) of the slit make it an excellent platform to study diffraction in time. By scanning the parameter space, precious insight on the various mechanisms at play within the modulation and the pump and probe pulses was gained. Particularly, saturation of the optical modulation within the medium is found to create a new regime where the sample's properties deviate from expectations, leading to new dynamics that could potentially affect time-varying

effects on the probe. With a better understanding of the modulation and how to model it, as well as a solid experimental method, we can now head on to the main challenge that is spectral diffraction at optical frequencies.

Chapter 4
Single slit diffraction in the time-domain

4.1 Introduction

Having demonstrated and characterised the appearance of a slit in time in ITO thin films under all-optical pumping, we can now turn our attention to diffraction in the time domain by examining the probe spectrum after interaction with the medium. Early works and in particular Zhou et al. first demonstrated time refraction in a 620 nm thin film of ITO [64], and thinner layers have been used to the same effect since [67]. Our experiments rather focus on time-varying mirrors, that can be switched on and off on short time scales. Along the time refraction effects linked to propagation in a changing medium, resulting in frequency shifts, we aim to observe diffraction from a mirror being switched on and off in time, that is a slit in time inducing a broadening or thinning of the spectrum. As both refraction and diffraction are here results from scattering by a temporal interface, respectively in phase and amplitude, we hope to better separate the two effects by selecting the appropriate platform. Note that in the coming chapters, the term diffraction will be applied to the temporal modulation from a single or double slit, even though the effects of time refraction can simultaneously be observed.

Here, we investigate an ITO/gold bilayer as it provides both the advantages of a high contrast in modulated reflectivity, and minimal spatial extent for propagation of the probe. This will allow us to characterise the spectral modulations resulting from a single slit in time. A particularly unexpected result lies in strong spectral modulations at high intensities, much beyond what could be expected from state of the art time-varying models.

4.2 Time-varying signatures in a single slit experiment

4.2.1 Measurement of diffraction in time at low pump intensity

The vast majority of experimental and theoretical data presented in chapter 3 is spectrally integrated, under the assumption that the probe pulse is narrower in frequency than the sample's resonance, such that a single reflectivity value can be attributed to the entire spectrum. This

delivered powerful insights on the modulation mechanisms and behaviour, and allowed us to optimise the temporal slit design. We will now turn our attention to the spectral time-varying effects by exploring the same pump-probe measurements but focusing on the full spectrum.

Fig. 4.1(a) shows the measured probe spectrum as a function of delay on a logarithmic scale, for the optimal modulation frequency and angle (230 THz, 65 degrees incidence) determined in the previous chapter. The intensity here is kept low at 22 GW/cm^2, well below the saturation of the reflectivity modulation with pump intensity shown previously in Fig. 3.7(a). The spectrum changes quite visibly near its zero delay, with side lobes appearing at negative delay while the main peak narrows down, followed by a broad peak at positive delay. This result is in very good agreement with the semi-analytical model presented in section 2.3.2 and shown in Fig. 4.1(b). Spectral changes are more visible for slightly negative delays, which correspond to the rise of the reflectivity where the gradient of the time modulation of the complex reflection coefficient is strongest.

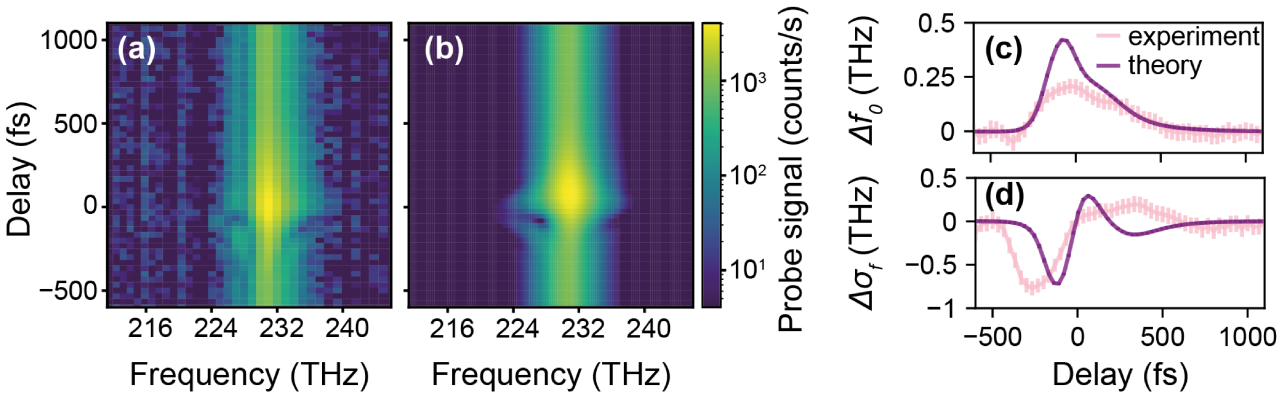

Figure 4.1: Bilayer spectral scans with delay at low intensity. **(a)** Measured probe signal in logarithmic scale as a function of frequency and delay at a pump power of 22 GW/cm^2. **(b)** Theoretical prediction of the spectral modulation using the semi-analytical model. **(c,d)** Spectral shift (c) and broadening (d) as a function of delay, as extracted from experiment (pink curves) and the semi-analytical model (purple curves) by fitting a Gaussian to the reflected probe spectrum at each delay. Panels (a) and (b) reproduced from [79].

Frequency shift (Δf_0) and broadening ($\Delta\sigma_f$) in the probe spectrum are extracted by fitting the main frequency peak with a Gaussian. Note that this approach does not give insight on the full range of generated frequencies, as it neglects any information (i.e. spectral features) beyond the fitted Gaussian shape. As shown here in Fig. 4.1(c), frequency shifts are fairly limited with a maximum value of 0.21 THz, smaller than the shifts observed in other, thicker ITO systems [64, 78]. A close comparison can be made with the 115 nm thick ITO thin film studied by Bohn et al. [67], which observed a maximum shift of the order of 0.6 THz for intensities of 400 GW/cm^2. Defining a figure of merit of shift per intensity (in THz.cm^2/GW)

[77], the bilayer can be considered to be 6 times more efficient with 9.5 MHz.cm^2/GW against 1.5 MHz.cm^2/GW [67]. This is likely due to the fact that, though the layer thickness is smaller, the stronger resonance in the bilayer enables stronger frequency shifts upon modulation.

Broadening ($\Delta\sigma_f$), on the other hand, exhibits stronger features, as can be seen in Fig. 4.1(d). The probe pulse narrows down by 0.77 THz (about 30% of its width), and then broadens up by 0.2 THz, from an original pulse width of 2.8 THz. The reduction of the bandwidth happens at the same delay on the rise time than the generation of side bands in the spectrum akin to those observed in spatial single slit diffraction, suggesting a transfer of energy between different frequencies. On the other hand, the broadening of the spectrum corresponds to the slow decay of reflectivity following the relaxation of the electrons in the conduction band. The semi-analytical model, with its adiabatic approximation, reproduces the shift and broadening with good fidelity, though it overestimates the phase shift, likely due to the unrestrained refractive index change leading to exaggerated temporal changes in the reflection coefficient's phase.

4.2.2 Shift and broadening under optical pumping

To better understand the shift and broadening of the probe pulse, we need to dive back into the model presented in section 2.3. Fig. 4.2(a) and (b) show the amplitude $\rho = |r|$ and phase ϕ of the complex reflection coefficient $r = \rho e^{i\phi}$ as modelled by the semi-analytical theory from section 2.3.2 for a pump intensity of 22 GW/cm^2. Remembering that changes in amplitude are related to broadening and changes in phase to frequency shifts, the modelling of the complex reflection coefficient against frequency and delay gives insights on the time-varying physics. For the amplitude $\rho = |r|$, the strongest change in amplitude with delay is obtained at a frequency of 230 THz, as expected from the Berreman resonance. Frequencies above 230 THz undergo a a smaller increase, while frequencies around 220 THz undergo a sharp series of decrease and increase on the rise, and slower decrease and final increase on the decay of the modulation in reflectivity as a function of delay. For the phase ϕ, frequencies below 230 THz undergo the strongest phase changes as they cross the full resonance. The Berreman resonant frequency of 230 THz undergoes half of this frequency shift, while frequencies above observe little change in phase.

The correspondence between the complex reflection coefficient evolution and the observed spectral modulations in the ITO bilayer is shown here in Fig. 4.2(c-f). The change in time of the amplitude and phase of the Fresnel coefficient of the bilayer are sketched in Fig. 4.2(c)

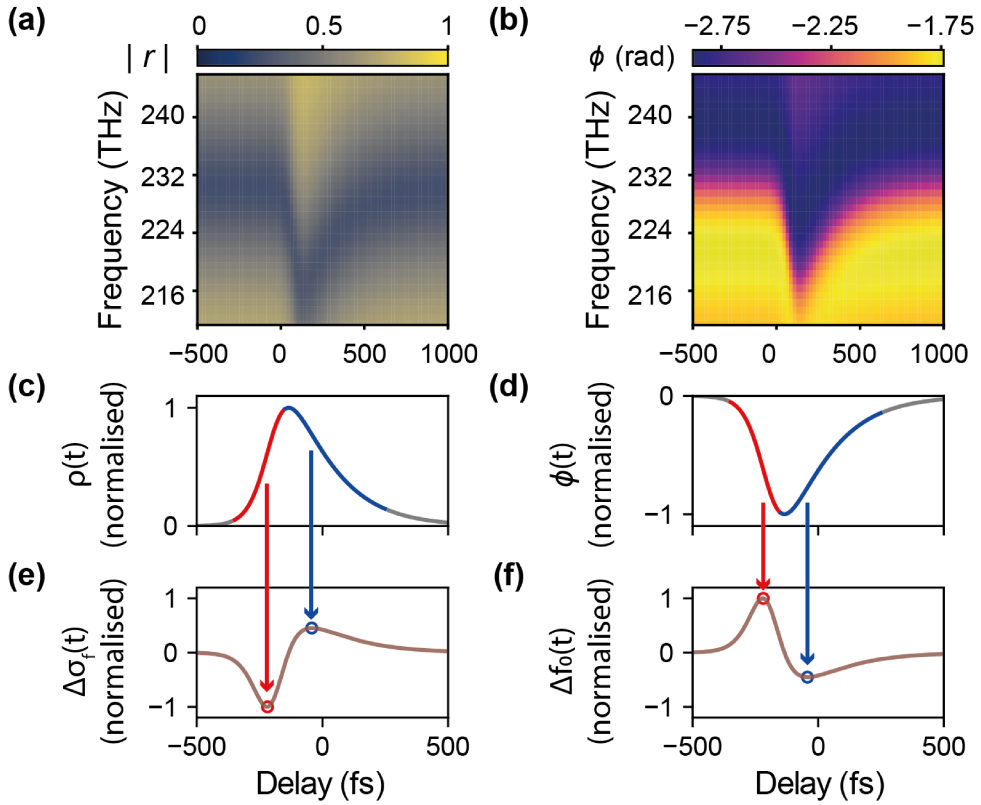

Figure 4.2: Correspondence between the complex reflection coefficient change and the observed spectral modulation. **(a,b)** Complex reflection coefficient of the bilayer in (a) amplitude and (b) phase as a function of frequency and delay, as predicted by the semi-analytical model for a pump intensity of 22 GW/cm^2. **(c,d)** Diagram of the complex reflection coefficient evolution in time in (c) amplitude and (d) phase. The rise and decay of the modulation are highlighted in red and blue respectively. **(e,f)** Corresponding change in probe pulse (c) bandwidth and (d) carrier frequency. The peaks, indicated by the red and blue circles, correspond to the color-matched slopes in panels (c) and (d). Panels (a) and (b) reproduced from [79].

and (d), with rise and decay respectively highlighted in red and blue. The resulting broadening and shifts in Fig. 4.2(e) and (f) from a probe seeing said amplitude and phase change in the reflection coefficient will see a decrease or increase corresponding to an arrival time of the probe on the rise or decay of the modulation, highlighted by the blue and red arrows - with a maximum slope corresponding to a peak in modulation (remember that frequency is a derivative of phase with respect to time.).

Let us now look at the experimental frequency shift and broadening as a function of delay and pump intensity in light of the complex reflection coefficient. Experimental measurements are shown in Fig. 4.3(a) and (b) for a pump-probe carrier frequencies of 230 THz, at pump intensities of 6.99 GW/cm^2 (light blue curve) and 39.22 GW/cm^2 (dark blue curve). As it turns out, the positive frequency shift is strongest at low intensities at slightly negative delay, on the rise of the modulation. Little to no redshift is visible at low pump intensities for the frequency of 230 THz.

As noted earlier, a carrier frequency of 220 THz, below the Berreman mode, will fully cross the resonance and experience a stronger phase shift. This is visible in Fig. 4.3(b) where the measured frequency shift is plotted against delay for pump intensities of 6.74 GW/cm^2 (brown curve) and 38.26 GW/cm^2 (orange curve) for a carrier frequency of 220 THz. The blueshift reaches a larger value on the rise of the modulation than for the 230 THz probe pulse. While for a 230 THz probe pulse the best shifting efficiency was recorded with a figure of merit of 42.9 MHz.cm^2/GW at 6.99 GW/cm^2 , the 220 THz probe pulse shows an efficiency of 119.7 MHz.cm^2/GW for a similar pump intensity of 6.74 GW/cm^2. This shows the important role of resonance crossing in frequency shifting. This is also highlighted by the redshift on the decay of the modulation, which is present at 220 THz and not 230 THz.

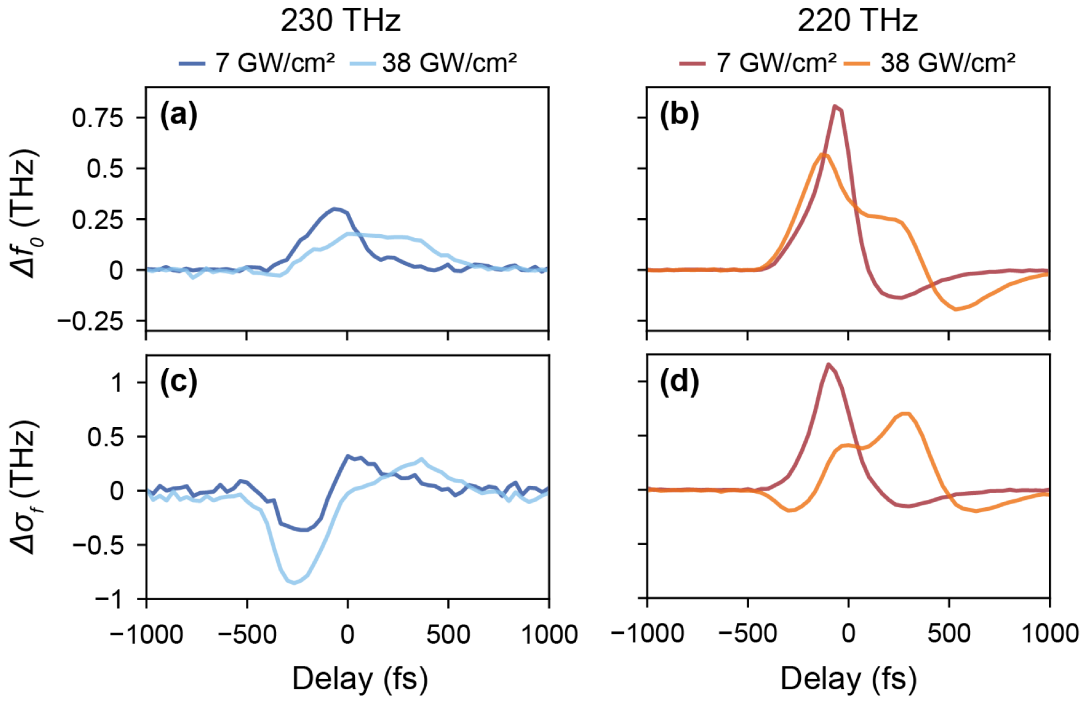

Figure 4.3: Shift and broadening in the bilayer for low pump intensities. **(a,b)** Frequency shift and **(c,d)** broadening of the reflected probe pulse as a function of delay for frequencies of (a,c) 230 THz (dark and light blue curves) and (b,d) 220 THz (brown and orange curves), at pump intensities of 7 GW/cm^2 (brown and dark blue curves) and 38 GW/cm^2 (orange and light blue curves). Adapted from [79].

Regarding the probe pulse bandwidth, a successive narrowing and broadening are observed for the probe at 230 THz in Fig. 4.3(c), near zero delay, at the rise and decay of the modulation. The bandwidth decrease is larger at a higher pump intensity, which is a consequence of a larger amplitude modulation. On the other hand, the broadening of the probe pulse on the decay of the modulation does not significantly change with pump power, which could be a consequence of the increase in decay time with increasing pump intensities.

Interestingly, in Fig. 4.3(d) the probe bandwidth seems to undergo different dynamics at

220 THz. At low intensity, the broadening is quite strong, with the bandwidth increasing by ∼ 1 THz, with little narrowing. This dynamic is opposite to that observed at 230 THz, which is linked to the decrease rather than in increase in reflectivity for 220 THz at low pump intensities. When the pump intensity is increased, the probe at 220 THz exhibits richer dynamics as it crosses more of the Berreman resonance and sees a reflectivity increase. Hence, in single slit diffraction in time, dispersion has great influence on the reflected probe spectrum.

4.3 Ultrafast dynamics in the saturation regime

4.3.1 Large broadening from time diffraction at high pump intensities

Using smaller beam sizes and the maximum available amount of pump power from our laser, high intensities up to 700 GW/cm^2 can be achieved within the pump-probe setup. Fig. 4.4(a) shows the measured probe signal against frequency and delay for a pump intensity of 708 GW/cm^2. As expected, the spectral signature of the modulation at negative delay is much larger than at low intensities (see Fig. 4.1(a)), showing a large broadening in the red end of the spectrum due to the reflectivity modulation being pushed further. The newly generated frequencies extend from 214 up to 245 THz, with 10^{-3} smaller intensity than the modulated main peak. In other words, the generated frequencies have an amplitude of 1% of the unmodulated probe peak frequency. The spectrum is also much more asymmetric than at low intensity, which we attribute to the additional changes in the phase of the complex reflection coefficient.

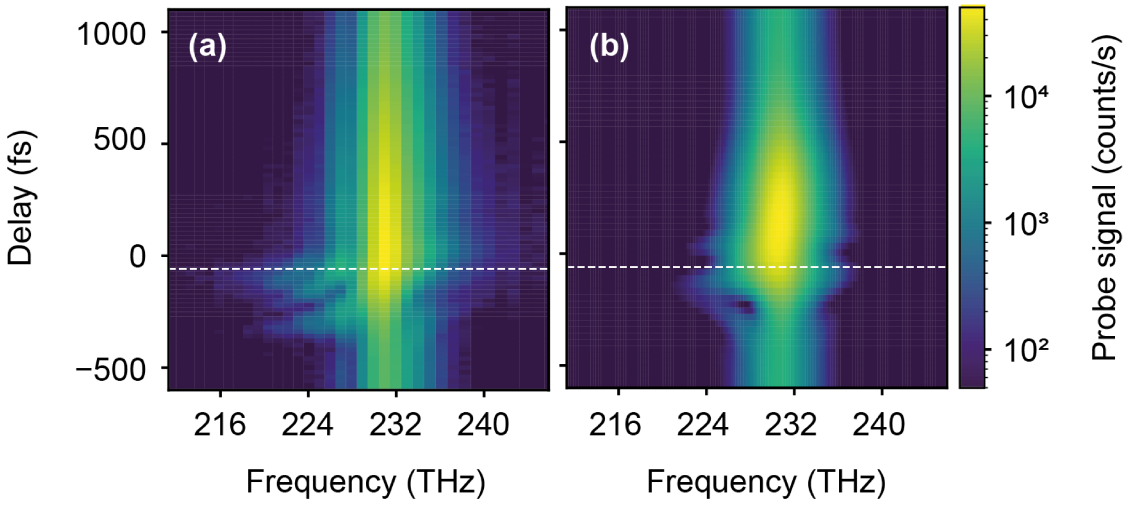

Figure 4.4: Bilayer spectral scans at high intensity. **(a)** Measured logarithmic probe signal against frequency and delay for a pump intensity of 708 GW/cm^2. **(b)** Corresponding simulated spectra against delay, obtained using the semi-analytical model. The white dashed lines represent the delay at which the spectra will be presented in Fig. 4.6. Reproduced from [79].

One can note that extracting the shift and broadening at this pump intensity by fitting a Gaussian or sech^2 function to the measured frequencies will poorly represent the time-varying effects in spectrum, as the main peak of the signal remains relatively unchanged - with a maximum shift of 0.3 THz and broadening of 0.2 THz. This is a point we will come back to later when discussing the dynamics of the medium. If we consider the modulated spectrum to be constituted of a two signals, one being the main peak with large amplitude and little modulation, the other being a weaker modulation with the many generated frequencies, a counter-intuitive result is obtained: the modulated signal is an order of magnitude larger in bandwidth than the pump and probe pulses. By experimentally knowing the amplitude change of the reflection, and from the properties of Fourier transforms, the pump pulse envelope dynamics couldn't justify the measured extent of generated frequencies. This means the pump modulation dynamics in the medium are at least an order of magnitude below the pump pulse duration.

We use theoretical predictions from the semi-analytical model from section 2.3.2 to gain further insights on the dynamics of the medium in the saturation regime. The simulated probe spectrum as a function of delay is shown in Fig. 4.4(b), and though the model reproduces the fine spectral features with good accuracy, it cannot reproduce the extent of the broadening observed experimentally. In the end, the semi-analytical model can display a shortening of the rise time (here defined as 10-90%) of the reflectivity modulation down to a value of 60 fs. This value of 60 fs is shorter than the pump envelope's rise time of 115 fs (10-90%) as the reflection coefficient amplitude stays constant beyond the Berreman resonance, effectively inducing an artificial saturation where the maximum change in amplitude is obtained faster under higher intensities. Thus, the semi-analytical model does not provide a satisfying answer to the fast time scales observed experimentally, and this is likely due to the adiabatic approximation imposing the pump width dynamics to the modulation of the medium.

This change in rise time of the modulation with pump intensity can also be observed thanks to the frequency shift of the main peak. As shown in Fig. 4.5(a), at high intensities above 100 GW/cm^2, a redshift appears a slightly negative delays. This is quite contrasting to the results at low pump intensity, where no redshift is observed and blueshift is achieved at negative delays on the rise of the modulation, while now the redshift is observed on the decay, following the dynamics of the increase in decay time. This can only mean that new mechanisms and dynamics come at play within the medium in the saturation regime.

Meanwhile, the dynamics are not inverted for the broadening of the main peak: the pulse bandwidth shown in Fig. 4.5(b) shows the appearance of the plateau of the modulation of reflectivity, where little broadening is observed, and the increase in decay time of the modulation

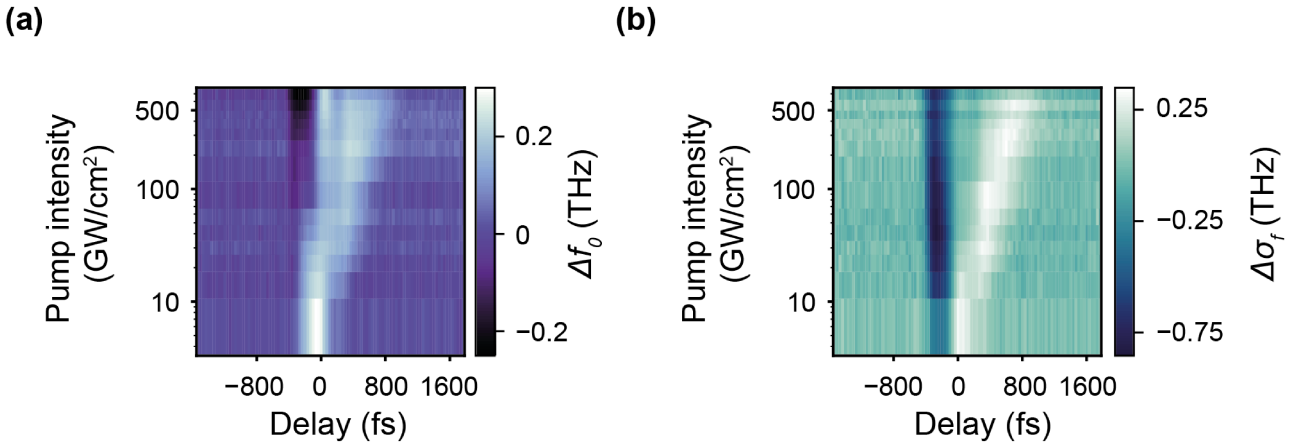

Figure 4.5: Shift and broadening in the bilayer as a function of pump intensity. **(a)** Spectral shift and **(b)** broadening as a function of delay and pump intensity for a degenerate pump probe experiment at a carrier frequency of 230 THz. Reproduced from [79].

with a broadening of the pulse happening at later and later times as pump intensity increases. The narrowing of the spectrum on the rise time of the modulation does not change at higher pump intensities, as only a small portion of the probe pulse if affected by the rise time and as a consequence the newly generated frequencies have intensities well below the main peak's FWHM.

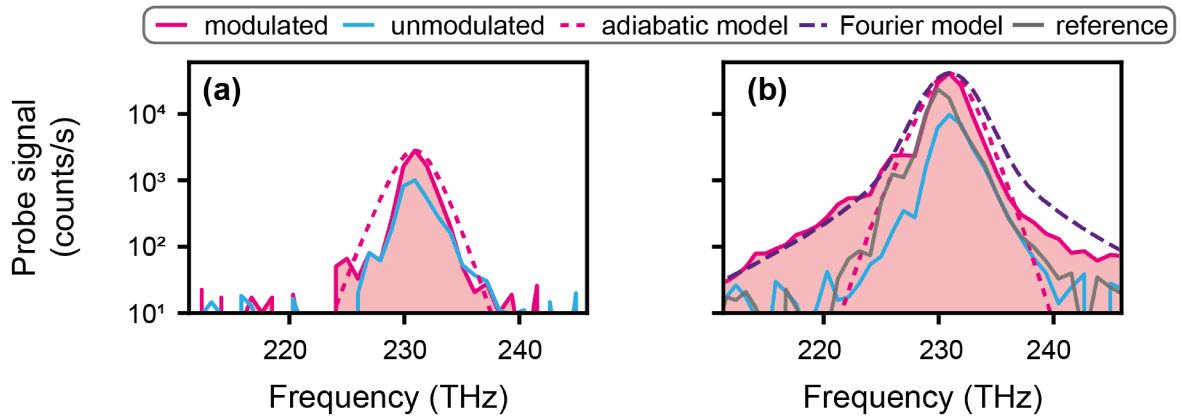

Figure 4.6: Modulated spectrum against original spectrum and theoretical prediction. **(a)** Low intensity (22 GW/cm^2) spectra: the measured spectrum (continuous pink line) matches the semi-analytical model's prediction (dashed pink line) and is similar to the unmodulated spectrum (light blue line). **(b)** Experimental high intensity (708 GW/cm^2) modulated spectrum (continuous pink line): there is now a considerable difference with the adiabatic theory (dashed pink line) as the probe is considerably broader than when unmodulated (light blue line). A Fourier transform simulation with a fast rise time (dashed purple line) fits the resulting spectrum much better. A reference probe spectrum, with no interaction with the ITO layer, is shown in grey to highlight the generation of visible frequencies beyond the increase of probe signal. Adapted from [79].

Note that this does not mean the semi-analytical model is fundamentally wrong, rather, just as it didn't account for a lengthening of the decay time at high intensities, it is likely

not accounting for intensity-dependent electron dynamics. Comparing in Fig. 4.6(a) the experimental (continuous pink curve) and simulated spectra (dashed pink curve), a reasonable agreement is found. This is likely because the modulation is still small, in below the saturation regime. There, the dynamics in the medium do not change significantly with pump intensity and small scale spectral modulation is observed when compared to the original probe signal (light blue curve). Furthermore, Bohn et al. showed that the model can reproduce spectral shifts with great accuracy with similar measurements in ITO [52, 67]. A different explanation for our results would be that the dynamics of the modulation in ITO at high intensities involve new behaviour from the intraband electrons that lie beyond the presented adiabatic model.

4.3.2 Fourier modelling and fitting of the rise time

It is therefore necessary to introduce an alternative model which can replicate the new time scales corresponding to the observed broadening at high frequency while simultaneously reproducing the modulated spectrum. For this reason, the semi-analytical model presented in section 2.3.2 will be replaced by the simpler Fourier model described in section 2.3, using equation 2.13, that we will remind here:

$$S(f) = \mathrm{FT}\left[r(t) \times E_{probe}(t)\right](f) \tag{2.13}$$

where $E(t)$ can be calculated by assuming the probe pulse is Fourier limited, and taking the Fourier transform of the unmodulated spectrum. The aperture function, here the complex reflection coefficient $A(t) = r(t)$, will be a guess function whose rise and decay time can be tuned independently, without any connection to the medium or the pump pulse properties as in the semi-analytical model and solely fitted to the data. This allows very fast rise times to be included in the model. On the other hand, the Fourier model does not account for either dispersion or the phase of the complex reflection coefficient. The Fourier model's purpose is to investigate the timescales by reproducing the extent of broadening. Note that the Fourier model has fitting parameters that are adjusted to the experimental spectra, in contrast to the semi-analytical model where the dynamics have no fitting parameters but require a good representation of the pump-induced changes of $\epsilon(\omega)$.

We choose to heuristically model the reflection coefficient in time as following:

$$\rho(t) = \frac{1}{(1 + e^{-\alpha t}) \times (1 + e^{\beta t})} \tag{4.1}$$

where α and β are positive values related respectively to the rise and decay times. The reflection coefficient is then normalised to fit the experimentally observed modulation in intensity, i.e applying:

$$r(t) = A \times \frac{\rho(t)}{\max(\rho(t))} + C \tag{4.2}$$

with A and C chosen so that $R(t) = |r(t)|^2$ has the same maximum and minimum values than the experimentally measured reflectivity.

The β coefficient can be fitted thanks to the spectrally integrated pump-probe scans, as the decay of the modulation is slower than the probe pulse envelope, a change in β will be visible in the integrated counts against delay. Fitting the convolution $R(t) * |E_{probe}|^2$ to the experiment gives $\beta = 1/400$ fs^{-1}, corresponding to a decay time of 625 fs (90-10%). The coefficient α representing the rise time of the modulation, on the other hand, is fitted to the spectral extent of the modulated data.

To put the Fourier model to the test, the modulated spectrum at the high intensity of 708 GW/cm^2 is shown in Fig. 4.6(b). The experimental spectrum (continuous pink curve) extends much further than the prediction from the semi-analytical model (dashed pink curve) as seen in Fig. 4.4. The Fourier model prediction is shown in dashed purple, and matches very well the broadening of the experimental spectrum for lower frequencies. The asymmetry of the spectrum likely originates from redshift during the modulation, which is not accounted for in the Fourier model. To match the experimental spectrum, α needs to take the value of $1/2$ fs^{-1}, which corresponds to a rise time of 7 fs (10-90%), a time scale unachievable for the semi-analytical model if new mechanisms are not implemented to take into account the electronic dynamics. This rise time is an order of magnitude lower than those found in the semi-analytical model, just as the experimental broadening in frequency is an order of magnitude above the original bandwidth.

4.4 Four wave mixing, a window into time-varying effects

4.4.1 Four wave mixing in the Indium Tin Oxide bilayer

The matter remains that the frequencies generated by the modulation remain weak in amplitude in comparison to the main peak of the probe spectrum. To obtain a purely time-varying signal,

it is necessary to cut out the portion of the probe pulse that experiences little modulation by the pump. If the probe is 225 fs long in time and the modulation 7 fs, 97% of the pulse sees little modulation. A first portion of the pulse arrives before the rise, does not see any time-varying effects and is little reflected. A second portion arrives after the rise of the modulation and sees weak time-varying effects due to the slow recovery time of the mirror, and constitutes a majority of the signal due to the increase in reflectivity as shown in Fig. 4.7(a).

A useful measurement would record a signal that is present only during the modulation, bearing only the mark of the time-varying effects. An example of such a measurement can be found in Bruno et al.'s work [69], where the negative refracted and phase conjugated signals, generated during modulation and separable from reflected and transmitted signals, were recorded at slightly negative delays and showed time refraction in their spectra. The simultaneous presence of the probe and pump generated both the signal and the time-varying signature in its spectrum, as illustrated in Fig. 4.7(b). As negative refraction and phase conjugation originate from four wave mixing (FWM), we take inspiration from these measurements by exploring the ITO's rise time dynamics through the lens of FWM between the pump and the probe.

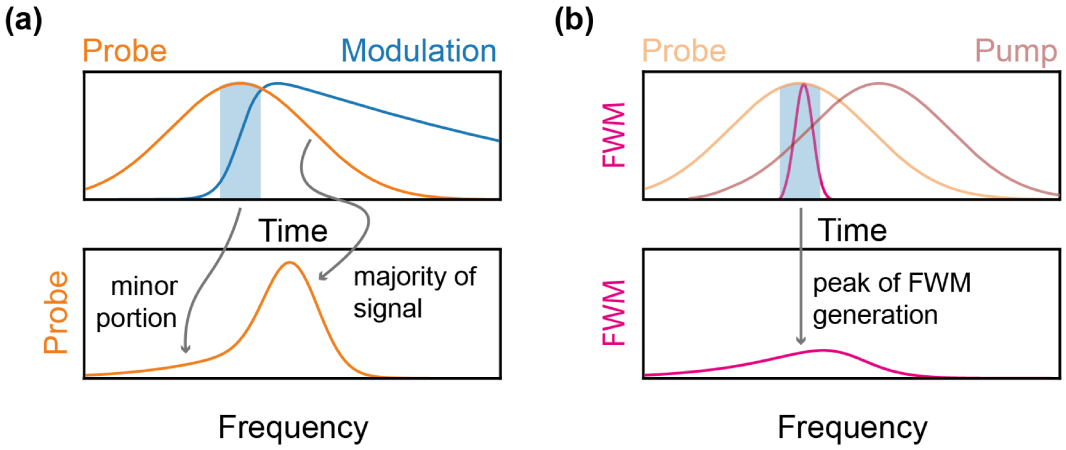

Figure 4.7: Motivation for the FWM experiment. **(a,b)** Diagrams of the impact of the pump and probe field dynamics along the modulation and their role in the generation of frequencies in (a) the probe spectrum and (b) the FWM spectrum. (a) The probe (orange curve) peaks on the rise of the reflectivity modulation (blue curve) in time (top). Yet, as the rise time is short only a small portion of the probe pulse is modulated (blue area). This results in the majority of the probe spectrum being unaffected (bottom). (b) On the other hand FWM (pink curve) exists only when pump (red curve) and probe (orange curve) are in the medium at the same time, which corresponds to the rise of the modulation (blue area, top). As a result, a major portion of the FWM pulse is modulated, generating a broad spectrum (bottom).

FWM is a third-order nonlinear parametric process, corresponding to the scattering of three waves generating a fourth one. In our scenario, the scattering of two pump photons with

a probe photon, as shown in Fig. 4.8(a), leads to the generation of a fourth photon with a new frequency and propagation direction. This nonlinear process is strongly dependent on the pump and probe intensities as

$$E_{FWM} \propto \chi^{(3)} E_{pump}^2 E_{probe}^{\dagger} \tag{4.3}$$

where E_{FWM} is the generated FWM field and E_{pump} and $E_{probe}^{\dagger}$ the respective pump and conjugated probe fields within the medium. Strong FWM signal will only be generated at the time of highest overlap of the two beams in the medium, as desired. As shown in Fig. 4.7(b), this time coincides with the rise time of the reflectivity modulation. At earlier times, the pump is not present in the medium, and at later times the rise of reflectivity prevents both pump and probe from entering the nonlinear medium as light is reflected at the interface, preventing the generation of FWM. Then, the major portion of the FWM pulse experiences the rise of the modulation, and the signal is expected to bear a similar time-varying signature in its spectrum as in section 4.3.

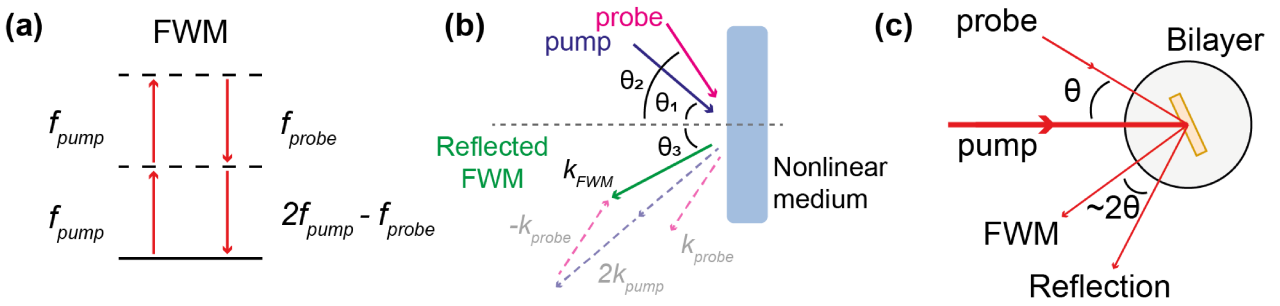

Figure 4.8: The FWM experiment. **(a)** Transition diagram for the FWM process. Dashed lines represent virtual states and dark lines real states within the medium. **(b)** Conservation of momentum and angle in the FWM process. For degenerate FWM with two pump photons impinging at an angle θ_1 and a probe photon at θ_2 on a nonlinear medium, conservation of momentum allows prediction of the out-coupled FWM angle θ_3. **(c)** Updated measurement setup, with simultaneous measurement of FWM and reflection of the probe. The FWM detector is placed 20 degrees away from the probe, at a lower out-coupling angle.

FWM is a nonlinear process that conserves energy and momentum. In our experiment, pump and probe photons have the same energy - we refer in this case to degenerate FWM - which means the generated photons will have the same frequency ω as the input signals (see Fig. 4.8(a)). Yet, thanks to conservation of momentum, FWM can be separated spatially from pump and probe as shown in Fig. 4.8(b), as these are not co-linear. For two degenerate beams impinging on a medium at angles θ_1 and θ_2, with respectively two and one photons contributing in this manner, the output FWM can be predicted to come out at the angle θ_3 following:

$$\tan(\theta_3) = \frac{2\cos(\theta_1) - \cos(\theta_2)}{2\sin(\theta_1) - \sin(\theta_2)} \tag{4.4}$$

In our setup $\theta_1 = 55°$ and $\theta_2 = 65°$, as a result $\theta_3 = 44.7°$. This means the FWM signal is $\sim 2\theta$ away from the probe inwards, where θ is the angle difference between the pump and the probe.

For this reason, the collection setup is improved by adding a collection line for FWM at this angle, 20 degrees below the probe collection angle as illustrated in Fig. 4.8(c). Though FWM could be more efficiently recorded in a different configuration than reflectivity (see appendix A), for the sake of comparison between the FWM signal and the modulated probe, the carrier frequency and incidence angles will be kept to 230 THz and 65 degrees for the coming measurements. This will not affect our interpretation and understanding of the dynamics in the medium as the measurement of FWM is only used as a window into the time-varying effects in ITO.

4.4.2 Spectral broadening in four wave mixing

We characterise the time-varying signature of the single slit in time in the bilayer by measuring FWM spectra at various pump intensities in Fig. 4.9(a). Our previous assumptions on the underlying time-modulated signal are confirmed: the FWM spectrum goes from a bandwidth scale comparable to the original pump and probe pulse, with a Gaussian shape, to a very broad non-Gaussian distribution and saturates in bandwidth for the same pump intensities as reflectivity. These spectra are taken at a delay of -150 fs, where FWM signal is the highest as is shown in Fig. 4.9(b), in which FWM (continuous red curve) and reflectivity (blue curve) are measured simultaneously. This is confirmed by the semi-analytical theory from section 2.3.2 (dashed red curve): though it cannot accurately depict modulation speeds, the model computes with high accuracy the pump and probe field in the layer with time, which allows to estimate the outgoing FWM as a function of delay.

The FWM bandwidth (FWHM) as a function of pump intensity are extracted and shown in Fig. 4.9(c). At a low pump intensity of 15 GW/cm^2, the FWM bandwidth is 3.2 THz, close to the original pump-probe width of 2.8 THz. The slight broadening is partly due to the FWM process, which mixes the various frequencies within the two signals, and partly due to the weak time-varying effects at low intensity. The width then increases with intensity and saturates above 100 GW/cm^2, with a plateau near the maximum recorded value of 10.7 THz. The peak of the FWM signal is also redshifted by 3.8 THz with regards to the probe pulse. This shows the true strength of the time-varying effects in the ITO bilayer, with a vast range of generated

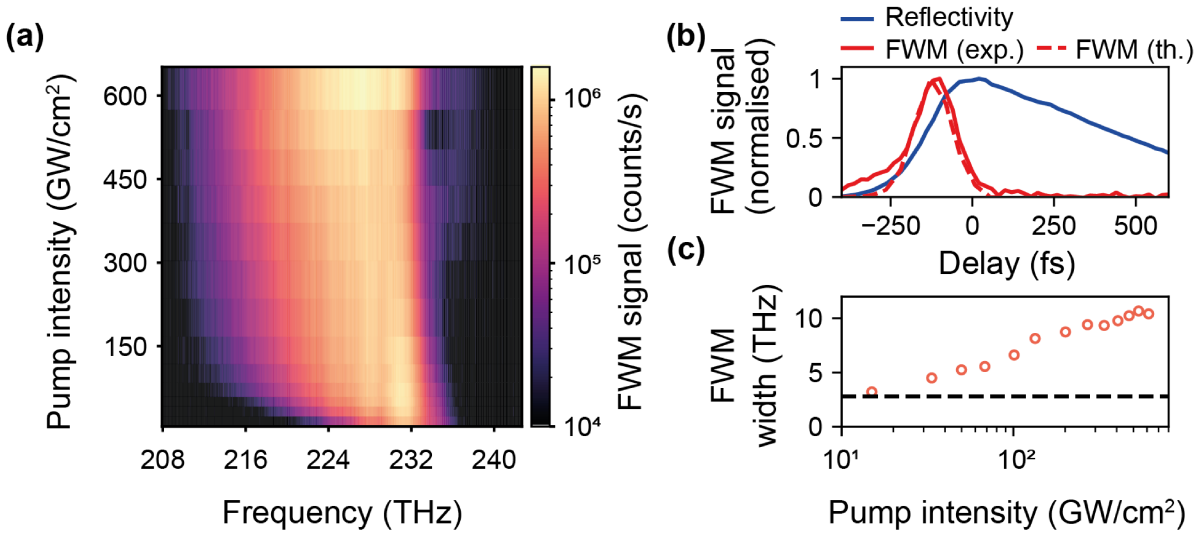

Figure 4.9: Time-varying signature in FWM. **(a)** FWM spectrum against pump intensity, measured at the delay with maximum signal. The probe is kept at 1.4 GW/cm^2, for a frequency of 230 THz and an incidence angle of 65 degrees. **(b)** FWM signal as a function of delay (continuous red curve) against the simultaneously measured modulation of reflectivity (blue curve). The adiabatic model (red dashed curve) can predict the evolution of FWM with delay with high accuracy. **(c)** Measured FWM bandwidth (FWHM) against pump intensity. The black dashed line shows the width of the illuminating probe signal. Reproduced from [79].

frequencies hidden underneath an unmodulated main peak in the reflected probe spectrum, and the values obtained here match well with the observed broadening in the reflection signal shown in Fig. 4.4(a).

Having observed a bandwidth increase by a factor of 3.8 implies a rise time value of 30 fs. This is larger than the value of 7 fs found by fitting the probe spectra with Fourier theory, but this can be explained by the fact that the broadening from time-varying effects is smeared by the complexities of the FWM process, hence the value of 30 fs should be considered as an upper limit rather than an actual value.

4.5 An anti-slit in a 310 nm Indium Tin Oxide thin film

4.5.1 Indium Tin Oxide transition from metal to dielectric: making an anti-slit

To put to test the time-varying physics uncovered so far, we perform the single slit diffraction experiment in a different system and configuration. An ITO thin film with a thickness of 310 nm, larger than that of the bilayer at 40 nm, is studied with pump-probe experiments to characterise how a change in the system's coupling and propagation properties, while maintaining the same nonlinear optical properties, affects the spectral modulation from a single slit. The 310 nm ITO

sample is very similar in many aspects to the bilayer, if not for the following few differences.

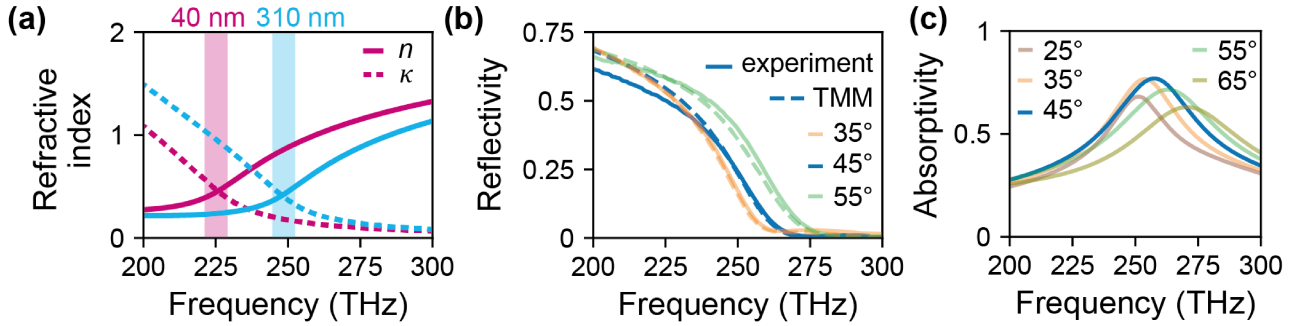

Figure 4.10: Linear characterisation of the 310 nm ITO sample. **(a)** Real (continuous curves) and imaginary (dashed curves) refractive indices of the 40 nm (pink curves) and 310 nm (light blue curves) ITO layers as a function of frequency. **(b)** Linear reflectivity of the thin film as a function of frequency, measured (continuous curves) and as computed by TMM (dashed curves), for angles of 35 (orange), 45 (blue) and 55 (green) degrees. **(c)** Corresponding absorption spectra from TMM, with the added angles of 25 (brown) and 65 (dark green) degrees for comparison.

First, as explained in section 2.2.2, the ENZ frequency of ITO is dependent on the fabrication process and particularly on the thickness of the fabricated sample. In our fabrication process, a thicker sample will have a higher plasma frequency, and as a result the 310 nm ITO sample has its ENZ frequency at 248 THz (1211 nm) as measured with ellipsometry in Fig. 4.10(a), whereas the bilayer had an ENZ frequency of 227 THz (1320 nm). As a result the Berreman resonance will be shifted to higher frequencies.

A second consequence of the larger thickness of the sample is a change in the strength and shape of the Berreman resonance: for thicker films of ITO, the ENZ crossing comes back to the more regular metal to dielectric transition of a bulk material, where the material is reflective at lower frequencies (metal) and transparent at higher frequencies (dielectric). To verify this, the reflectivity of the 310 nm sample is measured in the same configuration as depicted in the previous chapter in Fig. 3.2(a) and compared to TMM predictions. The reflectivity for p-polarised light for a few probe incidence angles is shown in Fig. 4.10(b): the Berreman resonance is now highly asymmetric, with a very minor bump in reflectivity at higher frequencies for an incident angle of 45 degrees. The presence of the Berreman resonance is not evident from the reflectivity profile, but appears much more clearly in the spectral and angular dependence of absorptivity: the angle of 45 degrees exhibits the strongest peak in absorption in Fig. 4.10(c). Going back to reflectivity, once again, for frequencies above the Berreman resonant frequency of 258 THz, no contrast is to be expected from intraband optical transitions as the material stays transparent throughout the modulation process. On the other hand, frequencies below 258 THz will undergo a metal to dielectric transition, showing a strong decrease in reflectivity.

This means optical pumping of the medium will create an anti-slit, where the aperture function goes from an ON to an OFF state rather than the opposite as in a regular slit. For this reason, no back-reflecting gold layer is added.

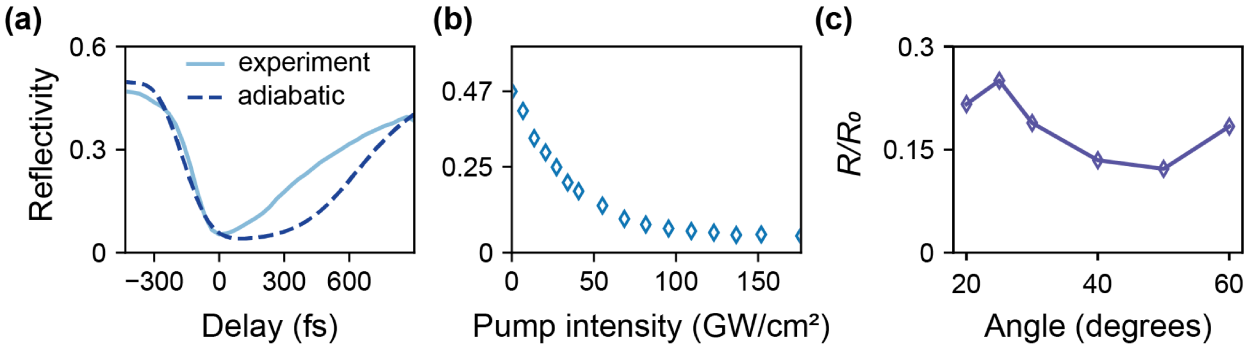

Figure 4.11: Pump probe characterisation of the 310 nm ITO sample. **(a)** Reflectivity as a function of delay for a 230 THz probe incident at 45 degrees with a pump intensity of 174 GW/cm^2. The adiabatic model (dark blue) fits well with the measured reflectivity (light blue). **(b)** Pump intensity dependence of the maximum change in reflectivity for a carrier frequency of 230 THz and a probe angle of 45 degrees. **(c)** Relative change in reflectivity (maximum modulation over unmodulated reflectivity R/R_0) as a function of probe incidence angle.

The anti-slit is measured and displayed in light blue in Fig. 4.11(a) for a pump-probe pulse at 230 THz, for consistency with the bilayer, and at an incident angle of 45 degrees. The reflectivity for the static system is of 46.9%, but at zero delay falls down to 5.3%. The observed time scales are the same as in the bilayer, as the pulses and modulations mechanics are the same. In fact, the modulation with delay can be accurately predicted using the semi-analytical model from section 2.3.2 (dark blue curve), keeping the same parameter α dictating the dependence of the plasma frequency on the field intensity within the medium, but accounting for the new ITO permittivity of the 310 nm thin film.

The 310 nm ITO thin film and the 40 nm bilayer have many properties in common. The pump intensity dependence of the modulation, shown in Fig. 4.11(b), shows a similar behaviour than for the bilayer, with a similar saturation level of $\sim$ 100 GW/cm^2, except for the decrease rather than increase in reflectivity. With regards to probe incidence angle, measurements in Fig. 4.11(c) (blue curve) show a better performance for angles of 45-50 degrees.

4.5.2 Time refraction and diffraction in an anti-slit experiment

Moving back to time-varying effects, we aim to compare the spectral evolution of the probe with delay for the two samples, 310 nm ITO and the bilayer, and compare the anti-slit and the slit modulation. Such a scan is shown on a logarithmic scale for a probe frequency of 230 THz, intensity of 176 GW/cm^2, and incidence angle of 45 degrees in Fig. 4.12(a) for the 310 nm ITO

thin film. The features are very similar to those observed in Fig. 4.1(a), with a thinning of the spectrum at zero delay preceded by a broadening, with stronger effects on the red side of the spectrum. The generated spectrum is quite broad at slightly negative delay. Yet, because of its thickness, the 310 nm ITO is more susceptible to phase accumulation effects than the bilayer, and it is therefore harder to distinguish between the effects of time refraction and time diffraction, and the validity of the semi-analytical model can be questioned as it assumes a single interface in space.

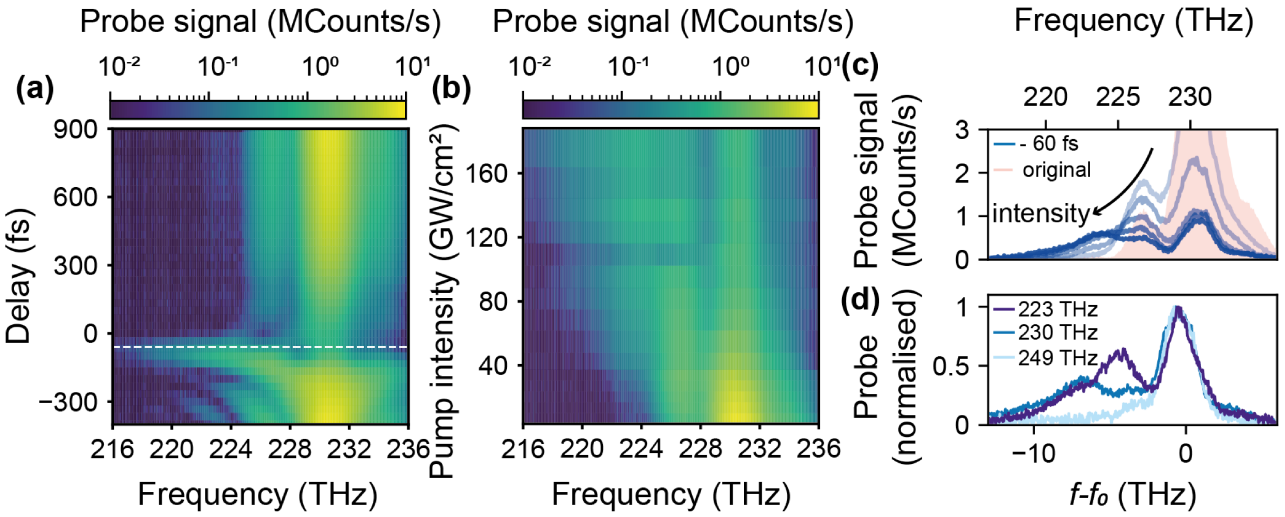

Figure 4.12: Spectral modulation in the 310 nm ITO thin film. **(a)** Measured probe spectrum on a logarithmic scale against delay for a pump intensity of 176 GW/cm^2, incidence angle of 45 degrees and 230 THz carrier frequency. The white dashed line shows the delay at which the spectra in panels (c) and (d) are shown. **(b)** Corresponding probe spectrum at -60 fs delay against pump intensity. **(c)** Modulated (−60 fs, blue curves) against unmodulated (red shaded area) probe spectrum extracted from panel (b). The amplitudes decrease with increasing pump intensities (light blue to dark blue curves), with intensities of 33, 55, 95, 123 and 151 GW/cm^2. **(d)** Modulated spectrum at −60 fs delay for a pump intensity of 152 GW/cm^2, for various carrier frequencies.

To better distinguish between the two effects, the modulated spectrum, at a delay of -60 fs, is measured for a range of pump intensities and represented in Fig. 4.12(b). There, the transition between the unmodulated and modulated spectra is clearer, and it is easier to link various attributes. As the pump intensity increases, the contrast between the main peak and the higher frequency side of the spectrum decreases, while a rift at 228 THz becomes more and more visible. This suggests that shift and broadening could be happening simultaneously, with the modulated peak crossing this rift at low intensities - explaining why the later appears at high intensity - and is broadened to a wider extent. The modulated spectra at various intensities are shown in Fig. 4.12(c) in blue, alongside the original, unmodulated spectrum (shaded area). The modulated peak is showing finer features, with two sub-peaks at high intensities within a

broad range of frequencies. The new spectral features exhibit an overall shift of the scale of 6 to 8 THz, significantly away from the original peak at 230 THz.

Note that the unmodulated spectrum does exhibit a low amplitude 'bump' at lower frequencies, which indicates a deviation from a classic Gaussian spectrum and perturbs the modulation. It seems as if this bump, due to its lower frequency, is conserved and gains more prominence while the main peak is being suppressed by the reflectivity decrease, and ends up polluting the measured modulated signal. Of the two peaks at lower frequency, one could be due to time-modulation while the other may just be a limitation in the experiment due to the imperfections in the unmodulated spectrum; this is problematic as it makes it hard to gain information from the frequency shifted peak. A possible explanation would be for this 'bump' to arrive at a slightly different time than the carrier, thus not being suppressed when the main peak is but rather at an earlier stage, explaining its temporary suppression at zero delay in Fig. 4.12(a). Further experiments would be required to test these points, nevertheless, we can see here the time-varying spectrum is likely showing strong time refraction with a 6.84 THz shift at a high intensity of 176 GW/cm^2.

Another problem to settle in the anti-slit is the question of absolute change in reflectivity $R_{mod} - R_0$ against relative change R_{mod}/R_0. On one hand, lower frequencies have the potential to see a higher absolute change in reflectivity $R_{mod} - R_0$, but on the other hand the higher absorption near the Berreman frequency give higher frequencies the potential to be further modulated. This is experimentally investigated by measuring the modulated spectra at various frequencies, here shown in Fig. 4.12(d) for a constant illumination intensity of 152 GW/cm^2. The spectra are normalised and shifted respective to their original carrier frequency for superposition. As can be seen, the lower frequencies exhibit a stronger modulated spectrum than the higher frequencies. Larger time-varying effects from a higher contrast in modulation is to be expected from Fourier theory. Moreover, this shows that in practice, in configurations where there is plenty available pump intensity for use in the experiment, ideal coupling to the medium is not necessary and it is more important for the probe to be in the right configuration.

Having experimentally characterised the anti-slit in 310 nm ITO, the spectral distribution of the probe pulse, with a perturbation in the form of a bump at red frequencies, is now known to be problematic in the measurement of time-varying effects in the thicker layer of ITO. To get around this constraint, one could use the semi-analytical model to find out what the time-varying effects should look like in the absence of chirp or perturbations and see if it matches with experimental observations where these are varied.

The experimental and simulated scans are compared side by side in Fig. 4.13(a) and (b).

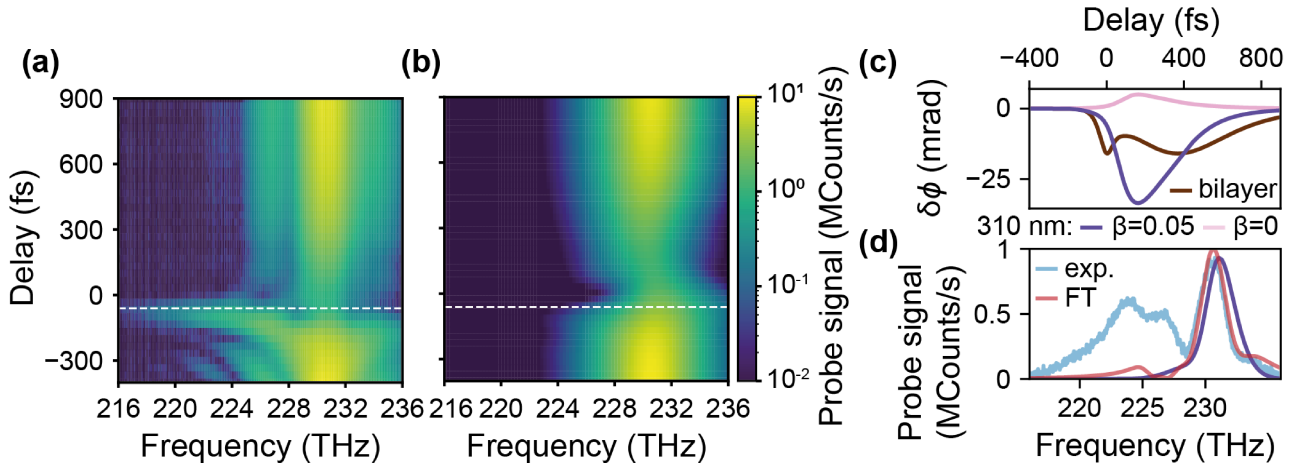

Figure 4.13: Theoretical modelling of the anti-slit in the 310 nm ITO thin film. **(a)** Experimental signal against frequency and delay, as presented in Fig. 4.12(a). **(b)** Theoretical prediction using the semi-analytical model, with an added change in electron scattering. The white dashed lines show the delay at which the spectra in panel (d) are shown. **(c)** Modelled phase change of the complex reflection coefficient as a function of delay as modelled for the 310 nm ITO with and without a change in electron scattering rate (respectively dark blue and pink curves), with the modelled phase change of the bilayer in the absence of electron scattering modulation for comparison (brown curve). **(d)** Probe spectra at -60 fs delay: experiment (light blue curve) against the semi analytical model in the presence of electron scattering modulation (dark blue curve) and the Fourier model (red curve).

One can see the theoretical prediction, though it follows the expected shift and broadening trend, extends to a much narrower range of frequencies than the experiment. The prediction shown in Fig. 4.13(b) results from a slightly tweaked model in comparison to that used for the bilayer. When modelling the anti-slit with a change in plasma frequency only, that is $\alpha \neq 0$, Fig. 4.13(a) cannot be replicated. This is likely due to the difference in sample geometry, with the added transmission and propagation within the layer. Whereas the bilayer's reflectivity increased under modulation, preventing the probe pulse from propagating within the medium, the 310 nm ITO instead becomes transparent with very little reflection, meaning that reflected light doesn't come from the first air/ITO interface anymore. Then, the role of absorption and phase changes during propagation becomes important in the 310 nm ITO where it had little impact for the bilayer. In comparison, the role of phase accumulation in the bilayer is overestimated by the model (see Fig. 4.1(c)).

To account for this phase shift, we come back on our decision not to include changes in the electron scattering rate γ in the Drude model, responsible for absorption and losses in the permittivity. It is known that γ sees a larger relative change under optical pumping than the plasma frequency [58], but this change was consciously ignored when modelling the bilayer as it introduced an extra fitting variable without bringing new time-varying dynamics into play due

to the nature of the sample. As can be seen in Fig. 4.13(c), the phase change in the absence of change in γ in the 310 nm ITO sample, here in pink, is negligible in comparison to the bilayer, shown in dark brown. By adding a change in the electron scattering rate, modelled as

$$\gamma(t) = (1 + \beta \times I)\,\gamma_0 \tag{4.5}$$

where I is the illuminating intensity and $\beta = 0.05$ cm^2/GW a fitted coefficient, the newly obtained phase change in dark blue in Fig. 4.13(c) brings the simulation closer to the time-varying dynamics measured in the sample. Yet, as the spectra at negative delay in Fig. 4.13(d) show, the modelled spectrum (dark blue curve) is still far off from the recorded modulated spectrum (light blue). This is verified at various pump intensities, low to high, showing that the semi-analytical model is limited in modelling the anti-slit in the 310 nm ITO. The Fourier model, as presented in equation 2.13 is also presented in red in Fig. 4.13(d), also cannot reproduce the experiment any better than the semi-analytical model, ruling out the shortening of the rise time at high intensity as an explanation for the shortcomings of the modelling.

This could be due to the interface approximation breakdown in the semi-adiabatic model from section 2.3.2, as causality comes into play and cannot be replicated by the model: the field propagating in the medium, as it undergoes broadening and frequency shift at a time t, is not immediately out-coupled, and is consequently modulated and further broadened and shifted at time $t + \delta t$. For the bilayer, the field is being prevented from entering the medium during the rise time and decay of the modulation, so causality is no problem. In the anti-slit, the reflected probe suddenly is allowed to penetrate and propagate within the medium, and likely the modulated signal that is being reflected undergoes round-trips within the medium, hence the problem of causality. This is a reasonable explanation for the limitations of the semi-analytical model in reproducing experimental results. The excellent agreement between experiment and theory in the bilayer at low intensity in Fig. 4.1(a) and (b) shows that experimental chirp or perturbations to the probe's temporal profile is no key mechanism in the generation of new frequencies.

To conclude, time-varying effects were observed and quantified in the 310 nm ITO in the same fashion as in the ITO bilayer, and precious insight was gained on the experimental limitations one might face. Most problematic are the difficulty of replicating the measured data with the model, due to the sample deviating from the interface approximation. Thus, the bilayer will be a better platform to study time diffraction effects.

4.6 Conclusion

In conclusion, spectral diffraction from a single slit in time was recorded from the ITO bilayer acting as an ultrafast mirror. Low intensities result match well with the current understanding and modelling of time-varying effects in ITO, but in the limit of the saturation regime, new frequencies are generated beyond the predicted extent. Further modelling with a material-independent Fourier theory, and measurement of FWM in the sample point towards a reduction of the reflectivity rise time to scales of 10 fs or below. This timescale is unexpectedly faster than those presented or modelled in literature [53, 67]. This will be further tested and explored in the following chapter, as we aim to observe diffraction from a double slit experiment in time. Finally, spectral modulation from an anti-slit in time in a 310 nm ITO thin film was recorded. Though the modulation mechanisms are identical, the different nature of the sample's reflection geometry deviates from the interface regime, thus making the time-varying mirror model inadequate and preventing numerical modelling. This shows the important role of the time-varying mirror for time diffraction in contrast to previously explored ENZ time-varying systems in literature.

Chapter 5

Young's double slit experiment in time

In 1801, Thomas Young demonstrated the wave nature of light using the now famous double slit experiment [88]. Young saw the problems in Newton's corpuscular theory of light in explaining dispersion or other observable optical effects, and was inspired by the then-known nature of sound waves and their beating when interfering. By illuminating two narrow slits separated in space with a light beam, Young was able to observe spatial oscillations due to interference in the intensity of the light reaching a screen placed behind, thus proving the wave nature of light. Since then, double slit diffraction and interferometry have allowed for the exploration of a great variety of wave systems, such as single photons [89], electrons [90, 91], neutrons [29], atoms [92] and large molecules [93]. Temporal double slit diffraction was first predicted by Moshinski in 1952 [34], and has since been observed in matter waves [31–33, 94], and recently in light waves in our work [81]. Though it was proved there is no possible time-domain diffraction of light in vacuum [33], the dispersion of a medium allows for double slit diffraction of photons. We thus design and observe temporal double slit diffraction at optical frequencies, using the ITO platform for diffraction characterised in chapters 3 and 4.

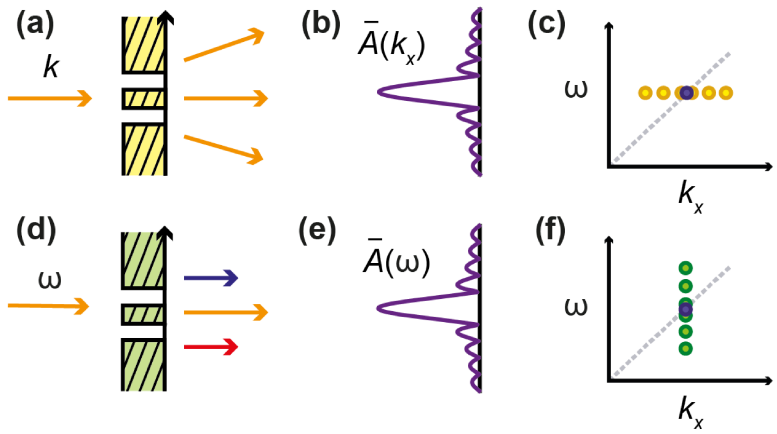

Figure 5.1: A space to time analogy of double slit diffraction. **(a)** Schematic of a spatial double slit experiment: light goes through two separate apertures in space. **(b)** Resulting momentum spectrum from the double slit diffraction, with the interference pattern taking the form of the Fourier transform of the aperture function. **(c)** Horizontal transition corresponding to the double slit aperture modulation of the beam in the dispersion diagram. **(d)** Time-domain double slit experiment: a pulse now goes through two successive apertures in time. **(e)** Resulting frequency spectrum from the time double slit, showing the same interference pattern than in (b). **(f)** Vertical transition in the dispersion diagram due to the temporal double slit modulation. Reproduced from [81]

Going back to the space to time analogy presented in section 2.1.1, we can get information

on time diffraction. In the classical picture, when light impinges on a mask with an aperture function $A(x)$ (Fig. 5.1(a)), in the limit of Fraunhofer diffraction a pattern corresponding to the Fourier transform of the aperture $\bar{A}(k_x)$ can be observed on a distant screen. The maxima and minima of this pattern correspond to constructive and destructive interference between the components with different momenta k_x. The resulting momentum distribution is shown for a double slit in Fig. 5.1(b): the observed pattern corresponds to the product of a sinc shape arising from the single slit diffraction, dictating the envelope shape of the pattern, with sinusoidal oscillations arising from the Fourier transform of the two Dirac deltas representing the two slit's separation in time, dictating the oscillation period. In the dispersion diagram, this corresponds to horizontal transitions as shown in Fig. 5.1(c).

In comparison, light going through two successive slits in time $A(t)$ (Fig. 5.1(d)) will see its frequency content modulated into the interference pattern $\bar{A}(\omega)$ in the same way (Fig. 5.1(e)). The shape of the slits will dictate the envelope of the oscillations in $\bar{A}(\omega)$ while their separation will affect the period of the oscillations just as in spatial diffraction. The double slit interference now corresponds to vertical transitions in the dispersion diagram (see Fig. 5.1(f)). The following chapter will present the realisation of double slit diffraction in time using ENZ thin films.

5.1 Demonstration of temporal double slit diffraction

5.1.1 From single to double slit modulation

The transition from single to double slit diffraction in time is experimentally put in place by adding a 50:50 beam splitter in the pump path, to create a second pump path going towards a delay stage and recombining with the other pump and probe at the sample, as illustrated in Fig. 5.2(a). This way, the separation in time between the two pump arrival times can be controlled, as well as the relative delay of the probe with regards to the pumps. The only difference in setup is the smaller angle between pumps and probe, now of 8 degrees (formerly 10 degrees), with the two pumps symmetric on either side of the probe. For measurement stability purpose the pump and probe beams sizes are slightly increased to guarantee the overlap in space of all beams, which now constrains the pump modulation to lower maximal intensities. But as shown in chapters 3 and 4, the sample's reflectivity saturates well below the high intensity of 700 GW/cm^2 used previously, and the pump intensities of $\sim$ 100 GW/cm^2 used in this chapter are sufficient to obtain a strong contrast in reflectivity modulation.

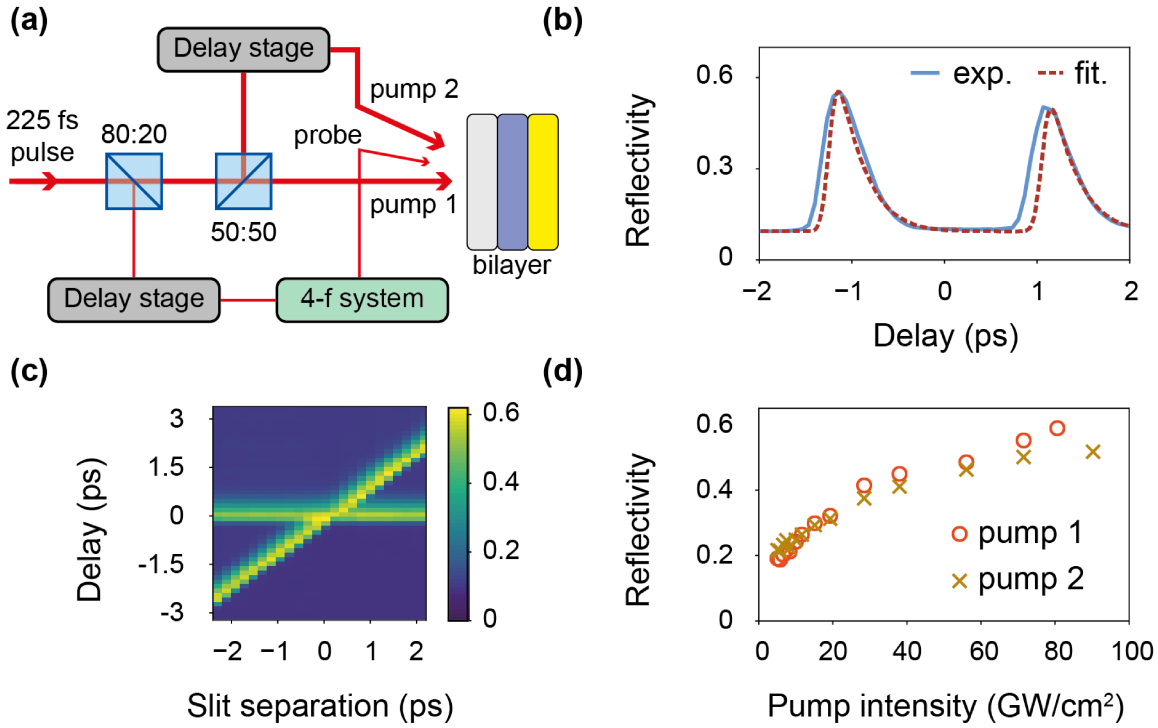

Figure 5.2: Characterisation of the double slit with a short probe pulse. **(a)** Diagram of the double pump-probe setup for double slit diffraction in time. **(b)** Reflectivity as a function of delay for two pumps impinging on the material with a temporal separation of 2.3 ps. The Fourier model (dashed red curve) is fitted to experimental data (continuous blue curve). **(c)** Reflectivity as a function of slit separation and probe delay with regards to pump 1, pump 1 corresponding to the slit at constant zero delay. **(d)** Maximum reflectivity under modulation as a function of pump intensity for pump 1 (orange circles) and pump 2 (dark yellow crosses). Panels (b-d) reproduced from [81]

We first characterise the double slit modulation with a short 225 fs probe pulse, shorter than the slit separation in time, and observe the reflectivity being increased twice as the two pumps arrive successively. The reflectivity as a function of delay is shown in Fig. 5.2(b), and clearly demonstrates the separate action of the pumps arriving with a 2.3 ps delay between them (blue curve). The two pumps having different incidence angles (see Fig. 5.2(a)), they have different coupling to the ITO layer and thus induce slightly different reflection modulation amplitudes.

We verify the control of the slit separation by mapping the reflectivity with delay in Fig. 5.2(c): the pump that we label as 'pump 1' is fixed at zero delay as its arrival time cannot be changed, while the other 'pump 2' arrival time is varied. When the two pumps arrive at the same time, the two slit modulations merge into a single slit in time, with a similar reflectivity level as when the two slits are separated in time due to the saturation of the sample. The saturation of the reflectivity modulation at high pump intensities in Fig. 5.2(d) is evaluated by measuring the maximum reflectivity at various pump intensities, pump 1 and 2 sharing the same intensity level. The shape of the reflectivity curve and amplitude of the modulation are

similar to those measured in chapter 3, though the saturation intensity is slightly lower, which could be due to the different beam sizes used in the present experiment.

We model the double slit in a similar way as the single slit, with the phenomenological model described in equation 2.13 and a real-valued reflection coefficient that we fit to the measured reflectivity. The complete expression for the reflection coefficient modulation is

$$r(t) = A \times r_s\left(t + \frac{S}{2}\right) + B \times r_s\left(t - \frac{S}{2}\right) + C \tag{5.1}$$

where A and B are the respective modulation amplitudes of each slit, S the slit separation in time, and r_s the normalised single slit reflection coefficient as presented in equation 4.1 which we will display here as a reminder:

$$r_s = \frac{1}{(1 + e^{-\alpha t}) \times (1 + e^{\beta t})} \tag{4.1}$$

The model reproduces with good accuracy the rise, slight plateau and decay of reflectivity with delay (see the dashed red curve in Fig. 5.2(b)). The relative amplitude of the second peak B with regards to the first one A, i.e. B/A, is 93%. More importantly, the decay time is fitted to be of 330 fs (1/e), a value compatible with literature [53]. The rise time on the other hand cannot be inferred from this measurement as mentioned previously, due to the temporal resolution limit of the spectrally integrated scan shown in Fig. 5.2(a) corresponding to the probe pulse width of 225 fs.

A last consideration before attempting to measure a temporal diffraction spectrum is the duration of the probe pulse. If the pulse was to be kept at a FWHM of 225 fs, it could not experience the two successive slits modulation as their separation in time would be longer. In order for the probe to experience the double slit in time, it needs to be broadened in time. We use for this purpose the 4-f setup presented in chapter 3. This presents us with a compromise: a longer probe pulse length trades off a lower modulation efficiency (a smaller portion of the pulse is being modulated) with a larger range of observable slit separations. Having taken this into consideration, we can move on to measure and characterise double slit diffraction in the bilayer.

5.1.2 Double slit diffraction

To demonstrate time diffraction, we use a 230 THz probe pulse with a 1 THz bandwidth and a duration of 794 fs, and measure its reflected spectrum under modulation by the two pumps.

The probe is centered to the middle time between the two pump modulations of reflectivity. Fig. 5.3(a) and (b) shows in red the lower side band of the reflected probe spectrum for slit separations of 800 fs and 500 fs. The spectrum is considerably broadened with new frequencies being visible up to 8 THz (or 8 bandwidths) away from the pulse carrier frequency. More remarkably, the spectrum displays oscillations with a specific period, which is lower for a 800 fs slit separation (Fig. 5.3(a)) with a 1.3 THz period than for the lower separation of 500 fs with a period of 2 THz (Fig. 5.3(b)). The oscillations intensity is lower for frequencies further away from the carrier frequency. This distinct signature is very similar in pattern to what is expected in the spatial case, and is in remarkable agreement with predictions from the phenomenological Fourier model (purple line in Fig. 5.3(a) and (b)) from equation 5.1. The envelope intensity decrease with frequency arises from the shape of the single slit modulation, while the underlying oscillations are a direct result of the presence of two separate slits in time.

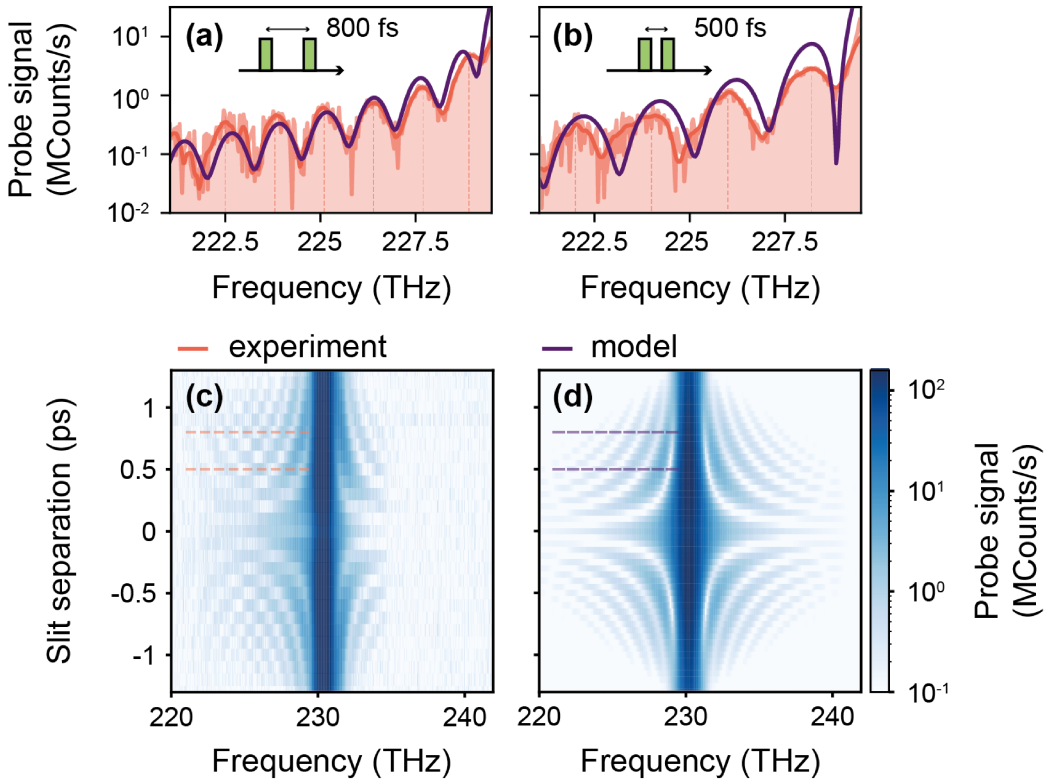

Figure 5.3: Double slit time diffraction spectra and interferograms. **(a,b)** Diffraction spectra for slit separations in time of (a) 800 fs and (b) 500 fs. Experimental data is shown in red (light red curve unprocessed data, dark red curve smoothed data) and theory in purple. **(c,d)** Full interferogram of reflected probe signal against frequency and slit separation in time, (c) experiment and (d) theory. The dashed lines show the line cut which panels (a) and (b) are showing. Reproduced from [81]

The full interferogram of time diffraction is shown in Fig. 5.3(c). As expected from Fourier theory, we observe the oscillation period in spectrum decreasing with increasing slit separation. For large slit separations, the pattern disappears as the probe is not long enough in time to

undergo modulation by the two slits. For low slit separations, due to the reflectivity modulation's finite width, the two slits merge as shown previously in Fig. 5.2(b), which results in the disappearance of the oscillations - the broadening is still visible, as it is a signature of the single slit diffraction. The Fourier model reproduces all these features with good accuracy as can be seen in Fig. 5.3(d). A more noticeable feature of the experimental interferogram that is not being reproduced by the model is the asymmetry in modulation: it shows a considerably larger extent of diffraction on the red side of the spectrum, with a visible range 3 times larger than on the blue side band. This asymmetry is explained by the role of dispersion and phase change in the complex reflection coefficient, which causes a red shift of frequencies through time refraction. The phenomenological Fourier theory doesn't account for phase changes as this would need to be measured in an interferometric experiment in order to guide the modelling, just as reflectivity measurements guided the modelling of amplitude. This will be further discussed in section 5.2.2.

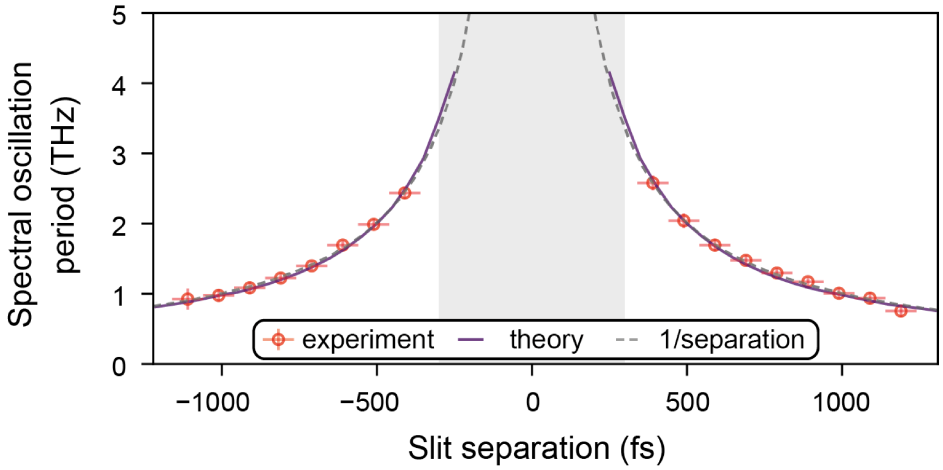

Figure 5.4: Spectral oscillation period from double slit time diffraction. Measured oscillation period in the spectrum diffraction pattern as a function of slit separation in time: the experimental values (red circles) are in excellent agreement with the phenomenological model (purple line) and follow an inverse rule with the slit separation in time (grey dashed line) as expected from Fourier theory. The errors are standard deviation in slit separation and standard error of the mean in spectral oscillation period. The grey-shaded area shows slit separations of less than 300 fs, where the slits are too close in time to produce a double slit pattern. Reproduced from [81].

A final piece of evidence in the demonstration of double slit time diffraction happening in the bilayer is the dependence of the spectral oscillations' period on the slit separation in time, shown in Fig. 5.4. In spatial diffraction theory, under the Fraunhofer approximation, the distance between two peaks in intensity is inversely proportional to the distance between the slits. As a similar relation can be expected for the temporal case, we extract the spectral oscillation period from the interferogram shown in Fig. 5.3(c), and plot it against slit separation

in Fig. 5.4. The agreement between experiment and the Fourier theory from equation 2.13 is again remarkable and shows the signature of time diffraction. The period's dependence on the slit separation is symmetric with regards to exchanging the two pumps in time as expected, while the smaller slit separations (below 300 fs) show no visible oscillations due to the slits merging into a single one. The errors are shown as the standard deviation estimated for the slit separation error (50 fs), and the standard error of the mean for the spectral oscillation period (an estimated error of 0.15 THz on the oscillation peak location, the statistics arising from the variable number of observable oscillations).

Hence, we have convincingly demonstrated diffraction from a double slit in time, by recording its signature spectral oscillations and their dependence on the slit separation in time. This experiment provides a simple and elegant view into the physics of time-varying media as well as a useful formalism for spectral shaping of pulses.

5.2 Analysis of diffraction patterns

5.2.1 Experimental insights

We will here further look into the effects of slit separation, pump intensity and probe offset in time on the spectral interference pattern arising from the double slit in time. For this, we define two figures of merit for double slit diffraction drawing inspiration from the spatial experiment. The first figure of merit is visibility and is defined as

$$\nu = \frac{C_m^{max} - C_m^{min}}{C_m^{max} + C_m^{min}} \tag{5.2}$$

where C_m^{max} and C_m^{min} refer to the maximum and the next minimum of the diffraction peak of order m. We will pick $m = 1$ here. Visibility, just as in its name, informs on how visible the individual oscillations from the slits are as illustrated in Fig. 5.5(a).

As can be seen in Fig. 5.5(b), the visibility of the interference fringes increases as the slit separation in time decreases. This is consistent with predictions from the Fourier model that was presented in 2.3.1, up to the merging of the two slits together. There, the oscillations are drowned under the broadening of the probe pulse, which reduces the experimental visibility.

To understand this, one needs to look into the probe pulse shape in Fig. 5.5(c). As it is Gaussian in time, its amplitude is smaller away from the center, and thus the two slits, when arriving further away from the probe's center, affect a smaller portion of the probe field. As a result the interference is weaker, resulting in lower visibility. On the other hand, for an

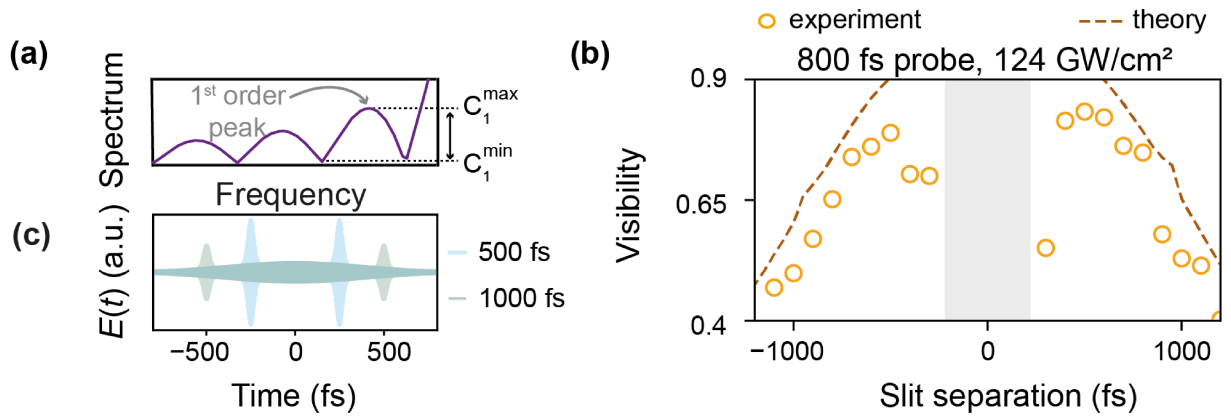

Figure 5.5: Interferometric visibility and slit separation in time. **(a)** Diagram of the interferometric visibility as defined by the frequency spectrum. **(b)** Measured visibility as a function of slit separation for a 794 fs FWHM probe and a 124 GW/cm^2 pump intensity. The theoretical prediction from the Fourier model is shown with the dashed brown curve. **(c)** Sketch of the reflected probe field in time for slit separations of 500 (light blue area) and 1000 fs (light green area). The turquoise area shows the original probe pulse before modulation.

infinitely long probe pulse in time, visibility would be constant with slit separation. This can be considered the temporal equivalent of using too large or too small of a beam fitting in the space between two slits, with all or little light passing through and interfering.

The second figure of merit, efficiency, will be defined as the ratio between the maximum intensity of the non-diffracted spectrum C_0, and the first diffracted peak $C_{m=1}^{max}$ where m is the diffraction order, i.e. $\eta = C_{m=1}^{max}/C_0$ as illustrated in Fig. 5.6(a). This gives a measure of the relative intensity of the diffracted signal, as well as puts a higher limit on the number of observable fringes for a given detection apparatus, due to saturation and damage of the sensor that can arise from the high counts of the main carrier frequency when modulated. Note that this definition of efficiency is not meant to describe an absolute strength of the frequency generation effect, as the diffraction order signal could alternatively be normalised to the modulated peak or the peak intensity before reflection, which would give 10 times lower values.

Efficiency is expected to increase with the single slit modulation amplitude, as the envelope of the spectrum depends on it. We choose here the diffraction order $m = 1$ for lower frequencies, on the red side of the spectrum as in Fig. 5.6(a). Fig. 5.6(b) shows how the contrast between the modulated and unmodulated probe pulse in time decreases with a lower modulation amplitude, for instance as a consequence of a lower pump intensity. The efficiency of the modulation depends strongly on the pump intensity as a higher slit contrast will lead to a larger broadening and thus a higher amplitude of the frequency oscillations.

The double slit diffraction spectrum is recorded for various pump intensities and shown in

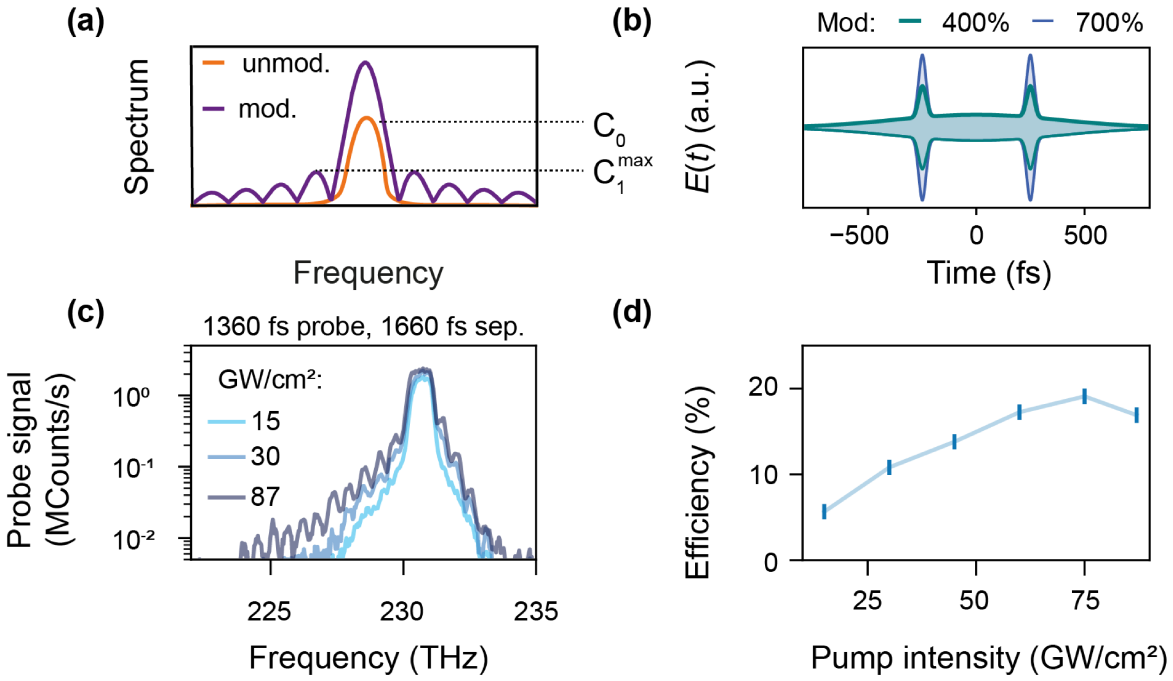

Figure 5.6: Pump intensity dependence of double slit diffraction efficiency. **(a)** Diagram of the modulated (purple curve) and unmodulated (orange curve) spectra defining efficiency. **(b)** Sketch of the reflected probe field in time for slit modulation amplitudes of 400% (green curve) and 700 % (blue curve). **(c)** Interference spectra for various pump intensities, for a 1360 fs probe and 1660 fs separation. **(d)** Corresponding efficiency as a function of pump intensity.

Fig. 5.6(c). As intensity decreases, one can observe the reduction in broadening and thus intensity of the oscillations, as the single slit modulation weakens. At 15 GW/cm^2, the oscillations are not visible, while at 30 GW/cm^2 they decay significantly faster than at 87 GW/cm^2, while their amplitude is comparable to the noise of the detector. The efficiency is then extracted for a range of pump intensities. Fig 5.6(d) indicates that this behaviour saturates at high intensity, just as the modulation of reflectivity, thus putting a higher limit of $\sim$ 20% on the maximum achievable efficiency for the experimental conditions.

However, changing the intensity of the pump illumination has no measurable effect on the visibility of the oscillations. This is not obvious from Fig. 5.6(c), where the interference spectra for a 1360 fs probe and a 1660 fs slit separation are shown for intensities of 15 to 87 GW/cm^2, but is to be expected from Fourier theory. When decreasing the modulation amplitude, it is the envelope of the oscillations, corresponding to the single slit shape and the broadening of the spectrum, that decreases. Visibility is dependent on the slit separation, slit shape and the probe properties and thus remains the same.

Another mechanism that can be leveraged to tune the diffraction spectrum is the temporal offset of the probe with regards to the two slits. If the slits peak at times $-S/2$ and $S/2$, we can define the offset as the time between $t = 0$ and the time t_{max} corresponding to the maximum of

the probe pulse in time (Fig. 5.7(a)). Again from Fourier theory, we expect the oscillations to lose visibility as the probe is offset from the time $t = 0$, as it progressively sees more and more of a single slit while the other slit acts less and less on the modulation. On the other hand, the probe pulse peak coinciding with the maximum of a modulation induces a larger broadening and higher signal.

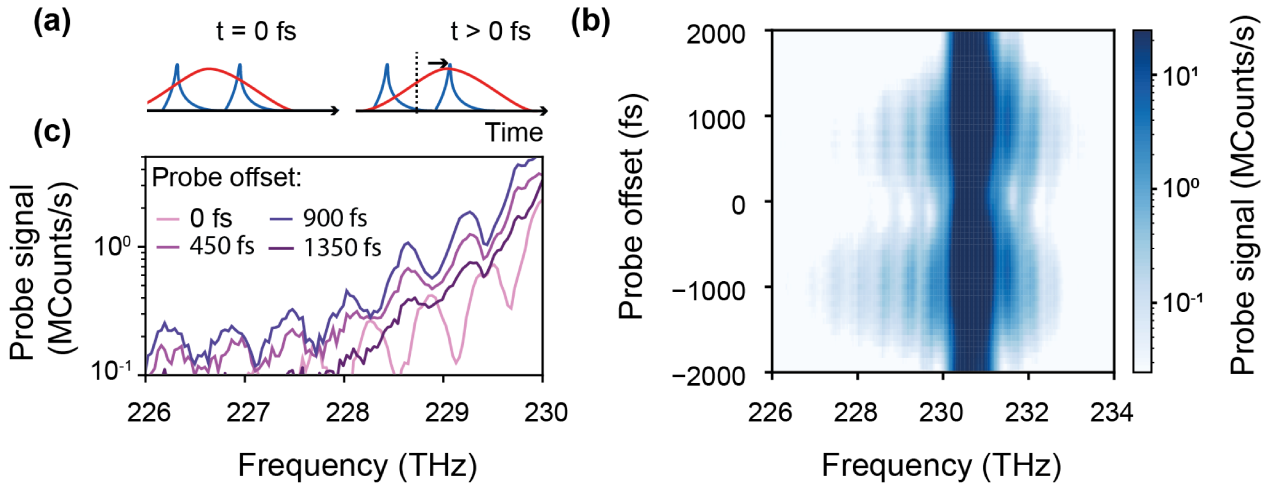

Figure 5.7: Spectral oscillation dependence on the probe offset in time. **(a)** Diagram of probe offset in time: the probe is originally set at the intermediate time between the two modulation peaks (left), but can be displaced to arrive earlier or later in time (right), thus observing one slit more than the other. **(b)** Measured probe spectra as a function of probe offset, for a 1363 fs probe. **(c)** Line cut of the probe spectrum for probe offsets of 0, 450, 900 and 1350 fs (from light pink to dark purple). Panel (a) reproduced from [81].

This is measured in Fig. 5.7(b) by varying the probe arrival time via the delay stage while keeping the slit separation in time constant. As the probe moves away from the zero offset, the spectral broadening gets stronger as the pulse experiences more modulation from one of the two slits, while the effect of the other slit gets weaker. The broadening is strongest for offsets of ± 1000 fs, corresponding the probe pulse peaking on the rise time of one of the slits. Interestingly, the oscillations in the spectrum are visible for a wide range of probe offsets. Focusing on the spectra for a few selected probe offsets in Fig. 5.7(c), it appears that the visibility of the interference fringes decreases as their intensity increases (pink to purple curves). On one end, the imbalance between the two slits decreases the visibility, while the prominence of a single slit increases the efficiency of the spectral broadening. Finally, for probe offsets beyond a slit's main peak, both visibility and efficiency fall off (dark purple curve in Fig. 5.7(c)).

A final parameter that can be tuned to explore the double slit diffraction effect is the probe pulse duration. In Fig. 5.8(a) and (b) are show the full interferograms for (a) the original measurement with a 794 fs FWHM probe and (b) the same measurement with a longer probe pulse of 3250 fs. One can see that the longer pulse shows oscillations over a larger range of slit

separations, though less oscillations are visible due the smaller effect the slits have on the probe and its broadening (see Fig. 3.12). Yet, though the probe pulse being longer in time helps with the observation of oscillations at larger slit separations, the reduction of the slit's modulation for longer pulses (see section 3.3.4) acts in the opposite direction, overall reducing the benefits of increasing the probe pulse width. Longer probe pulses could be used to increase the visibility of the oscillations, as a narrower spectral width would lead to lower walk-off effects and higher temporal coherence.

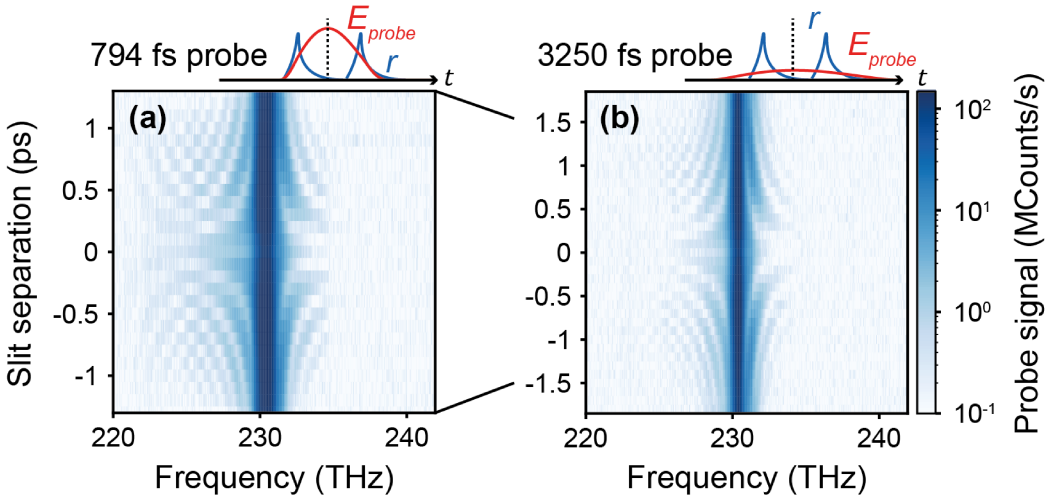

Figure 5.8: Double slit interferograms for two different probe durations. **(a,b)** Probe spectrum against slit separation for probe durations of (a) 794 fs and (b) 3250 fs. Panel (a) reproduced from [81].

Hence, having explored the parameter space of double slit diffraction in time and quantified the various mechanisms at play in a similar fashion to spatial diffraction, we can focus on the problem of modulation rise time posed by measurements of single slit diffraction in the previous chapter. The clear oscillatory pattern of the interference is a much more convincing feature of diffraction than broadening, and thus allows for a finer modelling of the time-varying physics at play. This will allow a refined study of the slit shape and rise time effects, as we try to bring new pieces to the puzzle.

5.2.2 The phenomenological model as a window into electron dynamics

An important result from section 4.3 is the ensemble of evidence hinting at modulation speeds much shorter than what could be achieved by the pump pulse envelope. Fitting the broadening in the probe spectrum undergoing single slit modulation with the Fourier model gives a rise time of 7 fs. We now ask the question whether the double slit diffraction experiment in time

can deliver similar information on the modulation shape and dynamics.

The first step in answering this question lies in understanding how this experimental realisation of the temporal double slit deviates from the ideal theoretical model. In Fig. 5.9(a), the ideal slit shape (orange curve), a box function with perfect contrast (0 to 1 in amplitude) and sharp edges (infinitely fast rise time and decay) is shown in comparison to the modelled slit shape (equation 4.1, blue curve). A width of 200 fs is given to the box function to replicate the pump pulse in timescale. For the same probe profile as used in previous simulations, the resulting spectrum can be computed from the Fourier model in just the same way, and is shown in Fig. 5.9(b). A major difference between the ideal and realistic slit shapes lies in the sinc-shaped envelope of the oscillations for the first, while the second exhibits the experimentally observed Lorentzian decay due to the finite rise and decay times of the single slit modulation. The period of the oscillations remains unchanged as expected, as the slit separation is the same in both spectra, except for every fourth oscillation being suppressed for an ideal slit shape due to the sinc envelope of the decay in spectrum. This highlights the importance of the slit shape in time on the observed spectrum and more particularly on the said envelope of the oscillations.

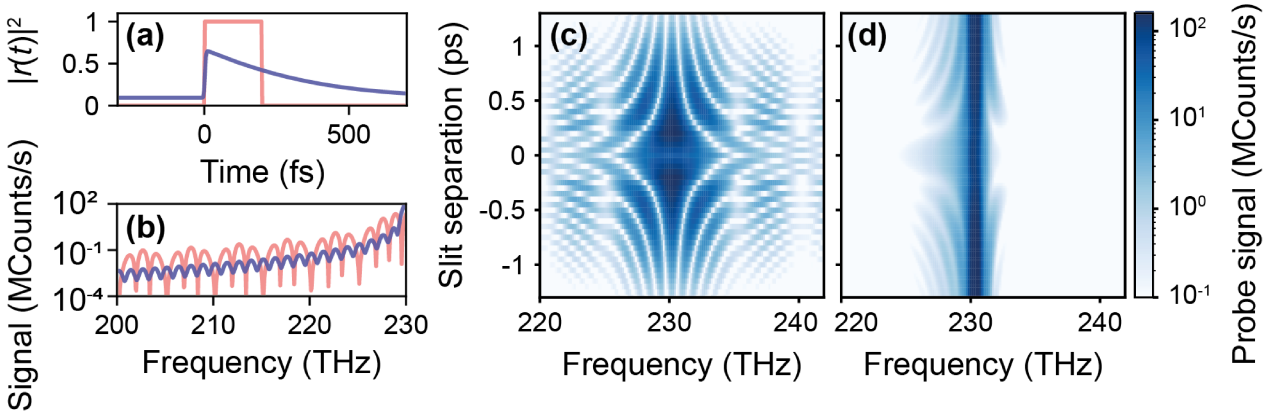

Figure 5.9: Modelling of the double slit experiment in time. **(a)** Diagram of an ideal slit in time (orange curve) against a slit shape mimicking the modulation of reflectivity in ITO (blue curve). **(b)** Resulting oscillations for a slit separation of 800 fs with an ideal slit (orange curve) and the slit shape used in Fig. 5.3(d) (blue curve). **(c,d)** Modelled probe signal against frequency and slit separation in time for (c) the ideal slit shape using the Fourier model and (d) the semi-analytical model with the same parameters as in chapter 4. Reproduced from [81].

The full interferogram of the diffraction spectrum from two ideal slits is shown in Fig. 5.9(c). One can see how the sinc function creates bands in frequency where oscillations are larger in amplitude (here at $\sim$ 222.5 THz and 237.5 THz), regardless of slit separation as these band originate from the single slit shape. Also, the diffraction from a single slit at shorter slit separations in time exhibits a much clearer sinc pattern than what was observed for a realistic slit in Fig. 5.3(d), where only a broadening is present. The sinc shape for a single slit can only

be achieved with an infinitely fast rise and decay time, and won't show if one or both of these scales is finite when compared to the optical cycle.

Beyond the discrepancy between the results for a real slit and the ideal slit model, there is also a major difference between the experimental and simulated interferograms in Fig. 5.3. As mentioned earlier, an asymmetry between the blue and the red ends of the spectrum appears in the experiment, while simulations such as the one shown in Fig. 5.9(c) are perfectly symmetric with regards to the carrier frequency. We attribute this to a combination of frequency shift in the modulation along with dispersion, just as the spectral modulation from a single slit was found to be strongly asymmetric with more generated frequencies in the red part of the spectrum in chapter 4.

To validate this, we simulate the double slit experiment with the semi-analytical adiabatic model. Even though it will fall short in predicting the extent of the observed oscillations, as it fell short in explaining the broadening of a single slit in section 4.3, it reproduces the qualitative features of diffraction taking dispersion into account. The interferogram is shown in Fig. 5.9(d), and exhibits clearly the asymmetry observed in the experiment, with fewer visible oscillations.

So far, the slit has been modelled with a 7 fs rise time (10-90%). Just as in chapter 4, this is a counter-intuitive result when considering the classical description of photocarrier excitation, where carrier dynamics follow the probe pulse envelope in time (here 225 fs). For a single slit experiment, the spectral envelope decay gives information on the modulation's shape in time as shown earlier, including the rise time. The semi-analytical model, following the adiabatic approximation of the driving pump pulse, can only predict rise times down to 30 fs due to the saturation of the reflectivity as the resonance is shifted. What signature does the rise time of the medium's modulation take in the double slit experiment in time?

The Fourier model allows to easily iterate over the various parameters of the double slit time diffraction experiment and observe the effects on the resulting spectra. Changing the rise time is expected to affect the oscillations' amplitude further away from the original carrier frequency of the pulse, as sketched in Fig. 5.10(a). A faster rise time implies larger oscillations for frequencies further away from the center of the spectrum, with little effect on the oscillations close to the carrier frequency peak. This can be understood as the faster dynamics in a single slit lead to a larger broadening of the spectrum and thus larger amplitude in the slit oscillations, or in other words a sharp rise means a high localisation in time, and as a consequence a large spread in frequencies. Equivalently, the modulation decay time affects mainly the amplitude of the oscillations closer to the carrier frequency due to its slow speed.

As the signal decreases for frequencies away from the carrier frequency, the oscillations

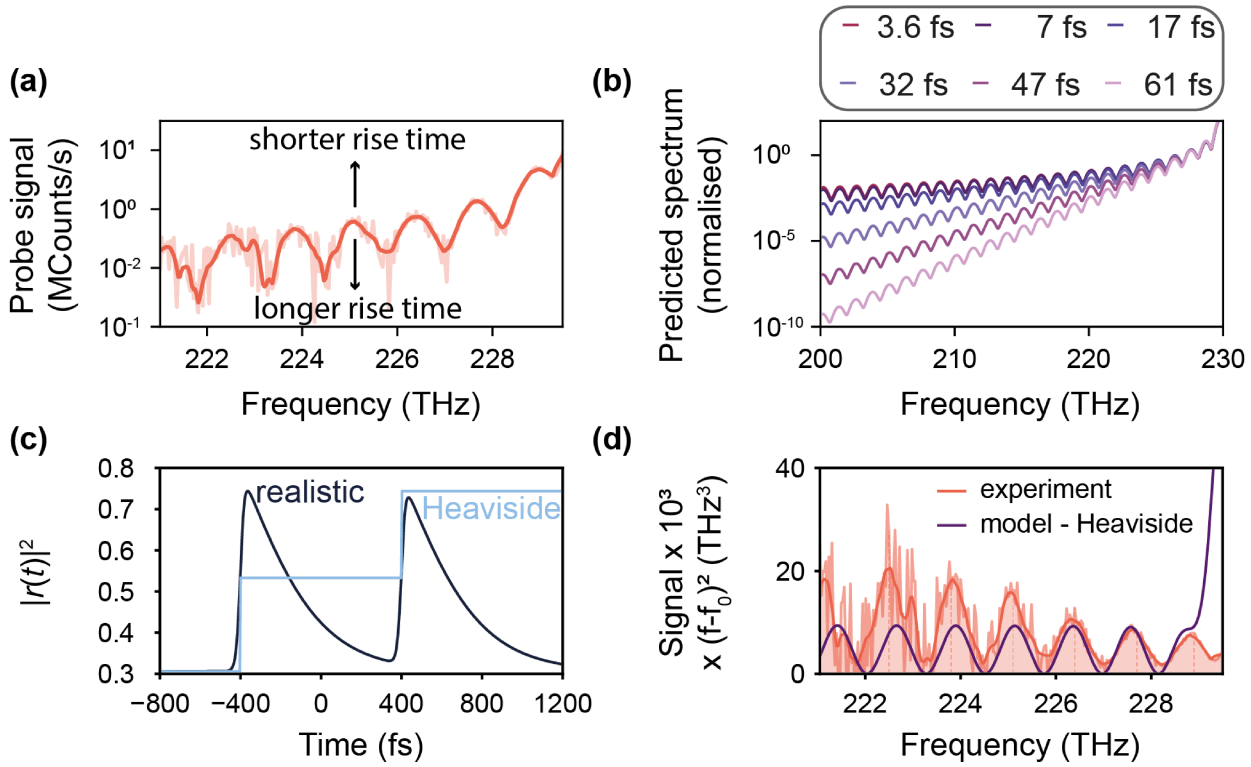

Figure 5.10: Role of the rise time of the modulation on diffracted spectra. **(a)** Measured probe signal against frequency for a slit separation of 800 fs and a probe pulse of 794 fs. The rise time acts on the oscillations further away from the carrier frequency, with decreasing effect as they draw closer to the peak at 230.2 THz. **(b)** Modelled spectra for various rise times, keeping all other parameters constant. Note that the frequency range is extended in comparison to panel (a). **(c)** Diagram of the slit shape used to model diffraction (dark blue curve), against the same shape in the asymptotic limit of zero rise time and infinite decay time (light blue curve). The amplitude of the oscillations was adapted to fit the contrast in reflectivity. **(d)** Probe signal multiplied with the squared difference in frequency from the carrier frequency, in units of THz^3, against frequency, experiment (red curve) and Fourier model with a Heaviside slit function (purple curve). Reproduced from [81].

become comparable to noise, which prevents us from resolving the rise time with high accuracy. This highlights the role of the detector and experimental apparatus: the signal to noise ratio and the detection range (minimum noise against maximum measurable counts, per frequency) together influence the measurement of oscillations at frequencies further away, as there is a need to distinguish them from noise while simultaneously resolving the main peak to have a better fitting of the rise time.

The spectrum for a 800 fs slit separation, 794 fs probe pulse undergoing double slit modulation is computed for various rise times, and displayed in Fig. 5.10(b). Close to 230 THz, all spectra show the same trend as they share the same decay time. But as frequency decreases further away from the main peak, the spectra start separating, with the slower rise times corresponding to a faster decay of the oscillation amplitude. As the rise time converges towards zero, the envelope of the oscillations' amplitude converges towards a $1/(f-f_0)^2$ shape, where

f_0 is the carrier frequency. This makes sense, as the Fourier transform of a Heaviside function (i.e. an infinitely fast rise) is an inverse function - the square originating in the translation from field amplitude to measured field intensity.

The next step would then be to fit the experimentally measured oscillations with the Fourier model to get a value for the rise time. Yet, when running a least-squares optimisation algorithm, the rise time converges to zero over the optimisation process. This is because all rise-times between 0-10 fs are indistinguishable over the range of frequencies in which the oscillations are experimentally measurable. In Fig. 5.10(b), 3.6 fs and 7 fs produce almost indistinguishable results down to 200 THz, while 17 fs can be distinguished below 215 THz. As a result, we can only place an upper limit of 10 fs for the rise time of the modulation

To further verify this, we consider the asymptotic limit where $\tau_{rise} \to 0$ and $\tau_{decay} \to \infty$. Then, the slit function takes the form of a Heaviside function. The absence of decay poses a minor problem in modelling the two slits in amplitude, that is solved by assigning each slit half the height of the full reflectivity modulation, as shown in Fig. 5.10(c). As stated earlier, the Fourier transform of a Heaviside function in time gives a $1/f^2$ dependence on frequency of the intensity spectrum. Hence the spectral oscillations normalised by $(f - f_0)^2$ will have a constant amplitude for a Heaviside-shaped double slit in time. By comparing the experimental counts normalised in the same way in Fig. 5.10(d), the Heaviside prediction is quite close to the experimental measurement, with discrepancies in the absence of the first oscillation, due to the absence of a decay time leading to interference near f_0, and the larger experimental oscillations at lower frequencies. The later is intriguing: the experimental spectrum does not display a sinc pattern and thus should not experience the oscillation amplitude increase with regards to $(f - f_0)^2$. An explanation for this is the increasing mark of noise at lower frequencies, where the oscillations start to blend into the background.

All this provides compelling evidence that the rise time of modulation in ITO is very short, below 10 fs, as the experimentally measured spectra are close to the asymptotic limit. To measure it with greater accuracy, there is a need for far more oscillations to be visible, yet as Fig. 5.10(b) shows it becomes increasingly difficult to distinguish different rise times as they converge towards zero, and producing oscillations at least 30 THz away from the carrier frequency will pose a real experimental challenge. This would require a longer spectral window in the measurement apparatus all the while keeping a good spectral resolution, as well as a lower count rate on the main peak at the carrier frequency, which in this experiment is brought close to saturation of the camera - signal can be made more visible by increasing the probe power but at the risk of damaging costly experimental apparatus.

Beyond further experimental characterisation of the rise time, there is the need to address the physical origin of such a short time scale. Only considering non-parametric processes in the medium, one can break down the dynamics of intraband absorption in the following way: following optical excitation, dephasing of the polarisation oscillations lead to absorption in very short timescales depending on the line width of the optical resonance [95] and moves the electrons in the conduction band into a non-thermal distribution. The electron then thermalise via electron-electron scattering, shifting the effective mass and plasma frequency due to the non-parabolic band of ITO, and this is followed by relaxation - mainly by electron-phonon interaction, as stated in section 3.3. ITO and TCOs in general already have quite unique properties in comparison to metals: the thermalisation of electrons seems to be much faster than in metals [95, 96], even though the time scale for electron-phonon interaction is similar [53, 87]. Del Fatti et al. [87] give interesting insight on why the rise time would decrease for higher intensities: for high electron gas temperatures (i.e. high pumping intensities), the effects of the Pauli exclusion principle decrease and thus the electron-electron scattering is increased. This effect is highlighted in Silver, with a threshold temperature increase of 300 K in the material that leads to a sudden reduction in modulation rise time. The fast rise time is also compatible with recent modeling by Un et al. [80], which also predicts electronic temperature changes of the order of 1e3 K, which seems sufficient to pass the threshold mentioned in [87]. This shows a non-parametric Kerr effect can induce ultrafast modulation on the fs scale, sufficient for strong time-varying effects at optical frequencies, without the need for fs pulses.

5.3 Conclusion

In conclusion, this chapter reported on the first observation of double slit time diffraction at optical frequencies, showing a clear signature in the spectral oscillations. Further study linked the various properties of the pump and probe pulses to the observed oscillations. In the future, one could use double slit diffraction in time as an interferometric tool to reveal the temporal coherence of the probe pulse, just as Young's double slit experiment demonstrates spatial coherence. A double slit experiment in time is also a first brick on the road of more complex temporal modulations such as Fabry-Pérot [97] or photonic time-crystals [98]. The elegant Fourier transform formalism provides an accessible platform for frequency shaping, with potential applications in signal processing.

Furthermore, the rise time measurement technique applied in this present and previous chapter showed to be consistent, and made its proof as a new way to measure medium dynamics

beyond a classic pump-probe measurement such as the ones shown in chapter 3. The sharp rise time, which could not have been measured another way, not only reminds us of the important of solid state physics in photonic time-varying media, but also allows us to access a new regime of applications thanks to the new time scales involved. For this reason, the next and final chapter will cover some topics such as how observe oscillations or access even faster rise and decay times, by exploring time-varying harmonic generation.

Chapter 6

Diffraction experiments in the harmonic regime

6.1 Introduction

Temporal scattering of light in single and double slit diffraction have been proven and thoroughly studied in chapters 4 and 5. With a better understanding of the tools at our disposition to sculpt light, a natural question comes as to which direction these results could be pushed towards. A first path will be explored here in this chapter by applying temporal diffraction to harmonic light generation.

Second and third harmonic are parametric processes, where two or three photons are upconverted through second and third order nonlinear effects. Going back to a scalar version of equation 2.8 and substituting an electric field of the form $E = e^{-i\omega t}$, the nonlinear polarisation takes the form

$$P = \epsilon_0 \left(\chi^{(1)} e^{-i\omega t} + \chi^{(2)} e^{-2i\omega t} + \chi^{(3)} e^{-3i\omega t} + ... \right) \tag{2.8}$$

One can recognise here two new outgoing waves with frequencies 2ω and 3ω, the second and third harmonic of the original frequency ω, called fundamental. The theory of harmonic generation is now well established and rigorous derivations can be found in references [28] and [38]. Nonlinear Optics provide a much more convenient framework for generation of light such as SHG, THG or FWM than photonic time-varying media, so we will not look into modelling these phenomena through the formalism presented in chapter 1. Instead, this chapter focuses on the effects of the same single and double slit modulation on harmonic generation, and try to further our understanding on how to control harmonic light. This time-varying system is more complex than those presented in previous chapters, as the signal being modulated is also a signal being generated within the medium: do time-varying effects happen before, during or after the generation of harmonic light? How do the dynamics of the electrons in the conduction band impact these SHG or THG? Can harmonic light be modulated in both intensity and frequency? This chapter will aim at answering these questions experimentally.

First, the basis for harmonic generation will be laid out, along with a characterisation in

ITO. Then the modulation of SHG in the medium will be studied and followed by a comparison with the direct modulation of the fundamental NIR beam. In particular, we will explore the link between modulation dynamics and harmonic light generation. Finally, modulation of harmonic in GaP, a material of great interest in Nonlinear Optics, will be studied and compared to the performances observed in ITO.

6.2 Spectral modulation of harmonic generation

6.2.1 Harmonic generation in Indium Tin Oxide

To start with, we will focus here on second and third harmonic generation which are commonly found and studied in Nanophotonics, rather than higher order harmonics. In classic nonlinear optical experiments, where mm scale crytals are used, harmonic generation depends highly on phase-matching conditions and material linear (e.g. absorption) and nonlinear properties (e.g. nonlinear susceptibility). In nanoscale media, phase-matching conditions are relaxed and resonances or surface effects such as surface plasmons, Mie resonances, or the Berreman mode in ITO, as well as nonlocal effects become relevant.

Second and third order harmonic generation in ITO has been explored in recent literature. In a first time, Luk et al. recorded in 2015 a strong enhancement of THG using the ENZ plasmonic resonance [99]. In the same year, Capretti et al. demonstrated the generation of second harmonic in ITO thin films [100], and the prominence of the normal component of the electric field E_z in the generation of SHG for p-polarised light. For this reason, our coming harmonic generation measurements will be done in the same excitation geometries as in the previous chapters, using p-polarised light and the Berreman resonance to enhance second harmonic.

Notably, bulk SHG exists only in non-centrosymmetric materials [28, 101], but for media such as ITO, and other similar ENZ materials for which this is not the case, symmetry-breaking at the interface of the material with another medium enables second harmonic generation [54, 100, 102]. The second harmonic is then produced over a region of 10-100 nm of the sample, at the first air/ITO layer (see appendix B). We observe this experimentally, with the 310 nm ITO sample yielding higher SHG generation efficiencies than a similar 40 nm thin film of ITO. Even more importantly, the thicker sample has a higher tolerance to damage thanks to the larger amount of volume heat can be dissipated in, which allows for higher laser repetition rates. This is essential in collecting good harmonic signal during modulation, particularly as

probe intensities need to be kept low in pump-probe experiments to avoid self-modulation effects. For this reason we choose the 310 nm ITO thin film to study modulation of harmonic generation. The probe, which we will now refer to as the fundamental, will be used to generate the harmonic signal in the Berreman-resonant condition to maximise generated light [100], that is an incidence angle of 45 degrees and p-polarised light as depicted in Fig. 6.1(a).

The observation of SHG and THG can easily be confirmed from two measurements. Measuring the spectrum should yield pulses centered at 2ω and 3ω respectively, as expected from harmonic generation theory. This is confirmed in Fig. 6.1(b), where both second and third harmonic spectra are clearly visible, as recorded for the 310 nm thick ITO layer under illumination at 230 THz, without photo-luminescence or other artefacts. Note that the width of the SHG spectrum is 5 THz in Fig. 6.1(b), when the fundamental pulse width is 2.8 THz. This is because of the presence of SFG between different frequencies within the fundamental pulse broadening the resulting harmonic pulse in frequency. If only SHG was taken into account, the second harmonic would have been expected to have a width of $2 \times 2.8/\sqrt{2} = 3.82$ THz as the spectral amplitude at each frequency is squared. Yet, due to SFG, whose strength is comparable to SHG and whose efficiency is constant over the spectral range of interest, various frequencies can interact with each other to generate up-converted photons, thus smearing the Gaussian distribution.

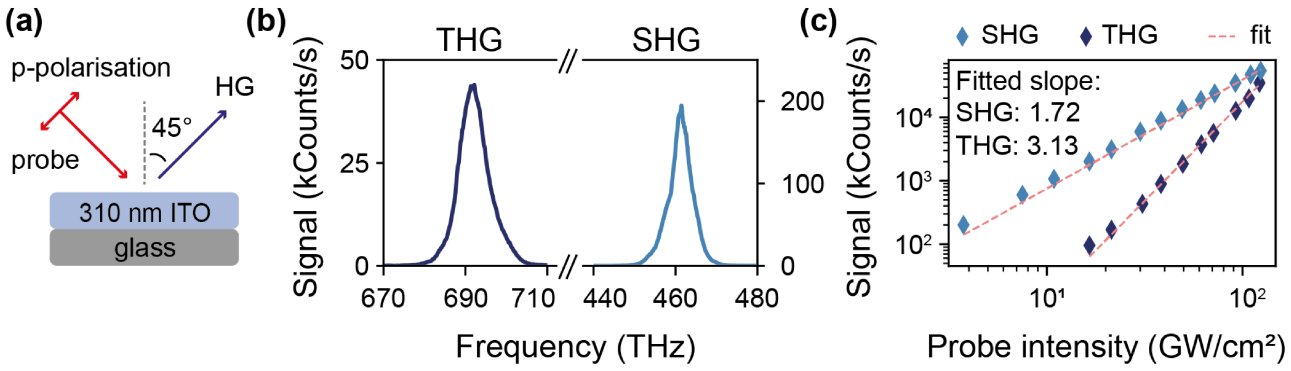

Figure 6.1: Second and third harmonic generation in ITO. **(a)** Diagram of the harmonic generation measurement: the NIR fundamental generates the harmonic signal, using an incidence angle of 45 degrees and p-polarised light. **(b)** Second (light blue curve) and third (dark blue curve) harmonic spectra, for a fundamental intensity of 31 GW/cm^2 and carrier frequency of 230 THz, in a 310 nm layer of ITO. **(c)** Intensity dependence of the SHG (light blue curve) and THG (dark blue curve) in the 310 nm ITO, on a log-log scale, with their respective linearly fitted curves (dashed light red curve).

Furthermore, the intensity dependence curves of the measured signals should exhibit a power dependence of order 2 and 3 for SHG and THG respectively. Fig. 6.1(c) shows the SHG (light blue) and THG counts as a function of fundamental pulse intensity, on a log-log scale for an

illumination at 230 THz and 45 degrees. By fitting the slope of the two curves, the power dependence n of SHG and THG, where $E_{HG} \propto E^n$, are found to be of 1.72 and 3.13 (dashed red curves in Fig. 6.1(c)), close to the expected values of 2 and 3.

One can notice in Fig. 6.1(c) that THG is only comparable to SHG at the highest powers, with the latest being much more efficient at low intensities. For this reason, we will study modulation of SHG in ITO: the probe, which will act as the fundamental and generate the harmonic signal in the pump-probe experiments, needs to be kept at powers as low as possible to avoid self-modulation. SHG will provide much better signal than THG at low intensities and allow better measurement of the spectrum. Moreover, as SHG is originating from the surfaces of the ITO layer, the majority of harmonic likely comes from the first air/ITO interface (see Appendix B).

6.2.2 Single slit time diffraction of Second Harmonic Generation in an Indium Tin Oxide thin film

Having chosen SHG in a 310 nm ITO thin film as a platform to explore temporal modulation of harmonic signal, we now turn our attention back to pump-probe measurements. Time-varying experiments with harmonic light will be done in the same configuration as the NIR in chapter 4, as illustrated in Fig. 6.1(a): the pump and probe pulses are degenerate and impinge on the sample with an 8 degrees incidence angle difference. The probe is p-polarised and impinges at 45 degrees, in the Berreman-resonant condition. The second harmonic signal generated by the probe is then collected in reflection at the same angle. The modulation of SHG is shown in Fig. 6.2(b), where the second harmonic counts against frequency and delay are shown on a logarithmic scale, for the same illumination conditions as in section 4.5 (230 THz, 45 degrees, 114 GW/cm^2). The harmonic spectrum is recorded at 460 THz just as in Fig. 6.1(b), at twice the frequency of the fundamental. A clear redshift of the spectrum can be seen for slightly negative delays, on the rise time of the modulation where the dynamics are now known to be very fast. The overall shape of the SHG spectrum against delay is similar to those obtained with the fundamental in the NIR in section 4.5 (see Fig. 4.12(a)).

To extract information from this scan, we first look at the spectrally integrated counts against delay for a pump intensity of 103 GW/cm^2, as displayed in blue in Fig. 6.2(c). The counts decrease down to $R/R_0 = 7.5\%$, a lower value in contrast to that observed for the probe modulation at 230 THz in section 4.5 for a comparable intensity of 95 GW/cm^2, at a value of $R/R_0 = 15\%$ and shown here in light orange in Fig. 6.2(c).

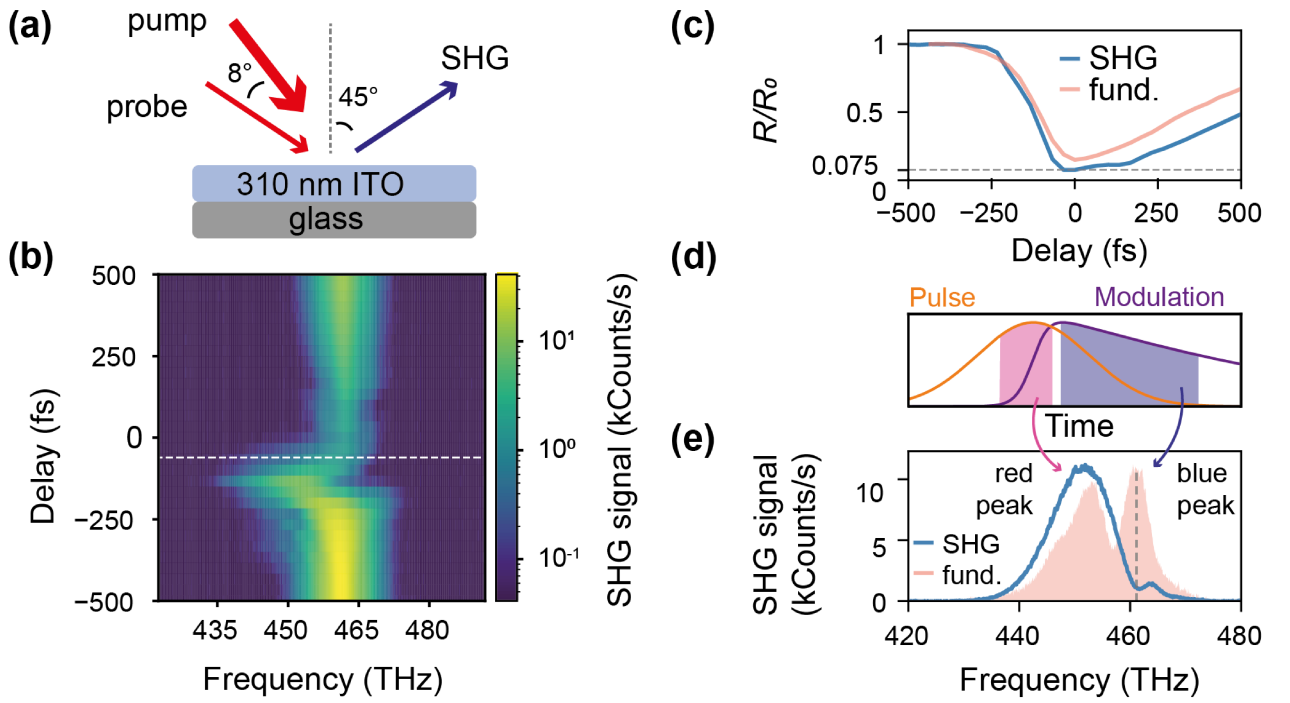

Figure 6.2: Modulation of SHG in Indium Tin Oxide. **(a)** Diagram of the pump-probe experiment at the harmonic with the 310 nm ITO thin film. **(b)** SHG spectrum against delay, on logarithmic scale, for a pump intensity of 114 GW/cm^2 and probe frequency of 230 THz. The white dashed line indicates the delay at which the spectra in panel(e) are shown. **(c)** Relative change in SHG reflected signal R/R_0 against delay (blue curve) for a pump intensity of 103 GW/cm^2, compared to the fundamental probe modulation with delay (light orange curve) at a comparable intensity of 96 GW/cm^2. The horizontal dotted line shows the maximum SHG modulation where the modulated signal amounts for 7.5% of the original signal. **(d)** Sketch of the modulated pulse (orange curve) against the modulation (purple curve) in time. The rise and decay (pink and blue shaded areas respectively) contribute respectively to the redshifted and blueshifted peaks in panel (e). **(e)** SHG spectrum for a delay of -60 fs (blue curve), against the normalised fundamental probe spectrum at the same delay (light red shaded area). The unmodulated peak frequency is shown with the dashed grey line.

Interestingly, the probe and its second harmonic show similar dynamics, with similar observed rise and decay time of the modulation. The SHG exhibits an additional plateau and an extra 'bump' in the decay of the modulation, around 100 fs delay. As was shown in chapter 3, the modulation rise time cannot be extracted from integrated counts such as those shown in Fig. 6.2(c) as these measurements are limited by the probe pulse's width in time. Yet, it was demonstrated in chapter 4 that the dynamics can be determined via the modulation's spectral signature on the probe, particularly at slightly negative delay.

In section 4.5, it was shown that modulation at the fundamental (230 THz) in the 310 nm ITO exhibited two peaks due to frequency shifts, due to part of the pulse experiencing a strong redshift on the modulation rise time and the rest undergoing a smaller blueshift from the decay of the modulation, as depicted in Fig. 6.2(d). As the reflectivity changes significantly, one can

also expect broadening, particularly for the parts of the pulse coinciding with the rise of the modulation in time where the effects are stronger.

Comparing the SHG modulated spectrum in blue to the fundamental modulated spectrum in the red-shaded area in Fig. 6.2(e), the spectra share the feature of having two distinct peaks: one slightly blueshifted above 460 THz and a strongly redshifted peak at about 450 THz. The red peak is significantly broader with a width of 12.6 THz, while the blue peak has a bandwidth comparable to the unmodulated second harmonic at 5 THz. The SHG spectrum shows a higher contrast amplitude between the two peaks than the fundamental probe. However, the extent of generated frequencies and the broadening of the shifted peak are comparable between the two signals. As their modulation amplitude is also comparable as seen in Fig. 6.2(c), this means their dynamics, i.e. rise and decay times, are also similar. From this one can infer that the single slit dynamics of both modulations, of the fundamental and of the harmonic, are similar.

An interesting viewpoint into the time-varying dynamics of the medium lies in the evolution of the probe spectrum with pump intensity, shown here in Fig. 6.3(a) for a delay of -60 fs. At low intensity, the two peaks can already be distinguished, but as the modulation amplitude increases they separate further and further. The lower frequency peak has higher intensity and visibly changes frequency, while the higher frequency peak seems more static. The modulated spectrum seems to converge, or saturate, towards a shifted carrier frequency. The same saturation behaviour can be found in the relative change in signal R/R_0 as a function of pump intensity, as the recorded SHG modulation converges towards a ceiling value at high intensity in Fig. 6.3(b). The modulation of SHG (blue curve) saturates faster at 25 GW/cm^2 than what is observed for the fundamental (red curve). This could explain the second bump observed in the harmonic signal against delay in Fig. 6.2(c), which is very similar to that observed in the bilayer at intensities far in the saturated regime (see Fig. 3.6 in chapter 3).

An interesting figure is the square of the reflectivity modulation for the probe at ω. As the second harmonic field originates from a nonlinear polarisation proportional to the squared fundamental field, we compare SHG modulation to the squared modulation $(R/R_0)^2$ of the fundamental probe. This squared modulation, shown in dashed pink in Fig. 6.3(b), is very close to the experimentally measured SHG modulation in amplitude and pump intensity dependence.

To further verify the spectral dependence on pump intensity, the carrier frequency of each peak of the harmonic modulated spectrum is extracted and compared in Fig. 6.3(c) to the unmodulated SHG peak frequency of 461.18 THz. The high frequency peak (in blue), starting at a frequency of 464.65 THz, seems to redshift at a comparatively low pace, shifting by 1.56 THz between the pump intensity of 10 GW/cm^2 and the highest intensity of 103 GW/cm^2. In

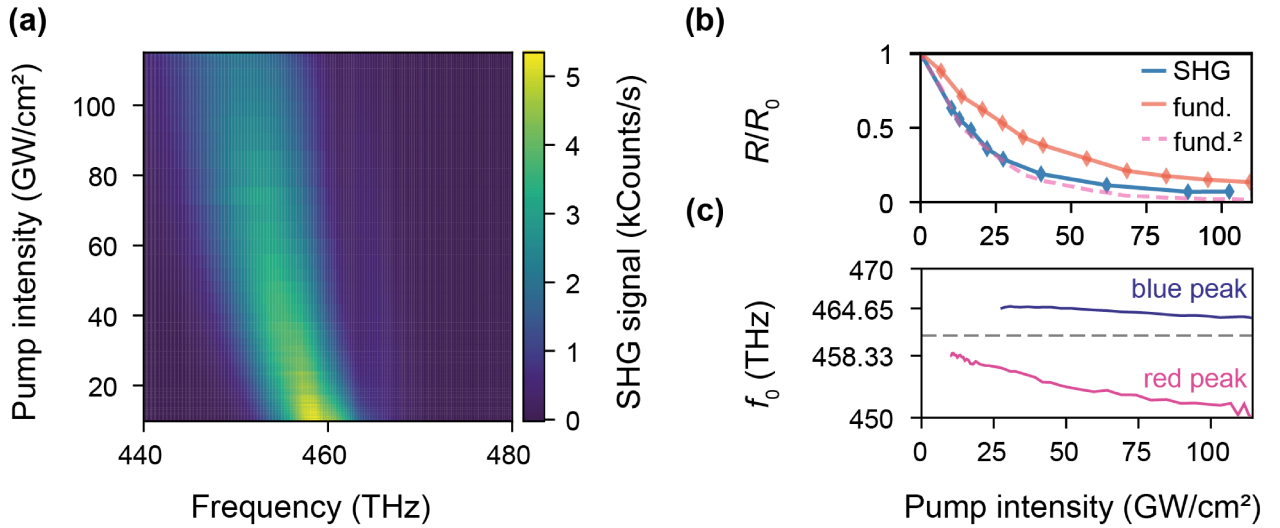

Figure 6.3: Pump intensity dependence of second harmonic modulation. **(a)** Modulated SHG spectrum at a delay of -60 fs as a function of pump intensity. **(b)** Pump intensity dependence of the relative modulation of SHG (blue curve) and the corresponding fundamental probe in the NIR (red curve). The squared fundamental R/R_0^2 is shown in dashed pink for comparison. **(c)** Extracted carrier frequency of the two peaks present in the modulated SHG spectrum, against pump intensity, redshifted (pink curve) and blueshifted (blue curve). The unmodulated spectrum peak frequency is shown with the dashed grey line for comparison.

comparison, the redshifted peak (in pink), starting at 458.33 THz, shifts by 8.78 THz over the pump intensity range, showing a much stronger response to the modulation.

This concurs with the findings from Fig. 6.2 and section 4.5. We interpret these as the lower frequency peak corresponding to the harmonic generated during the rise time of the modulation, just as a strong redshift was observed only at slightly negative delays for the fundamental at 230 THz in the NIR for both the 310 nm ITO and the bilayer (see section 4.2). The higher frequency peak then corresponds to the blueshifted portion of the spectrum, during the decay of the modulation just as in section 4.2. As intensity increases, the relaxation time increases too due to the change in electron heat capacity and the blueshift reduces.

6.2.3 Double slit time diffraction of Second Harmonic Generation in an Indium Tin Oxide thin film

Next, we move on to testing the temporal double slit diffraction experiment with harmonic signal. The double slit measurement is realised in the same way as in chapter 5, with the pump being separated in two and the separation between the time slits being controlled via a delay stage. The double anti-slit modulation of second harmonic generated by the 225 fs FWHM fundamental probe in the NIR is shown in Fig. 6.4(a) for a 1200 fs slit separation, showing the expected features of a large, negative modulation of SHG intensity. The modulation depth is

less affected by the lower intensities from the pumps than the fundamental in the NIR (see Fig. 5.2(a)). The probe's duration is then controlled via the 4-f system as described in section 3.3.4. The resulting unmodulated SHG spectrum is then measured to be centered at a frequency of 462 THz, with a bandwidth of 1.12 THz.

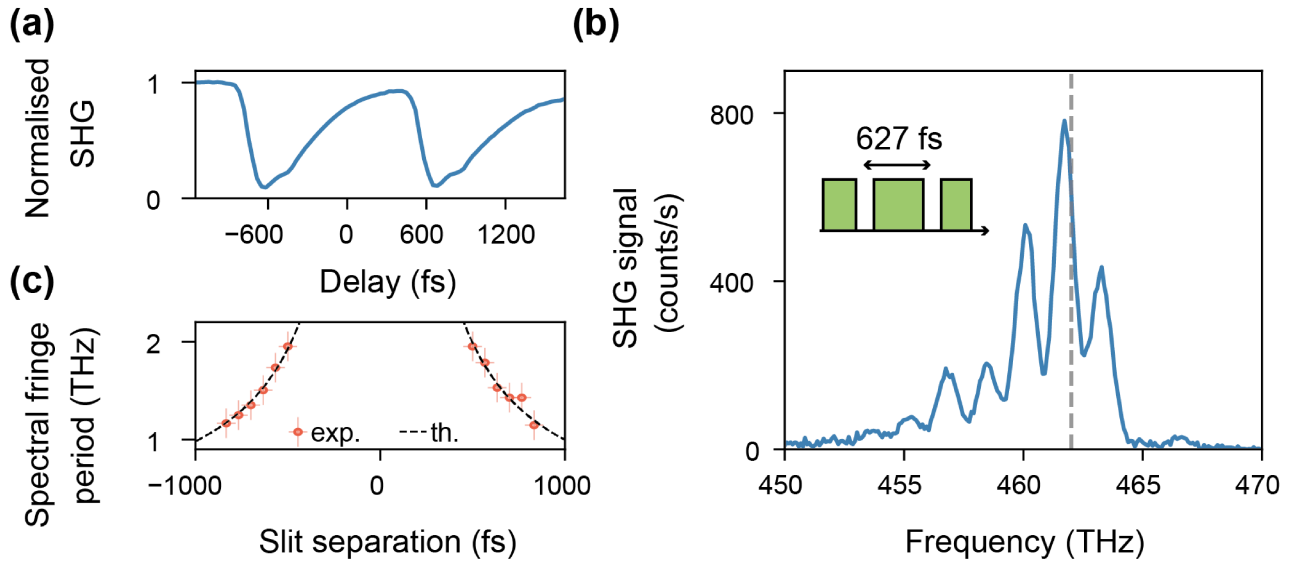

Figure 6.4: Double slit time diffraction of SHG in ITO. **(a)** Normalised SHG signal as a function of delay for two slits with 1200 fs separation and a pump intensity of 62.5 GW/cm^2, for a 225 fs probe duration. **(b)** Diffraction spectrum for a 691 fs long probe and 627 fs slit separation, for a probe carrier frequency of 230 THz and 33 GW/cm^2 pump intensity. The dashed grey line indicates the carrier frequency of the unmodulated probe spectrum. **(c)** Spectral oscillation period against slit separation, experiment (red circles) against Fourier modelling (dashed dark curve). As in chapter 6, errors are standard deviation in slit separation and standard error of the mean in spectral oscillation period.

The diffraction pattern in the spectrum of SHG for a double slit experiment in time is clearly visible in Fig. 6.4(b). The spectrum shows the expected oscillations due to the interference between the two slits, with a decay in signal away from the main frequency peak and visible all the way down to the end of the spectrometer's spectral window, 10 THz away from the second harmonic's carrier frequency. The period of the sinusoidal oscillations against slit separation in time matches those expected from Fourier theory, as shown in Fig. 6.4(c) (red crosses against dashed grey curve). The asymmetry due to the redshift of the spectrum is still present. A striking feature of the diffraction spectrum, in comparison to those observed in chapter 5 for the bilayer, is the large intensity of the oscillations when compared to the peak at the carrier frequency, far above the noise level. Another interesting feature is the low power requirement of the double slit experiment in SHG: the diffracted spectrum is much more visible than those measured with the bilayer: the intensity used here is of 33 GW/cm^2, a fifth the intensities used to get the best achievable diffraction in the NIR. This is due to the lower saturation level of

the SHG modulation in the 310 nm ITO (see Fig. 6.3(b)).

We then investigate the role of pump intensity in the time diffraction pattern. Fig. 6.5(a) presents the diffraction spectrum at various pump intensities, with both pumps being kept at the same level - we will dub this scenario (P2). The spectrum is clearly visible at higher pump intensities, while at lower intensities the oscillation pattern disappears into the noise as the broadening envelope due to the single slit becomes negligible. Just as for the fundamental, the period of the spectral oscillations is verified not to change when both slits' amplitudes decrease with intensity.

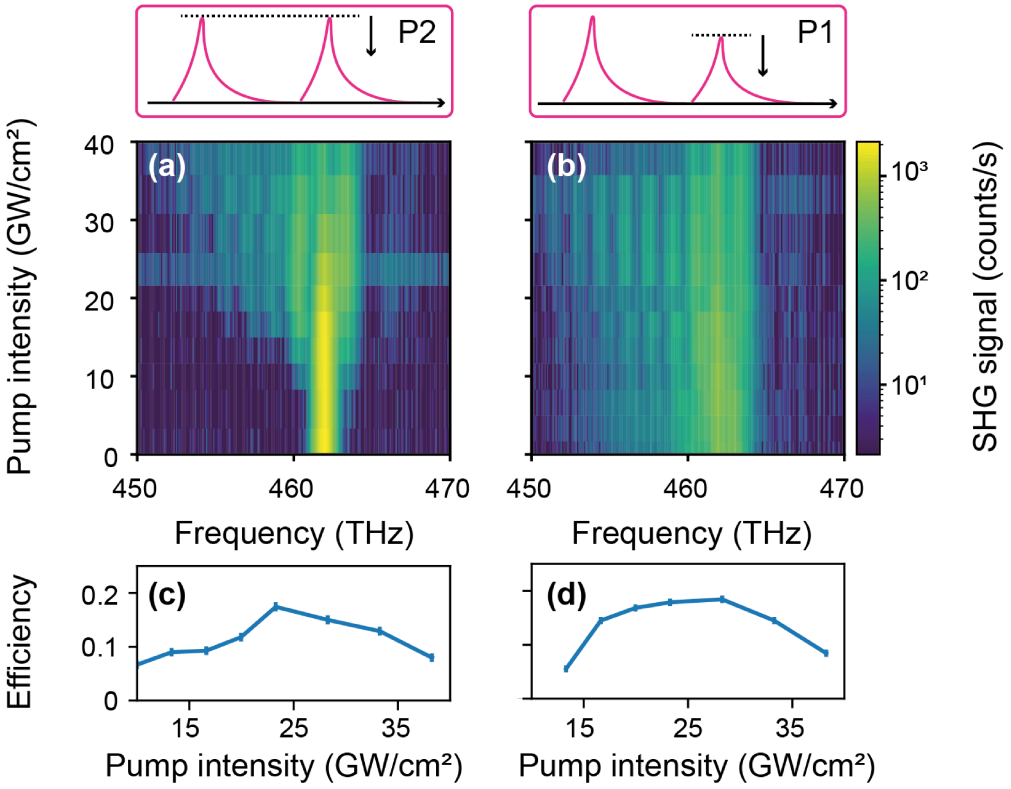

Figure 6.5: Pump intensity dependence of the time double slit diffraction spectrum. **(a,b)** SHG spectrum against pump intensity for (a) both pumps being kept at the same intensity level and (b) one pump being kept at a maximum pump intensity of 38 GW/cm^2 and the other one decreasing in intensity. **(c,d)** Extracted diffraction efficiency, with (c) corresponding to (a) and (d) corresponding to (b).

In comparison, the spectrum under double slit diffraction can also be studied by having only one slit vary in amplitude while the other stays at maximum modulation intensity, a scenario that will be dubbed (P1). As shown in Fig. 6.5(b), the broadening is kept at a higher level thanks to one of the slits still having high contrast. Again, the oscillation period doesn't change, but efficiency will vary.

The extracted efficiencies, defined as the ratio of the first modulated peak to the unmodulated spectrum, as a function of intensity for scenarios (P2) and (P1) are respectively shown

in Fig. 6.5(c) and (d), and are very similar in shape. Due to the asymmetry between the two pumps, the successive increase and decrease in efficiency is less sharp in scenario (P1).

6.2.4 Harmonic versus fundamental wave: new mechanisms for time-varying effects

By investigating the response of second harmonic generation by the probe under optical pumping of ITO, we have already determined the modulation in the harmonic regime share features similar to those of the modulation at the fundamental frequency. Yet, there are also differences that could be due to other time-varying mechanisms that are peculiar to SHG modulation. Fig. 6.6 depicts the various mechanisms that can induce time-varying effects within the medium.

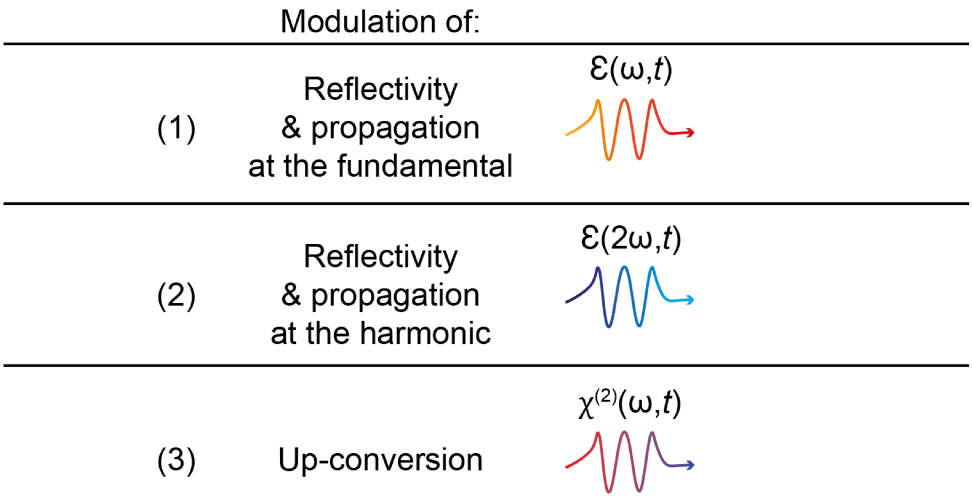

Figure 6.6: Mechanisms for frequency shifting of harmonic generation. Diagram of the three mechanisms that could contribute to the SHG modulation.

First, the probe fundamental is modulated from the change in permittivity of ITO under the pump pulse, as described in previous chapters. This is now well understood as the change in refractive index and Fresnel coefficients during the interaction of the fundamental pulse in the NIR with the medium, which in turn induces the nonlinear polarisation at the origin of SHG.

Second, optical pumping does not necessarily lead to material changes in the NIR only: the visible part of the complex reflection coefficient spectrum could also be modulated from changes in the permittivity at 2ω, inducing time-varying effects on the generated harmonic signal before it is out-coupled to the detectors. Rodriguez-Suné et al. [54] showed in 2020 that nonlocal effects on SHG can be neglected in the pump intensity range used in our experiment, and that background lattice effects are too far in the ultraviolet to affect frequencies at 460 THz, leaving intraband transitions as the dominant mechanism for modulation just as in the

NIR. Hence, the permittivity changes at 2ω originate from the same change in Drude model parameters than at ω. As dispersion of ITO is much weaker in the visible than in the NIR, we can reasonably expect modulation at the harmonic to be weaker than at the fundamental.

Third and last, the probe is up-converted to second harmonic via the nonlinear susceptibility. As the electronic properties of ITO change under optical modulation, the nonlinear interaction of electrons with light can reasonably be expected to vary just as the plasma frequency and electron scattering. Thus, the nonlinear susceptibility could also experience changes in time with the pumping of the medium. Then, as the nonlinear polarisation generating SHG can be expressed $P_{\mathrm{NL}} = \chi^{(2)}E^2$, a temporal change in $\chi^{(2)}$ can induce time-varying effects on the generated pulse just as the changes in reflection coefficient seen in chapter 4 and 5.

All in all, we will divide time-varying effects between these three categories: modulation of the fundamental in the NIR, modulation of the harmonic generated by the probe in the visible, modulation of the $\chi^{(2)}$.

To study and exclude the effect of modulation at $\epsilon(2\omega)$, we replace the probe at 230 THz by a probe at 460 THz. This is done by placing a phase-matched Beta Barium Borate (BBO) crystal in the probe path, generating a strong second harmonic signal. This signal is then filtered to cut the original probe signal at 230 THz, leaving the newly generated signal at 460 THz to act as the probe impinging on the sample. As the pump is still unaffected at 230 THz, this allows to investigate modulation of the sample in the visible under pumping in the NIR. The new probe at 460 THz will now be referred to as the probe at 2ω for clarity, while the original probe at the fundamental (230 THz) will be referred to as the probe at ω. The diagrams for each measurement are presented in Fig. 6.7(a-c).

The relative change in reflected signal of the probe at 2ω is presented in Fig. 6.7(d) in purple, alongside the SHG and probe at ω modulations. As can be seen, the modulation of the probe at 2ω (purple curve) is much weaker than the others, with a maximum decrease in relative reflectivity $R/R_0 = 93\%$. In comparison, the probe at ω (blue curve) drops to $R/R_0 = 15\%$ and the SHG (orange curve) to 8%. Just as in Fig. 6.3(b), we compare the SHG modulation to the squared fundamental modulation $(R/_0)^2$, shown here in dashed light blue. Again, the agreement between the two modulations is good, showing their strong similarity.

Meanwhile, the overall frequency shift of the probe's main peak, from the second harmonic or the probe at 2ω, can also be used to investigate the system. The shifts with delay of the main peak of SHG is presented in orange in Fig. 6.7(e) and exhibits the same evolution than the probes at ω and 2ω (purple curve) in the 310 nm ITO, with a successive decrease and increase around zero delay. Particularly, the second harmonic shifts by -8.75 THz on the rise

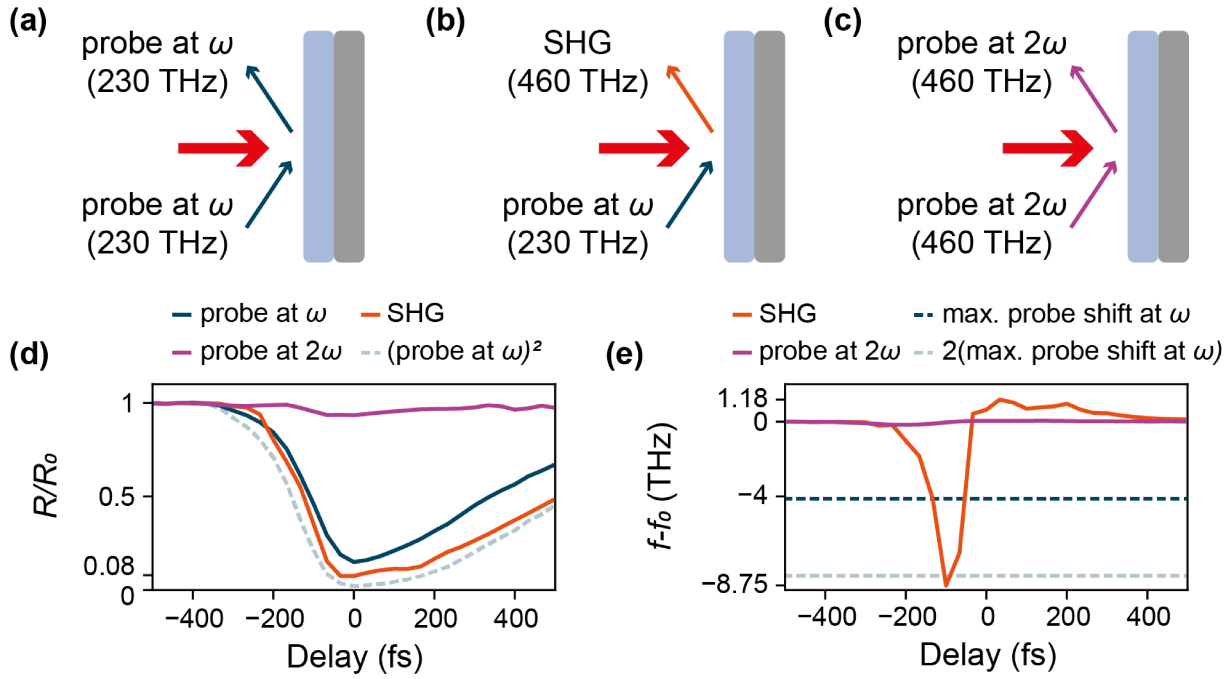

Figure 6.7: Comparison of second harmonic modulation with reference probes. **(a-c)** Diagram of the three distinct measurements shown in panels (d) and (e). (a) Measurement of the reflected probe at ω spectrum (at 230 THz) against delay. (b) Measurement of the reflected SHG spectrum (at 460 THz) generated by the probe at ω against delay. (c) Measurement of the reflected probe at 2ω spectrum (at 460 THz) against delay. **(d)** Relative change in SHG (orange curve), probe at ω (blue curve), squared probe at ω $(R/R_0)^2$ (dashed light blue curve) and probe at 2ω (purple curve) against delay. **(e)** Frequency shift as a function of delay for the SHG signal (orange curve) and a 460 THz probe (purple curve). The shift in the 230 THz cannot be fitted as a function of delay but can be measured to be -4.11 THz at -60 fs delay, or -8.22 THz when squaring the signal, shown here with the dashed blue lines.

time of the modulation, while the probe at ω in the NIR can only go as far as -4.11 THz at the comparable pump intensity of 95 GW/cm^2(dashed blue line). The frequency shift of the probe at 2ω (in purple), at -0.16 THz, cannot explain the difference in frequency shift between the probe at ω and the SHG modulation. On the other hand, if the modulated field of the probe at ω is squared again, the resulting frequency shift of -8.22 THz is much closer to the second harmonic's frequency shift.

Thus, it seems that time-varying effects in the SHG of the 310 nm ITO sample correspond to the modulation at the fundamental (scenario 1 in Fig. 6.6), with the reflected second harmonic field being very similar to the squared reflected fundamental field. Minor differences could be explained by time-varying effects in the visible on signals at 2ω (scenario 2) or a potential modulation of the $\chi^{(2)}$ of ITO in time (scenario 3).

To close the discussion on the respective importance of the three mechanisms shown in Fig. 6.6, it is found that the change in permittivity in the NIR is the dominant modulation for the generation of new frequencies in the SHG spectrum. Due to the low dispersion of ITO in the

visible, little spectral changes can be seen from modulation of the permittivity at 460 THz.

Limitations in the theory prevents us from drawing a definitive conclusion. Time-varying physics could be further tested through modelling, but as was shown in section 4.5 the 310 nm ITO sample deviates from the interface approximation, making both the semi-analytical and Fourier models presented in section 2.3 ill-suited to the situation. Another difficulty in modelling resides in taking into account the phase of the complex reflection coefficient which has not been accurately measured and modelled, and takes a prominent role in the thicker layers as the sample moves away from an interface approximation for the probe.

To conclude, we have demonstrated in this section single and double slit diffraction in time of second harmonic generation in a 310 nm layer of ITO. Experimental results differ from those obtained in the NIR with the fundamental for an ITO/Au bilayer, as the sample exhibits strong frequency shifts linked to time refraction and the splitting of the spectrum in two peaks. A high contrast between these two peaks is achieved, with comparably low pump intensities. A main challenge remains in the modelling of these time-varying effects at the harmonic level, to gain further insight and control on the spectral modulation independently of the nature of the sample or modulation.

6.3 Spectral modulation of harmonic generation in Gallium Phosphide

Though time-varying effects on SHG in ITO have been shown to be stronger than at the fundamental frequency due to frequency doubling, modulation at the harmonic showed limited advantage over that at the fundamental. Furthermore, ITO, though widely recognised for its ultrafast switching capacities, is not commonly used for photon up-conversion and other nonlinear light generation applications due to its strong absorption in the NIR. This prompts us explore different nonlinear materials, where spectral modulation at the harmonic would have a strong impact in comparison to the fundamental. This would for example enable systems with control of the harmonic generated spectrum all the while maintaining resonant properties and applications at the fundamental.

Gallium Phosphide is a popular material in nonlinear Nanophotonics, thanks to its remarkable nonlinear properties, high index and low losses for frequencies below its indirect band gap (below 547 THz), alongside other high index dielectrics such as GaAs, Al-GaAs or $LiNbO_3$ [46, 103]. Notably, GaP has demonstrated high efficiency for the generation of photon pairs via spontaneous parametric down conversion (SPDC) in thin films and metasurfaces, a non-

linear process akin to SFG or difference frequency generation (DFG) [104, 105]. Furthermore, light-matter interaction can be boosted in GaP thanks to nanostructuring, by engineering resonances in nanoantennas. These provide a gateway to compensate for the limitations imposed by the low volume of metasurfaces and thin films. More of interest to us, GaP is capable of ultrafast switching in the visible and NIR region [106, 107]. As time-varying effects have been demonstrated in antennas [108–111], one could think of designing a nonlinear metasurface for SPDC or harmonic generation using GaP, adding reconfigurability and spectral control of the signal using optical pumping. Other applications using GaP metasurfaces could lie in biosensing [112, 113]. We thus aim to test and benchmark the time-varying physics of GaP under optical pumping in the NIR.

6.3.1 Linear and nonlinear properties of Gallium Phosphide in the near-infrared

Our sample consists of 400 nm of amorphous GaP (a-GaP) deposited by sputtering on a SiO_2 substrate. Its refractive index, obtained by ellipsometry, is shown in Fig. 6.8(a), with the real and imaginary parts respectively in yellow and dashed brown. As can be seen, the losses increase in the green and blue part of the visible spectrum due to the indirect band gap at 541 THz. In the NIR, the losses are very close to zero with $\mathrm{Im}(n) = 0.019$ at 230 THz while the real index takes a nearly constant value of about 3.15 over the range. This makes a-GaP a strong material for the engineering of resonators in the NIR and visible, with strong Fabry-Pérot in the visible for nanolayers and a strong magnetic dipole or anapole resonance for antennas in the NIR.

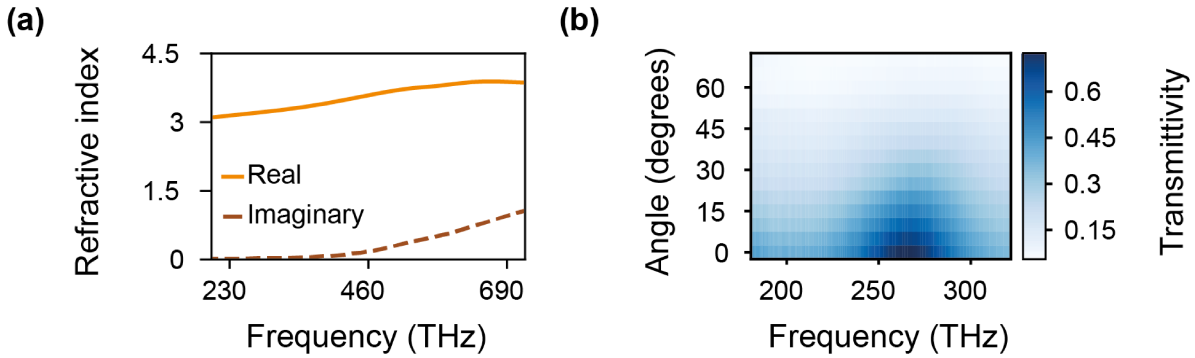

Figure 6.8: Linear characterisation of Gallium Phosphide. **(a)** Real (continuous orange curve) and imaginary (dashed brown curve) refractive indices of GaP as measured from ellipsometry. **(b)** Measured transmittivity of the 400 nm GaP sample against frequency and angle.

GaP has a refractive index 8 times larger and losses 21 times smaller than ITO, due to the two materials having very different band structure. GaP cannot be modelled with the Drude

equation, but also changes the paradigm by exhibiting low losses in the NIR and thus low intraband absorption. We thus expect relatively low time-varying effects under modulation in the NIR.

The transmittivity of the 400 nm GaP sample is characterised experimentally in Fig. 6.8(b), and shows a broad Fabry-Pérot resonance in the NIR at low incidence angle. Fabry-Pérot modes are sharper towards the visible, where shorter wavelengths allow for higher Q resonances, and disappear as the incidence angle increases. For a first investigation of time-varying effects in GaP, the system will be studied off resonance, the topic of resonance engineering in GaP being further discussed in the outlook. For this, we use the same frequency and incidence angle than for the 310 nm ITO sample in sections 4.5 and 6.2.2, at 230 THz and 45 degrees, where the Fabry-Pérot resonance is absent.

Time-varying experiments in GaP will be done in the same configuration than in chapter 4: the pump and probe pulses are degenerate and impinge on the sample with a 8 degrees incidence angle difference. The probe is p-polarised and impinges at a 45 degrees angle, and the reflected and transmitted signals are collected as illustrated in Fig. 6.9(a). The normalised changes in transmission (orange curve) and reflection (blue curve) are shown in Fig. 6.9(b), where T (R) is the spectrally integrated transmitted (reflected) signal and T_0 (R_0) is its initial value before modulation.

Modulation is stronger in transmission than reflection, with respective minimal signals $T/T_0 = 0.89$ and R/R_0 of 0.94. The signal sharply decreases, with a temporal resolution limited by the probe pulse, but the decay time of the modulation is here very sharp, in contrast to ITO. It seems as if there are two decay processes, a first within the probe's duration, and a second with a slower time scale. Both the rise and fast decay times are measured to be at or below the pump rise time of $\sim$ 110 fs (half a FWHM of 225 fs). Grinblat at al.'s measurements of optical switching in GaP in the visible to NIR range [106], at higher frequencies but in a much thicker crystalline sample of 350 µm, showed that TPA plays an important role, and can exhibit time-scales down to $\sim$ 10 fs for both rise and decay time, which explains the observed dynamics.

Another implication of Grinblat et al.'s work on TPA is that GaP's main modulated property is absorption during propagation within the medium, rather than the Fresnel reflection and transmission coefficients at the interfaces. This could explain why the modulation in reflection is weaker by a factor ~ 2 in comparison to the modulation in transmission: part of the reflected probe signal originates from the air/GaP interface, and as a consequence does not experience the change in losses within the medium.

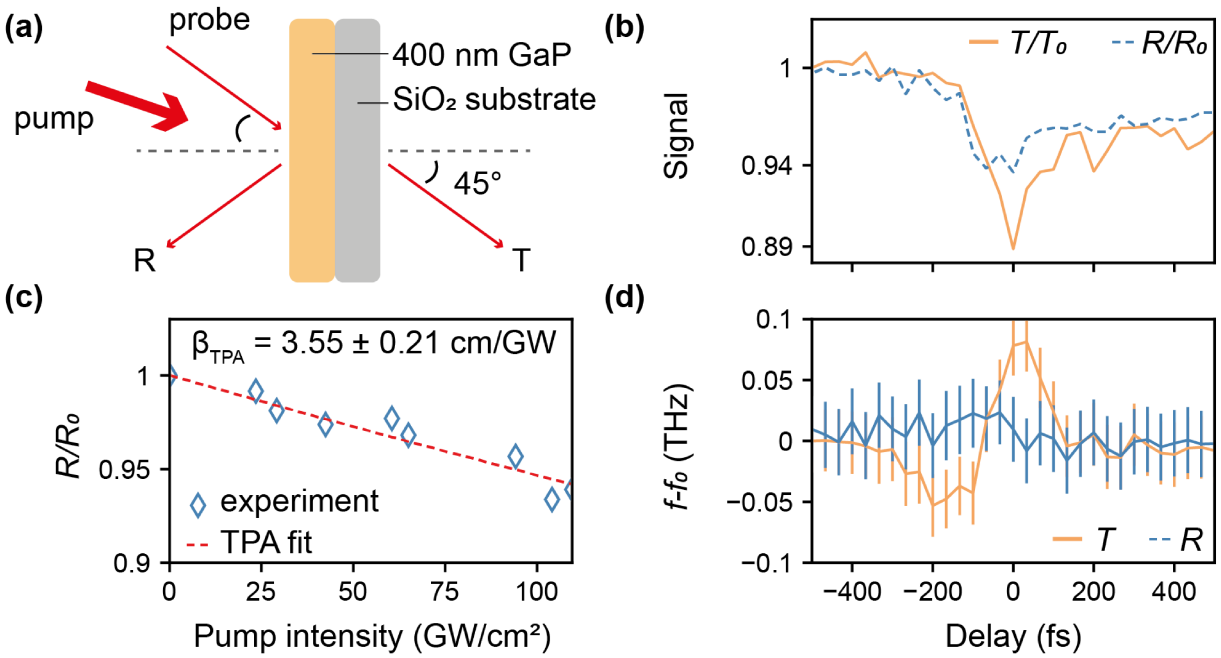

Figure 6.9: Optical modulation of GaP in the NIR. **(a)** Diagram of the experimental pump-probe setup for optical modulation of a GaP thin film. **(b)** Relative change in transmission T/T_0 (orange curve) and reflection R/R_0 (dashed blue curve) for a pump intensity of 110 GW/cm^2, carrier frequency of 230 THz and an incident angle of 45 degrees. **(c)** Pump intensity dependence of the reflected probe signal: experiment (blue diamonds) and two-photon absorption (TPA) fit (dashed red curve). **(d)** Frequency shift in the probe signal in transmission (orange curve) and reflection (blue curve).

To verify our hypothesis on TPA, we compare our study on pump intensity dependence of the modulation in reflection to reference [106], by extracting the two-photon absorption coefficient β_{TPA}, given in units of cm/GW (see appendix D). The measurement, displayed in Fig. 6.9(c), shows the maximum reflection modulation (blue diamonds) as a function of pump intensity. This reflected signal decreases linearly in intensity as the pump intensity increases, with the model (dashed red curve) fitting well with the data. The low change in transmittivity of the sample in the NIR is expected as the nonlinear Kerr effect is known to be weak in GaP, and appears linear as the effect of TPA is perturbative. By fitting the TPA model to the experimental data in Fig. 6.9(c), we find a value of $\beta_{\mathrm{TPA}} = 3.55 \pm 0.21$ cm/GW. In comparison, Grinblat et al. [106] determined via Z-scan measurements the β_{TPA} coefficient to be of the order 3 to 8 cm/GW for low to high pump frequencies below the band gap, in good agreement with our results.

Next, time-varying effects on the reflected and transmitted probe spectra are quantified by extracting their respective spectral shift and broadening. The frequency shift as a function of delay for a pump intensity of 110 GW/cm^2 is shown in Fig. 6.9(d) for both signals. Surprisingly, the reflected signal shows little sign of time refraction, whereas the transmitted signal shows a

successive decrease and increase in frequency around zero delay. This could be explained by the weaker modulation in reflection than in transmission. For the latter, the negative and positive shifts have comparable amplitude, showing the modulation rise and decay times are similar. No broadening is recorded for either reflected or transmitted signals.

Hence, we have determined that GaP, in the absence of resonance, exhibits better modulation in transmission than in reflection in the NIR, with both a larger change in transmittivity and frequency shift. These changes were confirmed to be due to TPA in the medium, in agreement with literature [106]. For this reason, our subsequent experiments on harmonic generation modulation in GaP will be done in transmission.

6.3.2 All-optical switching of third harmonic generation in a Gallium Phosphide thin film

Following the investigation of optical modulation of GaP in the NIR, a nonlinear characterisation is the next logical step before investigating time-varying effects of harmonic generated light. First, the nonlinear properties of GaP are measured and compared to those of ITO. Those measurements are done within the pump-probe setup, in the absence of the pump modulating the medium, as shown in Fig. 6.10(a).

We use nonlinear scattering theory, a useful tool in nonlinear nanophotonics (see appendix C) to extract the nonlinear susceptibility of materials. This allows us to investigate the nonlinear response of GaP and ITO for comparison, and their respective potential for harmonic light generation. Regarding ITO, it is known that Kerr nonlinearities present a great enhancement around the ENZ frequency in TCOs [53, 60, 61], yet the $\chi^{(3)}$ for the nonlinear Kerr effect should not be mistaken for the $\chi^{(3)}$ for THG. Not only are they different by nature, as the strong Kerr effect in ITO originates from non-parametric processes (parametric Kerr effect, originating from photon scattering, is weaker in this medium), while THG is parametric, but they are distinguished by their full mathematical expression - $\chi^{(3)}(\omega,\omega,\omega,-\omega)$ against $\chi^{(3)}(3\omega,\omega,\omega,\omega)$. This prompts for a measurement of the ITO $\chi^{(3)}$ (which will now be used to refer to $\chi^{(3)}(3\omega,\omega,\omega,\omega)$), to test the presence of enhanced harmonic generation at the ENZ frequency. The $\chi^{(3)}$ is extracted by measuring the input fundamental and output THG power in transmission. TMM and nonlinear scattering theory are then used to compute the $\chi^{(3)}$ from the experimental data. Note that only $\chi^{(3)}$ and not $\chi^{(2)}$ can be extracted using this method in centrosymmetric materials, as SHG is generated at the surface [28, 101] and would require more advanced modelling.

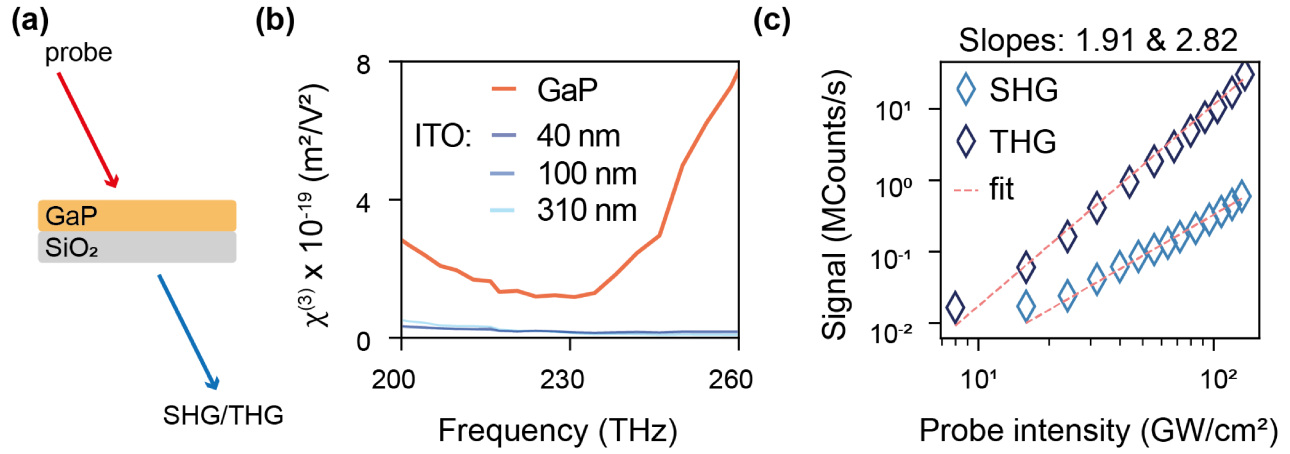

Figure 6.10: Nonlinear characterisation of Gallium Phosphide. **(a)** Diagram of the experimental setup for the characterisation of harmonic generation in GaP. **(b)** Measured nonlinear susceptibilities of ITO for various layer thicknesses and a-GaP for comparison. **(c)** Second and third harmonic signals in transmission against probe intensity for the 400 nm thick a-GaP thin film.

We test ITO samples of various thickness 40, 100 and 310 nm, with increasing ENZ frequency with thickness. We use the same 400 nm a-GaP sample, which is known to have low second harmonic generation but higher third harmonic in comparison to crystalline GaP [114]. The measured $\chi^{(3)}$ spectra are shown in Fig. 6.10(b), with GaP in red and the ITO samples in various shades of blue. For ITO, all three samples have a $\chi^{(3)}$ amplitude of about 2×10^{-20} m^2/V^2 in the range of 220 to 240 THz. In comparison, glass has a $\chi^{(3)}$ of about 10^{-22} m^2/V^2. GaP, on the other hand, shows much stronger nonlinearities, an order of magnitude above ITO in the spectral range of interest, and drastically increases with higher frequency. An increase of the $\chi^{(3)}$ with lower frequencies is also to be noted.

Hence, we show there is no particular enhancement of harmonic generation around the ENZ frequency of ITO due to material properties. Note that photonic architectures, such as the Berreman mode, can still enhance the fields within the layer and thus harmonic generation. A second result is the fact that GaP is better for third harmonic generation than ITO, motivating further experiments for temporal modulation of GaP THG.

As a-GaP is amorphous, it does not present a bulk $\chi^{(2)}$, yet as described earlier SHG is still produced at the interface just as for ITO due to symmetry breaking. The intensity dependence of transmitted SHG and THG in the thin film is shown in Fig. 6.10(c). Contrary to ITO, GaP shows a higher level of THG (in dark blue) than SHG (light blue) at the probe intensities used in the experiment, due to its larger $\chi^{(3)}$ than ITO. The fitted power dependence slopes (1.91 and 2.82, in dashed red) are once again close to the expected values of 2 and 3, verifying the nature of the signal. In ITO, the choice of SHG to explore temporal modulation is motivated

by the strength of SHG at low intensities as well as the fact that most of the signal originates from a single interface, which is not the case in GaP due to the much lower absorption at the fundamental frequency of 230 THz than ITO. Overall, this motivates us to use THG to investigate optical modulation in the GaP layer.

Measurements of time-varying effects in the harmonic signal of GaP are done in the same manner than in section 6.2, with the third harmonic generated by the probe collected in transmission as illustrated in Fig. 6.11(a). The THG measurement is done with a pump intensity of 122 GW/cm^2, a fundamental probe at 230 THz and a 45 degrees incidence angle. The spectrally integrated THG signal as a function of delay is shown in Fig. 6.11(b) and compared to the fundamental and the cubed fundamental. As can be seen, the third harmonic signal (purple curve) undergoes significantly stronger optical modulation, with T/T_0 falling down to 36% at zero delay, where T is the spectrally integrated transmitted signal and T_0 is its initial value before modulation. Again, the rise and decay time scales measurement is limited in resolution to the rise of the pump/probe fundamental pulse, at $\sim$ 110 fs.

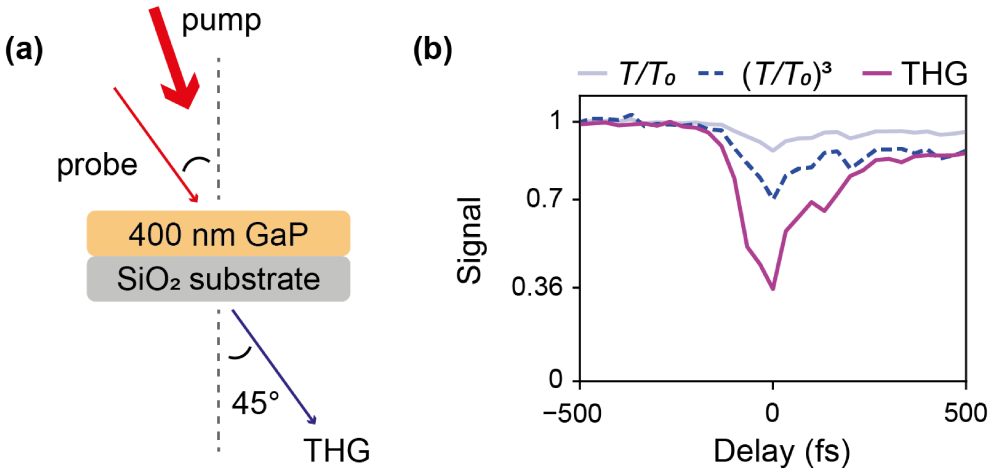

Figure 6.11: THG modulation in GaP. **(a)** Diagram of the pump-probe setup used to investigate the temporal modulation of harmonic in GaP. The probe impinges at 45 degrees incidence angle, with a frequency of 230 THz. The pump is degenerate and at an angle 8 degrees below that of the probe. **(b)** Relative counts against delay for the fundamental probe signal at 230 THz in transmission (grey curve), the THG signal (purple curve) and the cubed transmitted fundamental modulation (dashed blue curve). The sample is modulated with a pump intensity of 110 GW/cm^2.

In comparison, the transmitted fundamental (grey curve) only experiences a $T/T_0 = 89\%$, cannot explain the much stronger modulation of transmitted third harmonic in GaP. Unfortunately, it is not possible for us to verify whether modulation of a probe at 690 THz by a pump at 230 THz could explain the difference.

The fundamental probe field propagating through the medium generates the nonlinear po-

larisation at the origin of the transmitted THG, and thus it is reasonable to compare the cubed fundamental modulation to the THG modulation as was done for SHG in section 6.2.4. As can be seen in Fig. 6.11(b), $(T/T_0)^3 = 70\%$ at the fundamental, showing a major discrepancy between what could be expected from modulation at the fundamental and the observed modulation at the third harmonic level.

Hence, we have demonstrated strong modulation of transmitted THG signal in GaP, far beyond the observed modulation at the fundamental. This is qualitatively different than the results obtained in ITO, for which modulation of SHG is similar to modulation at the fundamental. With a different band structure, GaP brings different nonlinear properties, particularly in rise and decay time. Having shown a good contrast in THG intensity under optical modulation, we can now turn our attention to spectral modulation of this THG signal.

6.3.3 Spectral features of time diffraction in the third harmonic of Gallium Phosphide

The full THG spectrum against delay under modulation with a pump of intensity 122 GW/cm^2 is shown in Fig. 6.12(a). Near zero delay, as the signal decreases, the modulated spectrum exhibits visible frequency shifts. For the spectrum at -60 fs delay in Fig. 6.12(b) (brown curve), a frequency shift of -2.3 THz is observed, while the intensity of the spectrum is less than half that of the unmodulated spectrum shown here in yellow. The modulated spectrum is asymmetric, with a skew towards higher frequencies likely due to the residual amount of unmodulated pulse.

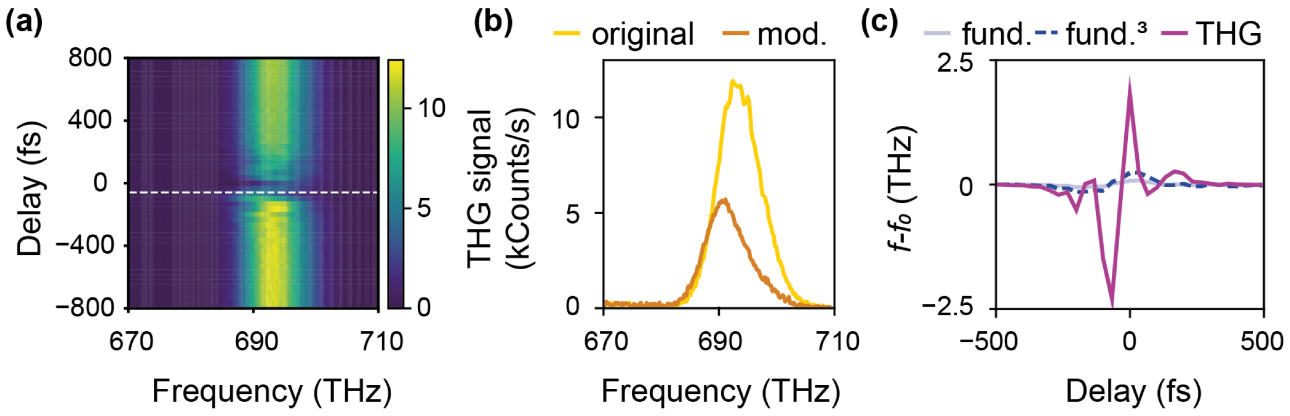

Figure 6.12: Spectral modulation of third harmonic in GaP. **(a)** THG spectrum against delay for a pump intensity of 122 GW/cm^2, incidence angle of 45 degrees and fundamental probe carrier frequency of 230 THz. The white dashed line indicates the delay at which the spectrum in panel (c) is shown. **(b)** Unmodulated (yellow curve) and modulated at -60 fs (brown curve) third harmonic spectra, from the measurement shown in panel (a). **(c)** Corresponding frequency shift against delay for the THG signal (purple curve), fundamental (grey curve) and cubed fundamental (dashed blue curve).

The frequency shift of the THG signal as a function of delay (purple curve) in Fig. 6.12(c) is similar in shape to that observed in ITO, with successive redshift and blueshifts of the carrier frequency, with more balance between each directions (-2.3 against +1.8 THz), showing and confirming the signature of a short decay time of the complex phase modulation. This would match with the recorded decay of the modulation seen in Fig. 6.11(b) and reported by Grinblat et al [106], and could prove a useful tool for the realisation of optical time-varying systems requiring short recovery times, such as time crystals. In comparison, the fundamental's frequency shift is negligible at a value of -0.05 THz, or -0.15 THz if the modulation is cubed. Thus, we have demonstrated strong frequency shifting and fast modulation dynamics in the third harmonic signal generated by GaP under optical modulation of the medium, unmatched by the time-varying effects at the fundamental.

An important parameter that could yield information on all-optical modulation in the third harmonic of GaP would be the dependence of the modulation on the pump intensity. The transmittivity measurement, displayed in Fig. 6.13(a), shows the pump intensity dependence of the THG relative change in transmittivity T/T_0 (purple curve). Though the fundamental modulation is linear with intensity due to the perturbative action of TPA as seen in section 6.3.1, THG modulation differs by experiencing a nonlinear intensity dependence throughout the pump intensity range (shown here in dashed light blue).

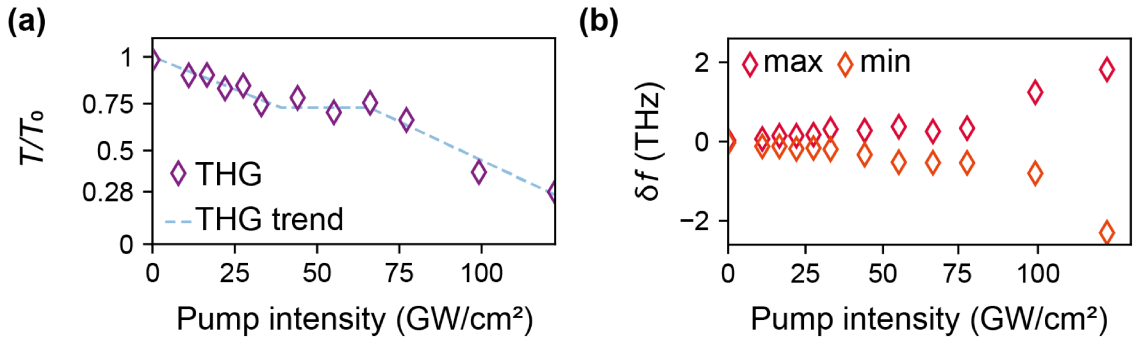

Figure 6.13: Pump intensity dependence of optical modulation in GaP. **(a)** Pump intensity dependence of transmission modulation in THG signal (purple diamonds) in a-GaP. The observed trend of the THG modulation is sketched in dashed light blue. **(b)** Maximum (red diamonds) and minimum (orange diamonds) frequency shift of THG from 2 different delays as a function of pump intensity.

Additionally, the extraction of the maximum and minimum frequency shifts from a single time slit in GaP in Fig. 6.13(b) confirms the observed pump intensity dependence of the transmitted signal change. The frequency shift of the THG is once again nonlinear with intensity, with stronger effects arising at high pump intensity. This behaviour is consistent with the shape of the recorded change in transmittivity (purple diamonds) in Fig. 6.13(a). Possible explana-

tions could lie in additional phenomena contributing to the third harmonic modulation such as modulation of the $\chi^{(3)}$, FWM, nonlocal effects or other unforeseen electron dynamics, or three-photon and higher-order absorption effects gaining prominence at higher intensities [115], explaining the change in slope in Fig. 6.13(b). Modelling the experimental will be an important challenge to tackle to further improve our understanding of modulation of third harmonic in GaP.

We thus show that GaP presents strong all-optical spectral modulation of its third harmonic signal, both in frequency shifts (between -2 and 2 THz) and amplitude ($T/T_0 = 36\%$ signal decrease), whereas the fundamental signal in the NIR shows little modulation. This is a very interesting and conclusive result for further control of photon up-conversion in nanostructures.

6.4 Conclusion

In conclusion, time-varying effects in modulated harmonic generation in nonlinear media have been demonstrated. For both SHG in ITO and THG in GaP, these effects show stronger change in signal (R/R_0 or T/T_0) and spectral features than the experiments at the fundamental in the NIR, hinting at the potential of effective ultrafast switching of nonlinear light generation. In ITO, the harmonic follows the same dynamics than the NIR probe, thus making a good platform to lead the same diffraction experiments and investigations of material dynamics that could be done at lower frequencies. In GaP, the contrast between fundamental and harmonic modulation is particularly striking, making further experiments in this material promising as this was demonstrated in a non-resonant system. The physics at play were partially uncovered thanks to TPA, but much more work remains before the system is fully understood. Particularly, a change in pump intensity dependence of the third harmonic modulation in GaP above 100 GW/cm^2 along with a strong spectral response hints at new mechanisms enhancing the modulation. Using resonant architectures, these high intensities within the medium could be leveraged to create efficient time-varying structures. For both materials, the main barrier in bringing these time-varying effects within our understanding is modelling: the samples used to achieve high harmonic signal are too thick to appear as an interface to light, leading for example to causal effects during propagation within the medium. We close with this chapter the last topic of investigation in this thesis, and we can move on to discuss the importance and achievements of these results, as well as the next steps currently investigated of how one could move towards to push nanoscale time-varying media further.

Chapter 7

Summary and outlook

Throughout this thesis, the topic of diffraction in time has been thoroughly discussed and experimentally tested and proven. Building up on fundamental concepts of time-varying media and wave physics, and exploiting the recent discovery of ITO as a nonlinear optical platform for Nanophotonics as introduced in chapter 2, single and double slit diffraction in time has been demonstrated in the visible and NIR regime.

The first step in the experimental realisation of diffraction consisted in the making of a time slit. Using nanoscale systems and Nonlinear Optics, one can reduce spatial constraints to realise a time-varying mirror for diffraction in thin-films such as the bilayer presented in chapter 3, achieving high contrasts in reflectivity on short timescales. The spectral effects of the single slit in time were then studied in chapter 4, building our understanding of the broadening and dynamics within the medium as well as pointing at interesting new dynamics in the high pump intensity regime. Then, we showed the first realisation of double slit diffraction in time at optical frequencies in a nanostructure in chapter 5, and uncovered a shortening of the rise time of the modulation of 1-10 fs, far below the pump pulse's 225 fs duration. This demonstrated the potential of the time-varying mirror for frequency control, by using Fourier formalism, but also as a spectroscopic tool for materials. Finally, we explored temporal modulation of harmonic generation from a single slit in ITO in chapter 6, and found that second harmonic can be modulated with similar features and dynamics than the fundamental probe in the NIR. In comparison, GaP, a high-index dielectric, shows strong modulation of its third harmonic far beyond what can be achieved at the fundamental, demonstrating the presence of new dynamics and a potential for reconfigurable generation of nonlinear light.

All in all, we have not only shown the experimental demonstration of diffraction in time and the benefit of a time-varying formalism in understanding and modelling our systems, but we have also gained great insight on the optical modulation mechanisms within ITO. New phenomena have been found, with in particular the intriguing rise time dynamics of electrons within ITO and the new behaviour of GaP's THG at high modulation intensities.

Thankfully, though this thesis comes to a term, research on the topic doubtlessly will not. A first aspect that will not be extended here as it does not lie within the author's field of expertise is theory: at the core of the time-varying media community, theorists have been

essential to the renewal of the field in the recent years, and have an important role in both coming up with new applications and assisting experimentalists with new models allowing for simulations and better understanding of their platforms. This thesis has highlighted, amongst other things, the necessity to model causality in time-varying systems (a suggestion is the use of Laplace transforms, commonly used in engineering for feedback controls), or to work on models being able to handle both short timescales (beyond the adiabatic limit) and dispersion of the medium. Yet, as sometimes is the case, much work remains to be done experimentally to catch up with the plethora of applications theory predicts for time-varying systems. In Nonlinear Nanophotonics, work can be led and divided in tiers.

At the base level, there is the necessity to understand and probe the fundamental and practical limitations of nanoscale time-varying systems. For ITO, this means getting a better understanding of the electron dynamics under the saturation regime, as well as overcoming limitations such as efficiency or damage to the medium. These could be overcome with architecture, as was demonstrated using plasmonic nanoantennas [69, 78], though efficiency was recently shown to have an absolute upper limit by Khurgin [2], or engineering thermal effects to allow for a better dissipation of heat in the medium, thus enabling higher repetition rates for time-varying experiments. In GaP, as well as other high-index dielectric and other promising materials for nonlinear optics and ultrafast switching, e.g. transition metal dichalcogenides and other 2D materials, a better understanding of the optical excitation mechanism will also be useful for designing time-varying media. Particularly, the fast relaxation of the permittivity modulation in GaP is of great interest and an asset when compared to ITO. The use of resonances and photonic architecture in high-index materials [107] would then allow for further engineering of time-varying effects.

Notably, one could leverage the integration of multiple materials within an individual antenna to enhance nonlinear optical effects [43, 44, 116, 117]. Photonic gap antennas in particular, by slotting a thin low-index material within a high-index material, allow for a strong field enhancement within the low-index material without affecting the overall antenna resonance [118, 119]. Though this falls beyond the scope of this thesis, we propose the integration of a thin ITO layer within a GaP nanodisk to enhance the ultrafast switching and time-varying effects within the antenna (see Fig. 7.1(a)). Antennas for time-varying physics are of great interest, as they are a first step towards adding spatial dimensions to our nanophotonic systems to make them truly spatiotemporal.

In fact, adding spatial to temporal modulation would be the main next step in the development of active, reconfigurable metasurfaces, and this stream of research will likely be very

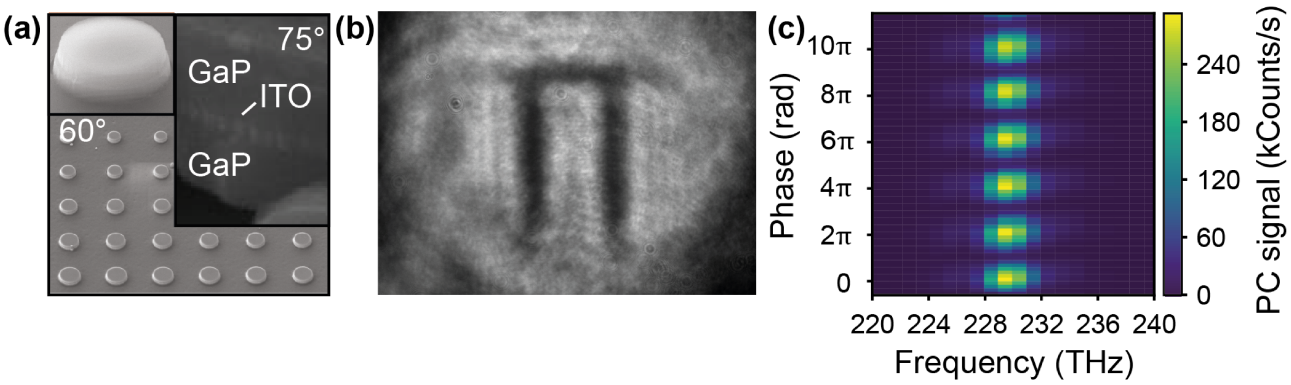

Figure 7.1: Integration of ITO in new applications. **(a)** Scanning electron microscope images of photonic gap antennas made of GaP with a 21 nm ITO thin film in the middle, visible in the top right inset. **(b)** Direct imaging of the probe beam after reflection from the 310 nm ITO thin film at 0 degrees incidence angle and 242 THz frequency, with the pump mask printing a pattern on the probe beam in the shape of the letter π. **(c)** Coherent control of absorption in time: the phase-conjugated pulse resulting from the time-reversal of a probe wave can interfere with the reflection from a second counter-propagating probe under an effective modulation by the probe.

active in the years to come. Nanoantennas and other resonant architectures, particularly with GaP's high potential for Nonlinear Optics, are a prominent topic of interest to the Nanophotonics and optical metamaterials community. The ability to reconfigure an antenna for harmonic generation or photo-catalysis, enhance or suppress their signal, change their resonant frequency is already powerful, but one could additionally add spatial modulation by imprinting spatial patterns in time. Achieving reconfigurable beam steering of a signal is a current topic of interest [120–122], and ITO could very well provide a platform for this. As can be seen in Fig. 7.1(b), by making the probe beam very large in space, the 310 nm ITO's modulation can be imaged with a camera - here the letter π. This modulation could be shaped to take the form of a grating or a photonic crystal lattice, using a digital micro-mirror device or spatial light modulator, and thus create reconfigurable, transient metasurfaces, inducing diffraction both in space and time.

Finally, after considering the more practical and application-minded prospects of the field and the further research this thesis could be used as a base for, one can contemplate the realisation of more complex temporal modulations. Recently, a temporal Fabry-Pérot and time crystal were demonstrated at microwave frequencies [97, 123]. A demonstration of these effects at optical frequencies would be an important result for the time-varying community. Another interesting direction of investigation would lie in disordered temporal media, where the changes in permittivity exhibit some degree of correlated or uncorrelated disorder [124–126], which can lead to temporal analogues of Anderson localisation. In the spirit of wave control, one can also

design a temporal coherent perfect absorber in ITO, by leveraging the effective permittivity oscillations at 2ω induced by a pump pulse on travelling waves in the medium. By timing the probe waves to arrive on the rise of the modulation, they are reflected in time, thus creating an interference between one wave and the other's conjugate and enabling dynamic control of a signal's amplitude. Such a control is shown here in Fig. 7.1(c), by performing the experiment in the 310 nm ITO at normal incidence for the pump, at 32 GW/cm^2. By varying the phase between the probe and the pump, the phase conjugated signal (PC) can be either suppressed or enhanced.

Using an interface such as the bilayer coupled with a tailored pump signal, complex temporal modulations could be achieved, the challenge now being in tailoring said pump signal and ensuring the rise and decay time of the modulation in the sample do not smear out the temporal evolution of the pump pulse. By gaining full control of the modulation in time, and using the advanced level of spatial control Nanophotonics are now capable of, the path towards a 4D optical wave synthesizer promises to bring its share of challenges and successes.

Appendix A

Characterisation of four wave mixing in an Indium Tin Oxide bilayer

An implication of the use of FWM as a platform for time-varying experiments is the change in the signal's dependence on illumination conditions, that are incidence angle of pump and probe, pulse frequency and pump and probe intensities. Optimal parameters could differ from the probe modulation measurement in the bilayer. This appendix focuses on the characterisation of FWM in the 40 nm ITO/Au bilayer in reflection, as described in section 4.4.

Particularly, the pump signal coupling to the medium is now important in the generation of the time-varying signal, as well as the spectral shape of the $\chi^{(3)}$ of ITO. Miller's rule informs us that third order effects are stronger for lower frequencies in ITO [127]. As can be seen in Fig. A.1(a), measuring the FWM signal for various carrier frequencies at an incidence angle of 65 degrees and for two pump intensities shows lower frequencies exhibiting a higher conversion efficiency than higher ones. The FWM signal is here taken at its maximum with regards to pump-probe delay. This result is likely due to a combination of the spectral shape of the $\chi^{(3)}$ of ITO along with the crossing of the Berreman resonance during modulation for frequencies 230 THz.

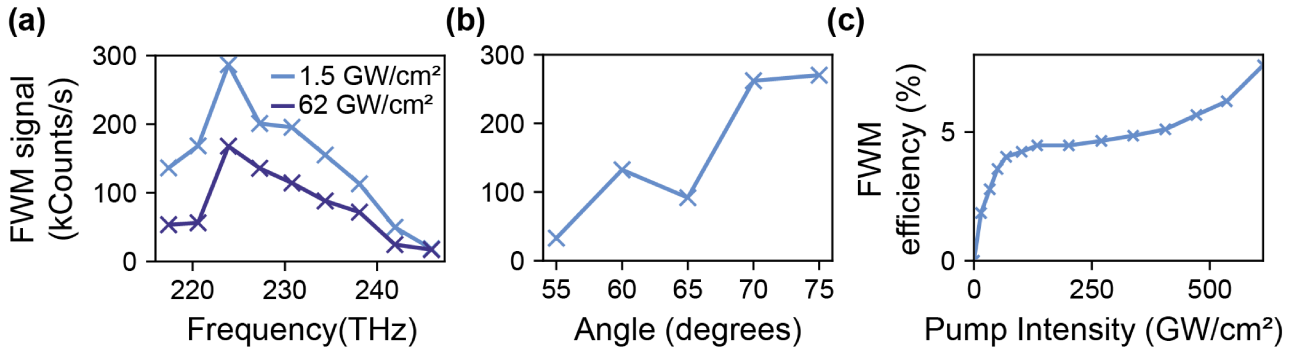

Figure A.1: Bilayer FWM characterisation. **(a)** Carrier frequency dependence of FWM for an incident angle of 65 degrees and a pump power of 70 GW/cm^2. Data was taken for two probe intensities of 1.5 GW/cm^2 (light blue curve) and 62 GW/cm^2 (dark blue curve), corresponding to the regimes of unperturbed and self-modulated probe. **(b)** Angular dependence of FWM for a pulse at 230 THz and low pump and probe intensities (9.3 and 1.2 GW/cm^2 respectively). **(c)** Efficiency of the FWM process, here defined as the ratio of FWM to probe power, as a function of pump intensity. The probe intensity is kept at 1.4 GW/cm^2, and the carrier frequency and angle to 230 THz and 65 degrees respectively. Panel (c) reproduced from [79].

The coupling of the pump beam now gaining importance over that of the probe, the incidence

angle of 65 degrees is not the ideal configuration for FWM anymore, as can be seen in Fig. A.1(b). Higher angles show better coupling from the pump (10 degrees below the probe) to the medium. Hence, the ideal FWM experiment, which would yield the strongest time-varying features, is more likely at lower frequency and higher incidence angle than the configuration chosen in the previous section.

Finally, we look into the intensity dependence of the FWM signal, and more particularly at its efficiency, here defined as the ratio of FWM to illuminating probe power. As can be seen in Fig. A.1(c), the efficiency dependence on pump intensity is very similar to that of the reflectivity modulation, with what seems like a linear increase at low intensities followed by a saturation at 100 GW/cm^2, reaching 7.5% at 612 GW/cm^2. This is quite interesting as the power dependence of FWM efficiency as defined above is expected to be quadratic with pump intensity below saturation (as 2 pump photons are involved in the process). This is likely due to the high pump intensities used even below saturation, with the quadratic shape of the curve being hidden for very low pump intensities in Fig. A.1(c).

Appendix B

Second harmonic generation at the Indium Tin Oxide interface

Let us start again from the vectorial expression of polarisation in the context of Nonlinear Optics:

$$P = \epsilon_0 \left(\tilde{\chi}^{(1)}\mathbf{E} + \tilde{\chi}^{(2)}\mathbf{E}^2 + \tilde{\chi}^{(3)}\mathbf{E}^3 + ... \right) \tag{2.8}$$

Considering second and third order terms for an electric field $E \propto e^{-i\omega t}$, frequencies 2ω and 3ω immediately appear, respectively corresponding to second and third harmonic. This can be translated in a Quantum Optics picture to multiple photons summing up to generate a photon with the sum of the energies (Fig. B.1(a,b)).

In equation 2.8, looking only at the second order term the following property comes naturally:

$$\begin{aligned} \mathbf{P}(\mathbf{E}) &= \tilde{\chi}^{(2)}\mathbf{E}^2 \\ \Rightarrow \mathbf{P}(-\mathbf{E}) &= \mathbf{P}(\mathbf{E}) \end{aligned} \tag{B.1}$$

Yet, for an amorphous and thus centrosymmetric material, the crystal symmetry requires

$$\mathbf{P}(-\mathbf{E}) = -\mathbf{P}(\mathbf{E}) \tag{B.2}$$

Clearly, equations B.1 and B.2 are not compatible, as a consequence centrosymmetric materials such as ITO cannot generate second or any even-order harmonic. The symmetry preventing generation of harmonics is only broken at the interface between media, allowing for SHG from an interfacial region near the surface of ITO [28, 101], as shown in Fig. B.1(c). THG, on the other hand, can originate from the bulk of the medium, as depicted in Fig. B.1(d).

The other interface and further reflections generate a lower signal due to absorption of the fundamental frequency in the NIR. The overall mechanism for this is presented in Fig. B.1(e). Absorption of the field at 230 THz in the ITO layer is strong, as the medium's ENZ frequency of 248 THz places the probe frequency in the metallic regime. On the other hand, the absorption

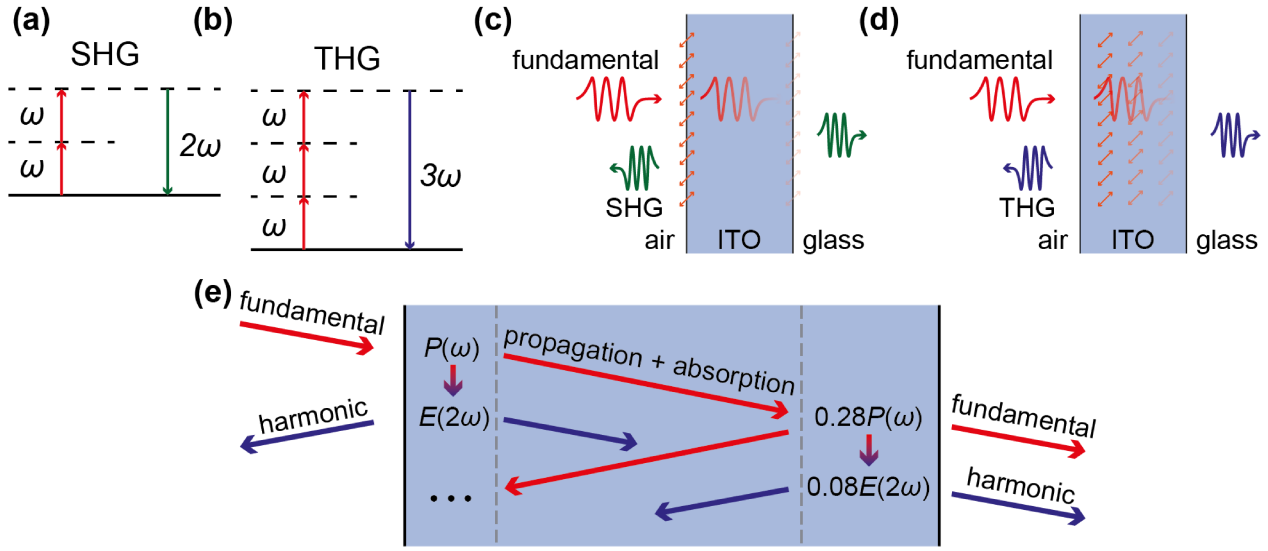

Figure B.1: Surface harmonic generation in ITO. **(a)** Second harmonic generation process: two photons at ω transition through virtual states to create a photon at 2ω. **(b)** Third harmonic generation process: in a similar manner three photons at ω add up to yield a photon at 3ω. **(c)** For a centrosymmetric material such as ITO second harmonic is generated at interfaces where the symmetry is broken. Absorption of the fundamental by the medium leads to imbalance between the fields at the two interfaces. **(d)** Third harmonic does not require symmetry breaking and thus can be generated over the whole volume of the medium. **(e)** Effect of absorption in the 310 nm ITO thin film on SHG. A probe pulse at frequency ω impinges on the medium from the air (left) and couples to the medium (blue area), inducing a polarisation amplitude $P(\omega)$ in the ITO at the interface. This interface generates a second harmonic field $E(2\omega)$. Meanwhile, the fundamental field propagates within the medium and reaches the other end of the ITO layer, creating a polarisation with amplitude $0.28P(\omega)$. The generated harmonic field will then have a corresponding amplitude $0.08E(2\omega)$, much below that generated at the first air/ITO interface. Subsequent round trips within the medium will generate a negligible amount of harmonic.

in the dielectric region is low (in the visible), and has little effect on harmonic propagation within the medium. After a single propagation of 310 nm at 230 THz (in the best case of an incident angle of 0 degrees), the probe field amplitude is down to 28%, leading to only 8% SHG at the second interface in comparison to the first one. This harmonic has to propagate again through the layer in order to be detected, without suffering loses. The probe, being reflected and travelling through the layer once again, only has an amplitude of 6% after a round trip, generating a negligible amount of harmonic signal. Thus we will consider the second harmonic as generated at the air/ITO interface on the first arrival of the probe, while keeping in mind the second interface generation as a perturbation and neglecting further round-trips within the layer. Note that the bilayer, by including an ITO/Au interface, presents too high complexity to study in this context for SHG [128].

Appendix C

Nonlinear Scattering Theory

Nonlinear generation of light can be described using nonlinear scattering theory, as presented in O'Brien et al.'s work [129]. This theory makes use of the reciprocal nature of Maxwell's equations, and is described in Fig. C.1(a). For a wave $\mathbf{E}_{in}(\omega)$ at fundamental frequency ω impinging on a nonlinear system, a field distribution $\mathbf{E}(\omega)$ will be created within the medium. This field generates a nonlinear polarisation. We will here consider the case of second harmonic generation and take $\mathbf{P}_{NL}(2\omega)$. This nonlinear polarisation will have a particular distribution in space depending on the fundamental illumination and coupling with the nonlinear medium, with various polarisations spread over a volume. Each point within that volume will then act as a current dipole, emitting light at the second harmonic frequency of 2ω. The generated field will then be out-coupled and collected as $\mathbf{E}_{NL}(2\omega)$ outside the medium. This is the general process for SHG in a nanophotonic nonlinear medium.

The reciprocity of Maxwell's equations becomes important in understanding and modelling which factors affect the efficiency of this harmonic generation. Just as each nonlinear dipole in the volume V generates a signal a field that contributes to $\mathbf{E}_{NL}(2\omega)$, reciprocity states the same nonlinear currents are created by an illuminating light of $\mathbf{E}_{NL}(2\omega)$. Hence, to model harmonic generation, one spans the parameter space of possible collected electric fields at the detector $\mathbf{E}_{det}(2\omega)$ and simulates the coupling of this field as a plane wave source to the medium. The overlap over the nonlinear volume of the detector-induced field $\mathbf{E}(2\omega)$ and the nonlinear polarisation generated by the fundamental field $\mathbf{P}_{NL}(2\omega)$ then gives the conversion efficiency from fundamental to harmonic. The nonlinear scattering theory is very useful on not only informing on harmonic generation efficiency, but also gives previous insights on how to engineer strong light generation and has been used many times in Nanophotonics where spatial field distributions can be complex but computed with finite difference time domain algorithms or TMM (see for example [69, 129]). The general expression for the nth harmonic generation is given by:

$$\mathbf{E}_{NL}(n\omega) \propto \omega^n \int_{\mathrm{V}} \mathbf{P}_{NL}(n\omega) \cdot \mathbf{E}(n\omega)\ \mathrm{dV} \tag{C.1}$$

A simple test on nonlinear scattering theory can be done by looking at SHG in a phase-matched crystal ,that is a medium for which the second order nonlinear susceptibility $\chi^{(2)}$ is

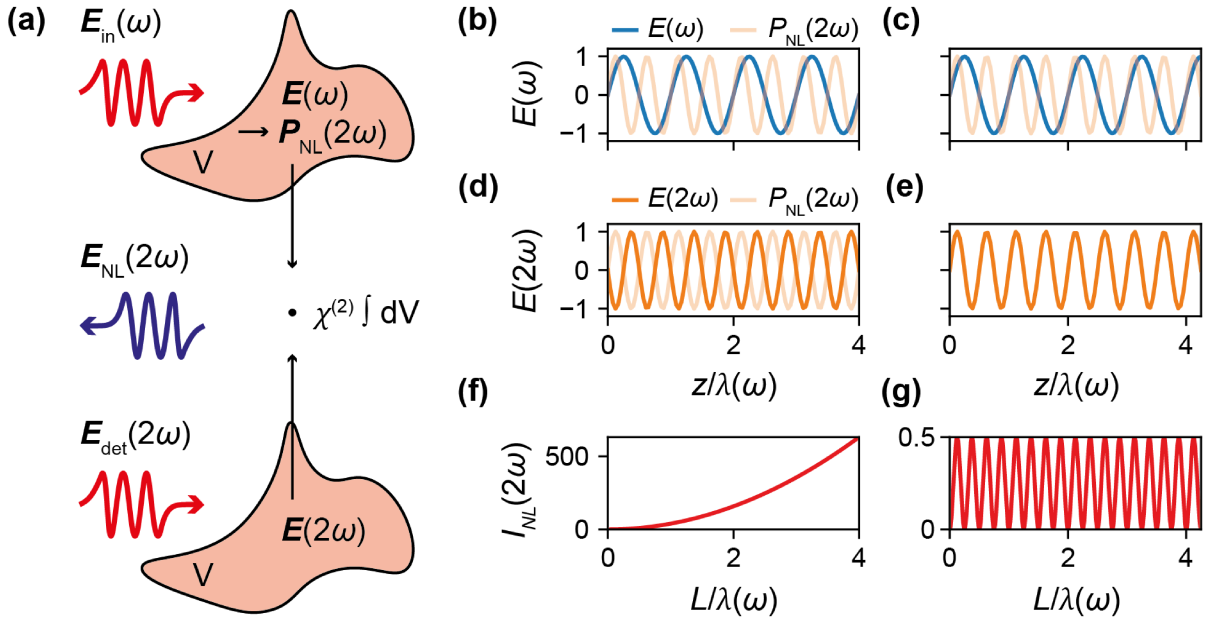

Figure C.1: Nonlinear scattering theory. **(a)** Diagram of nonlinear scattering theory: the field distribution and nonlinear polarisation is computed for the illuminating fundamental field (top). The linear field distribution at the harmonic wavelength is also computed (bottom) and the overlap between the two fields over the nonlinear medium gives the generated harmonic signal (middle). **(b,c)** Fundamental (blue curve) and nonlinear polarisation (yellow curve) fields in a single-layer phase-matched crystal. **(d,e)** Linear field at the harmonic generated by the detector plane wave (orange curve) in (d) transmission and (e) reflection, compared to the nonlinear polarisation (yellow curve). **(f,g)** Resulting SHG signal from nonlinear scattering theory as a function of crystal layer thickness. In (f) transmission the signal increases as L^2 just as in analytical theory [28] while in (g) reflection the fundamental and harmonic field interfere and prevent generation over an oscillation, which yields minor generation over distances where they cannot fully interfere.

non-zero and the wavevectors at the fundamental and harmonic are related by $2k(\omega) = k(2\omega)$. The medium is assumed to have no losses (k is real), but the theory is equally valid in the presence of an imaginary component of the refractive index or phase mismatch. The field distribution of the fundamental field, here taken to be polarised along x and propagating along z and expressed as $E(\omega) = e^{ik(\omega)z}$ is shown in blue in Fig. C.1 (b) and (c), for a crystal of length (b) $4\lambda(\omega)$ and (c) $4.25\lambda(\omega)$. The second order nonlinear polarisation is then taken to be $P_{NL}(2\omega) = E(\omega)^2$. The linear fields induced by a detector plane wave are shown in Fig. C.1(d,e) for (d) transmission and (e) reflection. For transmission, the detector is placed on the other end of the crystal, and thus the linear harmonic wave propagates as $E(2\omega) = e^{-ik(2\omega)z}$, while in reflection the detector wave travels with the fundamental wave as $E(2\omega) = e^{ik(2\omega)z}$. This is extremely important for the overlap integral: in the case of transmission, the polarisation and linear fields product gives $e^{i(2k(\omega)-k(2\omega))z} = 1$ while in reflection the dot product is $e^{i(2k(\omega)+k(2\omega))z} = e^{i2k(2\omega)z}$. Integrating over the volume, transmission will give a harmonic signal proportional to L^2 where L is the length of the crystal, as shows Fig. C.1(f), just as

expected from classical Nonlinear Optics [28]. For reflection, the dot product is a sinusoidal function and integrates to zero over a period. Therefore, the generated harmonic intensity will be extremely weak and will oscillate with the crystal length as shown in Fig. C.1(g), with the signal coming from sub-cycle interference (for example the added length of $0.25\lambda(\omega)$ in panels (c) and (e)). Note that any propagation and phase accumulation outside the nonlinear medium will only lead to a constant phase shift $\delta\phi$, which will have no effect in the dot product and integration.

What insights can we gain from nonlinear scattering theory? First, it separates the various elements and contributions to the harmonic signal. These can be divided as follow: the linear behaviour of the fundamental (coupling to the medium and field propagation and distribution), the linear behaviour of the harmonic (same), and nonlinear susceptibility. Time-varying effects will act on each of these elements, making the single and double slit experiment much more complex to understand. If SHG or THG were generated from the probe, how would the modulation affect the harmonic signal? To understand this, it is important to look at the effect of each of the contributions highlighted in nonlinear scattering theory. Can Fourier theory be directly applied to the harmonic signal, or would the effects be squared or cubed due to a prior modulation of the fundamental? Is the nonlinear susceptibility constant throughout the process, and if not what are its effects on the harmonic generation? These are difficult matters to model, even with a combination of nonlinear scattering theory, TMM and Fourier transform modelling. Nevertheless, the insights gained on the various mechanisms at play helps in understanding experimental results.

Another application of nonlinear scattering theory lies in the measurement of the nonlinear susceptibility of materials. Equation C.1 is a reduced version valid for any order of harmonics, but a specific value can be obtained by using the full expression for a given order. For THG, in a 1 dimensional lossless medium of length L, the harmonic field generated in transmission takes the following form [129]:

$$E_{THG}(3\omega) = \frac{9\omega^2}{2k(3\omega)c^2}\frac{e^{i\Delta kL}-1}{\Delta k}\chi^{(3)}(3\omega,\omega,\omega,\omega)E_0(\omega)^3 \tag{C.2}$$

where E_{THG} is the generated field, E_0 the fundamental field amplitude in the medium, $k(3\omega)$ the momentum of the harmonic light in the medium, c the speed of light, $\chi^{(3)}(3\omega,\omega,\omega,\omega)$ the third order nonlinear susceptibility and $\Delta k = k(3\omega) - 3k(\omega)$ the wavevector mismatch. To account for the presence of boundaries and losses in the medium, TMM is required to compute the coupling in the medium as well as the spatial distribution of the field. This induces a

correction factor $\kappa(\omega)$, which leads us to the formula

$$\chi^{(3)}(3\omega,\omega,\omega,\omega) = \left(\kappa(\omega)\frac{9\omega^2}{2k(3\omega)c^2}\frac{e^{i\Delta kL}-1}{\Delta k}\right)^{-1}\frac{I_{THG}(3\omega)}{I_0(\omega)^3} \tag{C.3}$$

Then, by measuring the input fundamental and output THG intensities, and using TMM, one can extract the nonlinear susceptibility from a thin film.

Appendix D

Two-photon absorption coefficient extraction

In Nonlinear Optics, the optical Kerr effect can be expressed as [28]:

$$\tilde{n}(I) = \tilde{n}_0 + \tilde{n}_2 \times I \tag{D.1}$$

where $\tilde{n}(I)$ is the intensity dependent refractive index of the nonlinear medium, $\tilde{n}_0$ the complex refractive index of the material in the absence of modulation, $\tilde{n}_2$ the complex nonlinear index corresponding to the Kerr effect and I the electric field intensity in the medium. Expressing this nonlinear coefficient in terms of its real and imaginary parts $\tilde{n}_2 = (n_2 + i\kappa_2)$, and assuming TPA is the driving mechanism behind the coefficient κ_2, one can then express the TPA coefficient β_{TPA} for a wave with free space momentum k_0 as [106]:

$$\beta_{\text{TPA}} = 2k_0\kappa_2 \tag{D.2}$$

Let us now consider the propagation of a wave at an angle of θ through a medium of thickness d with such Kerr nonlinearities, the accumulated phase φ is then given by:

$$\varphi(I) = \tilde{n}(I)k_0 d\cos(\theta) \tag{D.3}$$

$$\Leftrightarrow \varphi(I) = \tilde{n}_0 k_0 d\cos(\theta) + n_2 I k_0 d\cos(\theta) + i\kappa_2 I k_0 d\cos(\theta) \tag{D.4}$$

$$\Leftrightarrow \varphi(I) = \varphi_0 + \varphi_2(I) + i\varphi_{\text{TPA}}(I) \tag{D.5}$$

where φ_0 is the linear phase accumulation, $\varphi_2(I)$ is the phase accumulation due to Kerr effect, and $\varphi_{\text{TPA}}(I)$ is the change in loss in propagation due to TPA. We can then express φ_{TPA} as

$$\varphi_{\text{TPA}}(I) = \frac{\beta_{\text{TPA}}}{2} I d\cos(\theta) \tag{D.6}$$

We now need to relate the nonlinear phase accumulation to the measured reflected or transmitted signal from a slab of GaP. For this, we use the Airy formulas [130] (here in reflection) to get the complex Fresnel coefficient of the system (here in reflection r):

$$r = r_{ag} + \frac{t_{ag} t_{ga} r_{gs} e^{-2i\varphi(I)}}{1 - r_{ga} r_{gs} e^{-2i\varphi(I)}} \tag{D.7}$$

where r_{ij}, t_{ij} are the complex reflection and transmission coefficients of the various interfaces with ij denoting (a) air, (g) GaP and (s) the SiO_2 substrate. Note that it is assumed that the Fresnel coefficients of the interfaces do not change with intensity. This is a reasonable assumption in Nonlinear Optics considering $|\tilde{n}_0| \gg |\tilde{n}_2 I|$.

Grinblat et al. measured n_2 to be of the order of $\sim 10^{-5}$ to 10^{-4} cm^2/GW [106], hence for intensities $I \sim 100$ GW/cm^2 we can neglect $\varphi_2(I)$. The complex reflection coefficient can then be expressed as:

$$r = r_{ag} + \frac{t_{ag} t_{ga} r_{gs} e^{-2i\varphi_0} e^{-2\varphi_{\mathrm{TPA}}(I)}}{1 - r_{ga} r_{gs} e^{-2i\varphi_0} e^{-2\varphi_{\mathrm{TPA}}(I)}} \tag{D.8}$$

For $I \to 0$, $\varphi_{\mathrm{TPA}}(I) \to 0$ and r corresponds to the complex reflection coefficient of a linear Fabry-Perot. Meanwhile, for $I \to \infty$, $\varphi_{\mathrm{TPA}}(I) \to \infty$ and the numerator goes to zero while the denominator converges towards a value of 1, and thus $r \to r_{ag}$ meaning the reflectivity can only be decreased as far as the base level of the air/GaP interface reflection coefficient ($r_{ag} = 0.39$ at 230 THz and 45 degrees incident angle).

By fitting the Airy formula to the experimental data $R/R_0 = |r|^2/|r_0|^2$, we can extract the TPA coefficient β_{TPA}. Note that the field intensity inside the medium is computed from the incident field intensity using TMM. In the particular case of a GaP slab off-resonance, the electric field amplitude within and outside the layer are comparable $|E_{GaP}|^2 \simeq |E_{air}|^2$, so the correction factor comes back to the refractive index contrast n_{air}/n_{GaP}.

References

[1] E. Galiffi, "New degrees of freedom for metamaterials and metasurfaces: from hidden spatial dimensions to dynamical structures", PhD thesis (Imperial College London, 2020).

[2] J. B. Khurgin, "Optical Isolation by Temporal Modulation: Size, Frequency, and Power Constraints", ACS Photonics **10**, 1037–1045 (2023).

[3] V. Bacot, G. Durey, A. Eddi, M. Fink, and E. Fort, "Phase-conjugate mirror for water waves driven by the Faraday instability", Proceedings of the National Academy of Sciences **116**, 8809–8814 (2019).

[4] R. Fleury, D. L. Sounas, C. F. Sieck, M. R. Haberman, and A. Alù, "Sound Isolation and Giant Linear Nonreciprocity in a Compact Acoustic Circulator", Science **343**, 516–519 (2014).

[5] C. Cho, X. Wen, N. Park, and J. Li, "Digitally virtualized atoms for acoustic metamaterials", Nature Communications **11**, 251 (2020).

[6] E. A. Kittlaus, N. T. Otterstrom, P. Kharel, S. Gertler, and P. T. Rakich, "Non-reciprocal interband Brillouin modulation", Nature Photonics **12**, 613–619 (2018).

[7] Z. Shen, Y.-L. Zhang, Y. Chen, C.-L. Zou, Y.-F. Xiao, X.-B. Zou, F.-W. Sun, G.-C. Guo, and C.-H. Dong, "Experimental realization of optomechanically induced non-reciprocity", Nature Photonics **10**, 657–661 (2016).

[8] J. del Pino, J. J. Slim, and E. Verhagen, "Non-Hermitian chiral phononics through optomechanically induced squeezing", Nature **606**, 82–87 (2022).

[9] A. Nagulu, N. Reiskarimian, and H. Krishnaswamy, "Non-reciprocal electronics based on temporal modulation", Nature Electronics **3**, 241–250 (2020).

[10] S. F. Preble, Q. Xu, and M. Lipson, "Changing the colour of light in a silicon resonator", Nature Photonics **1**, 293–296 (2007).

[11] Z. Yu and S. Fan, "Complete optical isolation created by indirect interband photonic transitions", Nature Photonics **3**, 91–94 (2009).

[12] K. Schultheiss, N. Sato, P. Matthies, L. Körber, K. Wagner, T. Hula, O. Gladii, J. Pearson, A. Hoffmann, M. Helm, J. Fassbender, and H. Schultheiss, "Time Refraction of Spin Waves", Physical Review Letters **126**, 137201 (2021).

[13] V. Pacheco-Peña, D. M. Solís, and N. Engheta, "Time-varying electromagnetic media: opinion", Optical Materials Express **12**, 3829–3836 (2022).

[14] E. Galiffi, R. Tirole, S. Yin, H. Li, S. Vezzoli, P. A. Huidobro, M. G. Silveirinha, R. Sapienza, A. Alù, and J. B. Pendry, "Photonics of time-varying media", Advanced Photonics **4**, 014002 (2022).

[15] J. T. Mendonca, *Theory of Photon Acceleration* (CRC Press, 2000).

[16] V. I. Semenova, "Reflection of electromagnetic waves from an ionization front", Radiophysics and Quantum Electronics **10**, 599–604 (1967).

[17] M. Lampe, E. Ott, and J. H. Walker, "Interaction of electromagnetic waves with a moving ionization front", The Physics of Fluids **21**, 42–54 (1978).

[18] E. Yablonovitch, "Self-phase modulation and short-pulse generation from laser-breakdown plasmas", Physical Review A **10**, 1888–1895 (1974).

[19] V. L. Granatstein, P. Sprangle, R. K. Parker, J. Pasour, M. Herndon, S. P. Schlesinger, and J. L. Seftor, "Realization of a relativistic mirror: Electromagnetic backscattering from the front of a magnetized relativistic electron beam", Physical Review A **14**, 1194–1201 (1976).

[20] S. C. Wilks, J. M. Dawson, W. B. Mori, T. Katsouleas, and M. E. Jones, "Photon accelerator", Physical Review Letters **62**, 2600–2603 (1989).

[21] P. A. Franken, A. E. Hill, C. W. Peters, and G. Weinreich, "Generation of Optical Harmonics", Physical Review Letters **7**, 118–119 (1961).

[22] F. Shimizu, "Frequency Broadening in Liquids by a Short Light Pulse", Physical Review Letters **19**, 1097–1100 (1967).

[23] R. R. Alfano and S. L. Shapiro, "Observation of Self-Phase Modulation and Small-Scale Filaments in Crystals and Glasses", Physical Review Letters **24**, 592–594 (1970).

[24] R. H. Stolen and C. Lin, "Self-phase-modulation in silica optical fibers", Physical Review A **17**, 1448–1453 (1978).

[25] J. T. Manassah, M. A. Mustafa, R. R. Alfano, and P. P. Po, "Induced supercontinuum and steepening of an ultrafast laser pulse", Physics Letters A **113**, 242–247 (1985).

[26] R. R. Alfano, Q. X. Li, T. Jimbo, J. T. Manassah, and P. P. Ho, "Induced spectral broadening of a weak picosecond pulse in glass produced by an intense picosecond pulse", Optics Letters **11**, 626–628 (1986).

[27] M. N. Islam, L. F. Mollenauer, R. H. Stolen, J. R. Simpson, and H. T. Shang, "Cross-phase modulation in optical fibers", Optics Letters **12**, 625–627 (1987).

[28] R. W. Boyd, *Nonlinear Optics* (Academic Press, 2020).

[29] A. Zeilinger, R. Gähler, C. G. Shull, W. Treimer, and W. Mampe, "Single- and double-slit diffraction of neutrons", Reviews of Modern Physics **60**, 1067–1073 (1988).

[30] J. Felber, G. Müller, R. Gähler, and R. Golub, "Time dependent neutron optics: II. Diffraction in space and time", Physica B: Condensed Matter **162**, 191–196 (1990).

[31] A. Steane, P. Szriftgiser, P. Desbiolles, and J. Dalibard, "Phase Modulation of Atomic de Broglie Waves", Physical Review Letters **74**, 4972–4975 (1995).

[32] P. Szriftgiser, D. Guéry-Odelin, M. Arndt, and J. Dalibard, "Atomic Wave Diffraction and Interference Using Temporal Slits", Physical Review Letters **77**, 4–7 (1996).

[33] Brukner and A. Zeilinger, "Diffraction of matter waves in space and in time", Physical Review A **56**, 3804–3824 (1997).

[34] M. Moshinsky, "Diffraction in Time", Physical Review **88**, 625–631 (1952).

[35] E. Galiffi, "Broadband Nonreciprocal Amplification in Luminal Metamaterials", Physical Review Letters **123**, 206101 (2019).

[36] E. Galiffi, Y.-T. Wang, Z. Lim, J. Pendry, A. Alù, and P. A. Huidobro, "Wood Anomalies and Surface-Wave Excitation with a Time Grating", Physical Review Letters **125**, 127403 (2020).

[37] E. Galiffi, S. Yin, and A. Alú, "Tapered photonic switching", Nanophotonics **11**, 3575–3581 (2022).

[38] P. N. Butcher and D. Cotter, *The Elements of Nonlinear Optics* (Cambridge University Press, 1990).

[39] M. Conforti and G. Della Valle, "Derivation of third-order nonlinear susceptibility of thin metal films as a delayed optical response", Physical Review B **85**, 245423 (2012).

[40] H. Qian, Y. Xiao, and Z. Liu, "Giant Kerr response of ultrathin gold films from quantum size effect", Nature Communications **7**, 13153 (2016).

[41] S. Yu, X. Wu, Y. Wang, X. Guo, and L. Tong, "2D Materials for Optical Modulation: Challenges and Opportunities", Advanced Materials **29**, 1606128 (2017).

[42] J. W. You, S. R. Bongu, Q. Bao, and N. C. Panoiu, "Nonlinear optical properties and applications of 2D materials: theoretical and experimental aspects", Nanophotonics **8**, 63–97 (2019).

[43] J. Kuttruff, D. Garoli, J. Allerbeck, R. Krahne, A. De Luca, D. Brida, V. Caligiuri, and N. Maccaferri, "Ultrafast all-optical switching enabled by epsilon-near-zero-tailored absorption in metal-insulator nanocavities", Communications Physics **3**, 1–7 (2020).

[44] A. R. Rashed, B. C. Yildiz, S. R. Ayyagari, and H. Caglayan, "Hot electron dynamics in ultrafast multilayer epsilon-near-zero metamaterials", Physical Review B **101**, 165301 (2020).

[45] M. Decker and I. Staude, "Resonant dielectric nanostructures: a low-loss platform for functional nanophotonics", Journal of Optics **18**, 103001 (2016).

[46] A. I. Kuznetsov, A. E. Miroshnichenko, M. L. Brongersma, Y. S. Kivshar, and B. Luk'yanchuk, "Optically resonant dielectric nanostructures", Science **354**, 2472 (2016).

[47] D. G. Baranov, D. A. Zuev, S. I. Lepeshov, O. V. Kotov, A. E. Krasnok, A. B. Evlyukhin, and B. N. Chichkov, "All-dielectric nanophotonics: the quest for better materials and fabrication techniques", Optica **4**, 814–825 (2017).

[48] N. Kinsey, C. DeVault, A. Boltasseva, and V. M. Shalaev, "Near-zero-index materials for photonics", Nature Reviews Materials **4**, 742–760 (2019).

[49] A. Ciattoni, A. Marini, C. Rizza, M. Scalora, and F. Biancalana, "Polariton excitation in epsilon-near-zero slabs: Transient trapping of slow light", Physical Review A **87**, 053853 (2013).

[50] F. J. Rodríguez-Fortuño, A. Vakil, and N. Engheta, "Electric Levitation Using $$-Near-Zero Metamaterials", Physical Review Letters **112**, 033902 (2014).

[51] P. Drude, "Zur Elektronentheorie der Metalle", Annalen der Physik **306**, 566–613 (1900).

[52] J. Bohn, T. S. Luk, C. Tollerton, S. W. Hutchings, I. Brener, S. Horsley, W. L. Barnes, and E. Hendry, "All-optical switching of an epsilon-near-zero plasmon resonance in indium tin oxide", Nature Communications **12**, 1017 (2021).

[53] M. Z. Alam, I. De Leon, and R. W. Boyd, "Large optical nonlinearity of indium tin oxide in its epsilon-near-zero region", Science **352**, 795–797 (2016).

[54] L. Rodríguez-Suné, M. Scalora, A. S. Johnson, C. Cojocaru, N. Akozbek, Z. J. Coppens, D. Perez-Salinas, S. Wall, and J. Trull, "Study of second and third harmonic generation from an indium tin oxide nanolayer: Influence of nonlocal effects and hot electrons", APL Photonics **5**, 010801 (2020).

[55] S. Vassant, J.-P. Hugonin, F. Marquier, and J.-J. Greffet, "Berreman mode and epsilon near zero mode", Optics Express **20**, 23971–23977 (2012).

[56] S. A. Maier, *Plasmonics: Fundamentals and Applications* (Springer Science & Business Media, 2007).

[57] J. B. Khurgin, M. Clerici, and N. Kinsey, "Fast and Slow Nonlinearities in Epsilon-Near-Zero Materials", Laser & Photonics Reviews **15**, 2000291 (2021).

[58] H. Wang, K. Du, C. Jiang, Z. Yang, L. Ren, W. Zhang, S. J. Chua, and T. Mei, "Extended Drude Model for Intraband-Transition-Induced Optical Nonlinearity", Physical Review Applied **11**, 064062 (2019).

[59] M. Rudan, *Physics of Semiconductor Devices* (Springer, 2014).

[60] L. Caspani, R. Kaipurath, M. Clerici, M. Ferrera, T. Roger, J. Kim, N. Kinsey, M. Pietrzyk, A. Di Falco, V. Shalaev, A. Boltasseva, and D. Faccio, "Enhanced Nonlinear Refractive Index in Epsilon-Near-Zero Materials", Physical Review Letters **116**, 233901 (2016).

[61] E. G. Carnemolla, L. Caspani, C. DeVault, M. Clerici, S. Vezzoli, V. Bruno, V. M. Shalaev, D. Faccio, A. Boltasseva, and M. Ferrera, "Degenerate optical nonlinear enhancement in epsilon-near-zero transparent conducting oxides", Optical Materials Express **8**, 3392–3400 (2018).

[62] M. Ferrera and E. G. Carnemolla, "Ultra-fast transient plasmonics using transparent conductive oxides", Journal of Optics **20**, 024007 (2018).

[63] V. Bruno, S. Vezzoli, C. DeVault, E. Carnemolla, M. Ferrera, A. Boltasseva, V. M. Shalaev, D. Faccio, and M. Clerici, "Broad Frequency Shift of Parametric Processes in Epsilon-Near-Zero Time-Varying Media", Applied Sciences **10**, 1318 (2020).

[64] Y. Zhou, M. Z. Alam, M. Karimi, J. Upham, O. Reshef, C. Liu, A. E. Willner, and R. W. Boyd, "Broadband frequency translation through time refraction in an epsilon-near-zero material", Nature Communications **11**, 2180 (2020).

[65] E. G. Carnemolla, W. Jaffray, M. Clerici, L. Caspani, D. Faccio, F. Biancalana, C. Devault, V. M. Shalaev, A. Boltasseva, and M. Ferrera, "Visible photon generation via four-wave mixing in near-infrared near-zero-index thin films", Optics Letters **46**, 5433–5436 (2021).

[66] C. Liu, M. Z. Alam, K. Pang, K. Manukyan, J. R. Hendrickson, E. M. Smith, Y. Zhou, O. Reshef, H. Song, R. Zhang, H. Song, F. Alishahi, A. Fallahpour, A. Almaiman, R. W. Boyd, M. Tur, and A. E. Willner, "Tunable Doppler shift using a time-varying epsilon-near-zero thin film near 1550 nm", Optics Letters **46**, 3444–3447 (2021).

[67] J. Bohn, T. S. Luk, S. Horsley, and E. Hendry, "Spatiotemporal refraction of light in an epsilon-near-zero indium tin oxide layer: frequency shifting effects arising from interfaces", Optica **8**, 1532–1537 (2021).

[68] S. Vezzoli, V. Bruno, C. DeVault, T. Roger, V. M. Shalaev, A. Boltasseva, M. Ferrera, M. Clerici, A. Dubietis, and D. Faccio, "Optical Time Reversal from Time-Dependent Epsilon-Near-Zero Media", Physical Review Letters **120**, 043902 (2018).

[69] V. Bruno, C. DeVault, S. Vezzoli, Z. Kudyshev, T. Huq, S. Mignuzzi, A. Jacassi, S. Saha, Y. Shah, S. Maier, D. Cumming, A. Boltasseva, M. Ferrera, M. Clerici, D. Faccio, R. Sapienza, and V. Shalaev, "Negative Refraction in Time-Varying Strongly Coupled Plasmonic-Antenna–Epsilon-Near-Zero Systems", Physical Review Letters **124**, 043902 (2020).

[70] M. Taghinejad, H. Taghinejad, Z. Xu, Y. Liu, S. P. Rodrigues, K.-T. Lee, T. Lian, A. Adibi, and W. Cai, "Hot-Electron-Assisted Femtosecond All-Optical Modulation in Plasmonics", Advanced Materials **30**, 1704915 (2018).

[71] M. Taghinejad, H. Taghinejad, Z. Xu, K.-T. Lee, S. P. Rodrigues, J. Yan, A. Adibi, T. Lian, and W. Cai, "Ultrafast Control of Phase and Polarization of Light Expedited by Hot-Electron Transfer", Nano Letters **18**, 5544–5551 (2018).

[72] Y. Yang, J. Lu, A. Manjavacas, T. S. Luk, H. Liu, K. Kelley, J.-P. Maria, E. L. Runnerstrom, M. B. Sinclair, S. Ghimire, and I. Brener, "High-harmonic generation from an epsilon-near-zero material", Nature Physics **15**, 1022–1026 (2019).

[73] A. D. Dunkelberger, D. C. Ratchford, A. B. Grafton, V. M. Breslin, E. S. Ryland, D. S. Katzer, K. P. Fears, R. J. Weiblen, I. Vurgaftman, A. J. Giles, C. T. Ellis, J. G. Tischler, J. D. Caldwell, and J. C. Owrutsky, "Ultrafast Active Tuning of the Berreman Mode", ACS Photonics **7**, 279–287 (2020).

[74] S. Saha, B. T. Diroll, J. Shank, Z. Kudyshev, A. Dutta, S. N. Chowdhury, T. S. Luk, S. Campione, R. D. Schaller, V. M. Shalaev, A. Boltasseva, and M. G. Wood, "Broadband, High-Speed, and Large-Amplitude Dynamic Optical Switching with Yttrium-Doped Cadmium Oxide", Advanced Functional Materials **30**, 1908377 (2020).

[75] S. Saha, B. Diroll, M. G. Ozlu, S. N. Chowdhury, S. Peana, Z. Kudyshev, R. Schaller, Z. Jacob, V. M. Shalaev, A. V. Kildishev, and A. Boltasseva, "Engineering the Temporal Dynamics with Fast and Slow Materials for All-Optical Switching", arXiv, `10.48550/arXiv.2208.12927` (2022).

[76] M. Z. Alam, S. A. Schulz, J. Upham, I. De Leon, and R. W. Boyd, "Large optical nonlinearity of nanoantennas coupled to an epsilon-near-zero material", Nature Photonics **12**, 79–83 (2018).

[77] C. Liu, M. Z. Alam, K. Pang, K. Manukyan, O. Reshef, Y. Zhou, S. Choudhary, J. Patrow, A. Pennathurs, H. Song, Z. Zhao, R. Zhang, F. Alishahi, A. Fallahpour, Y. Cao, A. Almaiman, J. M. Dawlaty, M. Tur, R. W. Boyd, and A. E. Willner, "Photon Acceleration Using a Time-Varying Epsilon-near-Zero Metasurface", ACS Photonics **8**, 716–720 (2021).

[78] K. Pang, M. Z. Alam, Y. Zhou, C. Liu, O. Reshef, K. Manukyan, M. Voegtle, A. Pennathur, C. Tseng, X. Su, H. Song, Z. Zhao, R. Zhang, H. Song, N. Hu, A. Almaiman, J. M. Dawlaty, R. W. Boyd, M. Tur, and A. E. Willner, "Adiabatic Frequency Conversion Using a Time-Varying Epsilon-Near-Zero Metasurface", Nano Letters **21**, 5907–5913 (2021).

[79] R. Tirole, E. Galiffi, J. Dranczewski, T. Attavar, B. Tilmann, Y.-T. Wang, P. A. Huidobro, A. Alú, J. B. Pendry, S. A. Maier, S. Vezzoli, and R. Sapienza, "Saturable Time-Varying Mirror Based on an Epsilon-Near-Zero Material", Physical Review Applied **18**, 054067 (2022).

[80] I. W. Un, S. Sarkar, and Y. Sivan, "Electronic-Based Model of the Optical Nonlinearity of Low-Electron-Density Drude Materials", Physical Review Applied **19**, 044043 (2023).

[81] R. Tirole, S. Vezzoli, E. Galiffi, I. Robertson, D. Maurice, B. Tilmann, S. A. Maier, J. B. Pendry, and R. Sapienza, "Double-slit time diffraction at optical frequencies", Nature Physics, 1–4 (2023).

[82] D. M. Solís, R. Kastner, and N. Engheta, "Time-varying materials in the presence of dispersion: plane-wave propagation in a Lorentzian medium with temporal discontinuity", Photonics Research **9**, 1842–1853 (2021).

[83] J. Sloan, N. Rivera, J. D. Joannopoulos, and M. Soljačić, "Optical properties of dispersive time-dependent materials", arXiv, `10.48550/arXiv.2211.16166` (2022).

[84] R. Sapienza, "Photonic nano materials: anisotropic transport and optical Bloch oscillations", PhD thesis (Université Pierre et Marie Curie - Paris VI, 2005).

[85] J. A. Arnaud, W. M. Hubbard, G. D. Mandeville, B. d. l. Clavière, E. A. Franke, and J. M. Franke, "Technique for Fast Measurement of Gaussian Laser Beam Parameters", Applied Optics **10**, 2775–2776 (1971).

[86] D. R. Skinner and R. E. Whitcher, "Measurement of the radius of a high-power laser beam near the focus of a lens", Journal of Physics E: Scientific Instruments **5**, 237 (1972).

[87] N. Del Fatti, C. Voisin, M. Achermann, S. Tzortzakis, D. Christofilos, and F. Vallée, "Nonequilibrium electron dynamics in noble metals", Physical Review B **61**, 16956–16966 (2000).

[88] T. Young, *A Course of Lectures on Natural Philosophy and the Mechanical Arts* (Taylor and Walton, 1845).

[89] G. Taylor, "Interference Fringes with Feeble Light", Proceedings of the Cambridge Philosophical Society **15**, 114–115 (1909).

[90] C. Jönsson, "Elektroneninterferenzen an mehreren künstlich hergestellten Feinspalten", Zeitschrift für Physik **161**, 454–474 (1961).

[91] P. G. Merli, G. F. Missiroli, and G. Pozzi, "On the statistical aspect of electron interference phenomena", American Journal of Physics **44**, 306–307 (1976).

[92] A. D. Cronin, J. Schmiedmayer, and D. E. Pritchard, "Optics and interferometry with atoms and molecules", Reviews of Modern Physics **81**, 1051–1129 (2009).

[93] K. Hornberger, S. Gerlich, P. Haslinger, S. Nimmrichter, and M. Arndt, "Colloquium: Quantum interference of clusters and molecules", Reviews of Modern Physics **84**, 157–173 (2012).

[94] J. Felber, R. Gähler, C. Rausch, and R. Golub, "Matter waves at a vibrating surface: Transition from quantum-mechanical to classical behavior", Physical Review A **53**, 319–328 (1996).

[95] G. V. Hartland, "Optical Studies of Dynamics in Noble Metal Nanostructures", Chemical Reviews **111**, 3858–3887 (2011).

[96] N. Kinsey and J. Khurgin, "Nonlinear epsilon-near-zero materials explained: opinion", Optical Materials Express **9**, 2793–2796 (2019).

[97] H. Moussa, G. Xu, S. Yin, E. Galiffi, Y. Ra'di, and A. Alù, "Observation of temporal reflection and broadband frequency translation at photonic time interfaces", Nature Physics, 1–6 (2023).

[98] J. Zhang, P. W. Hess, A. Kyprianidis, P. Becker, A. Lee, J. Smith, G. Pagano, I.-D. Potirniche, A. C. Potter, A. Vishwanath, N. Y. Yao, and C. Monroe, "Observation of a discrete time crystal", Nature **543**, 217–220 (2017).

[99] T. S. Luk, D. de Ceglia, S. Liu, G. A. Keeler, R. P. Prasankumar, M. A. Vincenti, M. Scalora, M. B. Sinclair, and S. Campione, "Enhanced third harmonic generation from the epsilon-near-zero modes of ultrathin films", Applied Physics Letters **106**, 151103 (2015).

[100] A. Capretti, Y. Wang, N. Engheta, and L. Dal Negro, "Comparative Study of Second-Harmonic Generation from Epsilon-Near-Zero Indium Tin Oxide and Titanium Nitride Nanolayers Excited in the Near-Infrared Spectral Range", ACS Photonics **2**, 1584–1591 (2015).

[101] Y. R. Shen, "Optical Second Harmonic Generation at Interfaces", Annual Review of Physical Chemistry **40**, 327–350 (1989).

[102] M. A. Vincenti, M. Kamandi, D. de Ceglia, C. Guclu, M. Scalora, and F. Capolino, "Second-harmonic generation in longitudinal epsilon-near-zero materials", Physical Review B **96**, 045438 (2017).

[103] A. Krasnok, M. Tymchenko, and A. Alù, "Nonlinear metasurfaces: a paradigm shift in nonlinear optics", Materials Today **21**, 8–21 (2018).

[104] T. Santiago-Cruz, V. Sultanov, H. Zhang, L. A. Krivitsky, and M. V. Chekhova, "Entangled photons from subwavelength nonlinear films", Optics Letters **46**, 653–656 (2021).

[105] V. Sultanov, T. Santiago-Cruz, and M. V. Chekhova, "Flat-optics generation of broadband photon pairs with tunable polarization entanglement", Optics Letters **47**, 3872–3875 (2022).

[106] G. Grinblat, M. P. Nielsen, P. Dichtl, Y. Li, R. F. Oulton, and S. A. Maier, "Ultrafast sub–30-fs all-optical switching based on gallium phosphide", Science Advances **5**, 3262 (2019).

[107] G. Grinblat, H. Zhang, M. P. Nielsen, L. Krivitsky, R. Berté, Y. Li, B. Tilmann, E. Cortés, R. F. Oulton, A. I. Kuznetsov, and S. A. Maier, "Efficient ultrafast all-optical modulation in a nonlinear crystalline gallium phosphide nanodisk at the anapole excitation", Science Advances **6**, 3123 (2020).

[108] M. R. Shcherbakov, P. P. Vabishchevich, A. S. Shorokhov, K. E. Chong, D.-Y. Choi, I. Staude, A. E. Miroshnichenko, D. N. Neshev, A. A. Fedyanin, and Y. S. Kivshar, "Ultrafast All-Optical Switching with Magnetic Resonances in Nonlinear Dielectric Nanostructures", Nano Letters **15**, 6985–6990 (2015).

[109] M. R. Shcherbakov, S. Liu, V. V. Zubyuk, A. Vaskin, P. P. Vabishchevich, G. Keeler, T. Pertsch, T. V. Dolgova, I. Staude, I. Brener, and A. A. Fedyanin, "Ultrafast all-optical tuning of direct-gap semiconductor metasurfaces", Nature Communications **8**, 17 (2017).

[110] G. Della Valle, B. Hopkins, L. Ganzer, T. Stoll, M. Rahmani, S. Longhi, Y. S. Kivshar, C. De Angelis, D. N. Neshev, and G. Cerullo, "Nonlinear Anisotropic Dielectric Metasurfaces for Ultrafast Nanophotonics", ACS Photonics **4**, 2129–2136 (2017).

[111] N. Karl, P. P. Vabishchevich, M. R. Shcherbakov, S. Liu, M. B. Sinclair, G. Shvets, and I. Brener, "Frequency Conversion in a Time-Variant Dielectric Metasurface", Nano Letters **20**, 7052–7058 (2020).

[112] A. Tittl, A. John-Herpin, A. Leitis, E. R. Arvelo, and H. Altug, "Metasurface-Based Molecular Biosensing Aided by Artificial Intelligence", Angewandte Chemie International Edition **58**, 14810–14822 (2019).

[113] M. L. Tseng, Y. Jahani, A. Leitis, and H. Altug, "Dielectric Metasurfaces Enabling Advanced Optical Biosensors", ACS Photonics **8**, 47–60 (2021).

[114] B. Tilmann, T. Huq, T. Possmayer, J. Dranczewski, B. Nickel, H. Zhang, L. Krivitsky, A. I. Kuznetsov, L. de S. Menezes, S. Vezzoli, R. Sapienza, and S. A. Maier, "Comparison of Harmonic Generation from Crystalline and Amorphous Gallium Phosphide Nanofilms", Advanced Optical Materials, 2300269 (2023).

[115] M. R. Shcherbakov, K. Werner, Z. Fan, N. Talisa, E. Chowdhury, and G. Shvets, "Photon acceleration and tunable broadband harmonics generation in nonlinear time-dependent metasurfaces", Nature Communications **10**, 1345 (2019).

[116] S. Suresh, O. Reshef, M. Z. Alam, J. Upham, M. Karimi, and R. W. Boyd, "Enhanced Nonlinear Optical Responses of Layered Epsilon-near-Zero Metamaterials at Visible Frequencies", ACS Photonics **8**, 125–129 (2021).

[117] N. Maccaferri, A. Zilli, T. Isoniemi, L. Ghirardini, M. Iarossi, M. Finazzi, M. Celebrano, and F. De Angelis, "Enhanced Nonlinear Emission from Single Multilayered Metal–Dielectric Nanocavities Resonating in the Near-Infrared", ACS Photonics **8**, 512–520 (2021).

[118] A. Patri, K. G. Cognée, D. M. Myers, L. Haeberlé, V. Menon, and S. Kéna-Cohen, "Hybrid epsilon-near-zero modes of photonic gap antennas", Physical Review B **105**, 165126 (2022).

[119] F. Thouin, D. M. Myers, A. Patri, B. Baloukas, L. Martinu, and S. Kéna-Cohen, "Broadband field-enhancement in epsilon-near-zero photonic gap antennas", arXiv, `10.48550/arXiv.2211.05214` (2022).

[120] Y.-W. Huang, H. W. H. Lee, R. Sokhoyan, R. A. Pala, K. Thyagarajan, S. Han, D. P. Tsai, and H. A. Atwater, "Gate-Tunable Conducting Oxide Metasurfaces", Nano Letters **16**, 5319–5325 (2016).

[121] V. Pacheco-Peña and N. Engheta, "Temporal metamaterials with gain and loss", arXiv, `10.48550/arXiv.2108.01007` (2021).

[122] M. Karimi, M. Z. Alam, J. Upham, O. Reshef, and R. W. Boyd, "Time-varying gradient metasurface with applications in all-optical beam steering", Nanophotonics **12**, 1733–1740 (2023).

[123] X. Wang, M. S. Mirmoosa, V. S. Asadchy, C. Rockstuhl, S. Fan, and S. A. Tretyakov, "Metasurface-Based Realization of Photonic Time Crystals", arXiv, `10.48550/arXiv.2208.07231` (2022).

[124] Y. Sharabi, E. Lustig, and M. Segev, "Disordered Photonic Time Crystals", Physical Review Letters **126**, 163902 (2021).

[125] R. Carminati, H. Chen, R. Pierrat, and B. Shapiro, "Universal Statistics of Waves in a Random Time-Varying Medium", Physical Review Letters **127**, 094101 (2021).

[126] J. Kim, D. Lee, S. Yu, and N. Park, "Unidirectional scattering with spatial homogeneity using correlated photonic time disorder", Nature Physics, 1–7 (2023).

[127] R. C. Miller, "Optical second harmonic generation in piezoelectric crystals", Applied Physics Letters **5**, 17–19 (1964).

[128] M. Scalora, M. A. Vincenti, D. de Ceglia, N. Akozbek, M. J. Bloemer, C. De Angelis, J. W. Haus, R. Vilaseca, J. Trull, and C. Cojocaru, "Harmonic generation from metal-oxide and metal-metal boundaries", Physical Review A **98**, 023837 (2018).

[129] K. O'Brien, H. Suchowski, J. Rho, A. Salandrino, B. Kante, X. Yin, and X. Zhang, "Predicting nonlinear properties of metamaterials from the linear response", Nature Materials **14**, 379–383 (2015).

[130] B. E. A. Saleh and M. C. Teich, *Fundamentals of Photonics* (John Wiley & Sons, 2019).